

FILE COPY
DRAFTING ENGINEERING

ADA 054909

FOR FURTHER TRAN

USCIPI Report 810



12

UNIVERSITY OF SOUTHERN CALIFORNIA

AN INVESTIGATION INTO AN A POSTERIORI
METHOD OF IMAGE RESTORATION

by

John Baird Morton

April 1978

Image Processing Institute
University of Southern California
Los Angeles, California 90007

Sponsored by

Advanced Research Projects Agency
Contract No. F-33615-76-C-1203
ARPA Order No. 3119

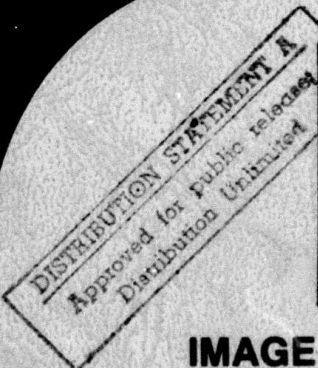
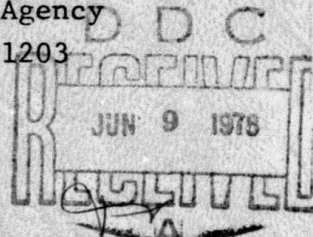


IMAGE PROCESSING INSTITUTE

78 06 08 038

14 USCIPI - 810

6
AN INVESTIGATION INTO AN A POSTERIORI
METHOD OF IMAGE RESTORATION

by

10 John Baird / Morton

11 Apr 1978

12 222p.

Image Processing Institute
University of Southern California
Los Angeles, California 90007

9 Technical Dept.

DDC

REPRODUCED

JUN 9 1978

REGULUS

A

This research was supported by the Advanced Research Projects Agency of the Department of Defense and was monitored by the Wright Patterson Air Force Base under Contract F33615-76-C-1203, ARPA Order 3119.

15 DISTRIBUTION STATEMENT A

Approved for public release;
Distribution Unlimited

The views and conclusions in this document are those of the author and should not be interpreted as necessarily representing the official policies, either expressed or implied, of the Advanced Research Projects Agency or the U.S. Government.

78 06 08 038
391 142

AB

UNCLASSIFIED

Security Classification

DOCUMENT CONTROL DATA - R & D

(Security classification of title, body of abstract and indexing annotation must be entered when the overall report is classified)

1. ORIGINATING ACTIVITY (Corporate author) Image Processing Institute University of Southern California Los Angeles, California 90007	2a. REPORT SECURITY CLASSIFICATION UNCLASSIFIED
2b. GROUP	

3. REPORT TITLE

AN INVESTIGATION INTO AN A POSTERIORI METHOD OF IMAGE RESTORATION

4. DESCRIPTIVE NOTES (Type of report and inclusive dates)
Technical Report, April 1978

5. AUTHOR(S) (First name, middle initial, last name)

John Baird Morton

6. REPORT DATE April 1978	7a. TOTAL NO. OF PAGES 195	7b. NO. OF REPS 49
8a. CONTRACT OR GRANT NO. F-33615-76-C-1203	9a. ORIGINATOR'S REPORT NUMBER(s) USCIPI Report 810	
b. PROJECT NO. ARPA Order No. 3119	9b. OTHER REPORT NO(s) (Any other numbers that may be assigned this report)	
c.	d.	

10. DISTRIBUTION STATEMENT

Approved for release: distribution unlimited

11. SUPPLEMENTARY NOTES	12. SPONSORING MILITARY ACTIVITY Advanced Research Projects Agency 1400 Wilson Boulevard Arlington, Virginia 22209
-------------------------	---

13. ABSTRACT

Two algorithms are developed which address the problem of estimating the magnitude and phase of the optical transfer function associated with a blurred image. The primary focus of the research is on the estimate of the phase of the optical transfer function. With the sharpening of one approximation, the method affords a reasonable estimate of the phase of the optical transfer function. Once an estimate of the optical transfer function has been made, the corresponding blurred image is Wiener filtered to estimate the original unblurred image. Results are demonstrated on computer simulated blurs and also on real world blurred imagery. Included is a mathematical bound on the phase of the optical transfer function.

DD FORM 1473
1 NOV 65

UNCLASSIFIED

Security Classification

Security Classification

14. KEY WORDS	LINK A		LINK B		LINK C	
	ROLE	WT	ROLE	WT	ROLE	WT
Key Words: Image Processing, Restoration, Blurring, Deconvolution, Blind Deconvolution						

ACCESSION FORM	
RTIS	White Section <input checked="" type="checkbox"/>
BDS	Over Section <input type="checkbox"/>
UNANNOUNCED	
JUSTIFICATION	
BY	
DISTRIBUTION/AVAILABILITY CODES	
Dist.	AVAIL. AND/OR SPECIAL
A	

UNCLASSIFIED
Security Classification

ACKNOWLEDGEMENT

Being reared to appreciate the virtues of thrift, it was always somewhat of a puzzle to me why one would attend a private university instead of attending the less expensive public university. After completing an A.A. degree, a B.S. degree, and a M.S. degree at different public institutions, and also after completing night courses given by other public universities, I enrolled in U.S.C. because of its convenient location, convenient schedule of classes, and because the company where I worked paid the tuition, thus removing the economic question from the picture.

At first I did not notice any substantial difference, but as time passed I began to appreciate why one would be willing to pay \$128. per unit compared to nothing per unit. At most of the public universities I had attended, I received the distinct impression that the university was not there to teach students, at least at the graduate level, but instead was more concerned with rituals and puberty rites, and the existence of the student was only a necessary evil to provide prestigious employment for the faculty. By contrast, at U.S.C. I recognized a healthy respect for the student and was impressed by an attitude that the university's reason for being was to educate the students.

For example, we all are aware of courses in graduate curricula which are clearly not relevant to one's career objectives and goals.

The nonrelevant courses are usually included as required courses in the curriculum because they are favorites of faculty members in positions of political power. Any student knows of the impossibility at a public university of substituting a more relevant course for a nonrelevant course. Yet, at U.S.C. I had little difficulty substituting courses more relevant to my career goals for courses less relevant to my career goals.

To not belabor the point I would first like to thank U.S.C. for treating me with respect as a student, for providing convenient schedules, for providing the Educational Television Center which saved me countless hours on the freeways and countless gallons of gasoline, and for providing a quality faculty and education.

I would like to thank the instructors I have had at U.S.C. in particular the three that I considered the best: Drs. Ali Habibi, Nasser Nahi, and Alexander Sawchuk.

I would like to thank the chairman of my guidance committee and thesis advisor, Dr. Harry Andrews, who not only provided sound advice and helpful direction and discussion, but who went far beyond the bounds of what would be expected of a tenured faculty member to be of assistance. I am especially appreciative of the trip he rescheduled so that I could take the qualifying exam at my convenience, of the thesis topic which he pulled from his briefcase enabling me to save several months finding an adequate topic, and for providing the opportunity to be a research assistant with the associated financial support.

Drs. Tim Strand and Alexander Sawchuk provided helpful suggestions.

For these I express my appreciation.

Lastly, I would like to thank my wife, Gina, without whose constant sacrifice and encouragement the work on the Ph.D. degree would not have begun, let alone have finished.

ABSTRACT

Two algorithms are developed which address the problem of estimating the magnitude and phase of the optical transfer function associated with a blurred image. The primary focus of the research is on the estimate of the phase of the optical transfer function. With the sharpening of one approximation, the method affords a reasonable estimate of the phase of the optical transfer function. Once an estimate of the optical transfer function has been made, the corresponding blurred image is Wiener filtered to estimate the original unblurred image. Results are demonstrated on computer simulated blurs and also on real world blurred imagery. Included is a mathematical bound on the phase of the optical transfer function.

TABLE OF CONTENTS

Chapter		Page
1	INTRODUCTION	1
	1.1 Introduction and Literature Review	1
	1.2 Research Goals	10
2	THE ALGORITHMS TO BE INVESTIGATED	11
3	NATURE OF THE PHASE	16
	3.1 Discussion	16
	3.2 Phase Bound	27
4	RESTORATION	38
5	IMPLEMENTATION AND SYSTEM PERFORMANCE	49
	5.1 Introduction	49
	5.2 On the Assumed Model	50
	5.3 On the Question of Estimating Statistical Properties of the Unknowns/Convergence	50
	5.4 On the Stability of the Iterations	73
	5.5 On Errors of Approximation	81
	5.6 On Phase Averaging	110
	5.7 On the Relaxation of One Assumption	116
	5.8 Summary	120
6	RESULTS OF SIMULATIONS	125
	6.1 Presentation of Results	125
	6.2 Discussion	127
7	RESULTS ON REAL WORLD BLURRED IMAGES	167
8	SUMMARY	187

TABLE OF CONTENTS (CONT'D)

Chapter	Page
8.1 Summary	187
8.2 Open Question	187
Appendix A. On a Theorem Concerning the Zeros of a Trigonometric Polynomial	189
REFERENCES	192

LIST OF FIGURES

Figure		Page
3.1	Principal value of the phase of the Fourier transform of a 64 x 64 pixel subimage	17
3.2	Phases corresponding to two functions	18
3.3	Phases corresponding to two functions	19
3.4	Phases corresponding to two functions	20
3.5	Phases corresponding to two functions	21
3.6	Function of Figure 3.2 together with functions corresponding to 10%, 20%, 30%, 40%, and 50% phase distortions	23
3.7	Function of Figure 3.3 together with functions corresponding to 10%, 20%, 30%, 40%, and 50% phase distortions	24
3.8	Function of Figure 3.4 together with functions corresponding to 10%, 20%, 30%, 40%, and 50% phase distortions	25
3.9	Function of Figure 3.5 together with functions corresponding to 10%, 20%, 30%, 40%, and 50% phase distortions	26
3.10	Original image	28
3.11	Phase distorted image	28
3.12	Phase distortion	28
3.13	A once sharp image reduced to garbage	29
3.14	Location of sample points	31
3.15	Representation of $H(u)$	32
3.16	Representation of $H(u)$ with $R(u)$ zero on an interval	32
3.17	Example of phase bound for $L=3$	36
4.1	Schematic of restoration process using interpolation in the Fourier domain	41
4.2	Restoration using 64 x 64 pixel sub-blocks	42

LIST OF FIGURES (CONT'D)

Figure		Page
4.3	Restoration using approach diagrammed in Figure 4.1	43
4.4	Triangularly shaped PSF	45
4.5	Comparison of approaches to restoration	46
4.6	Comparison of approaches to restoration	47
5.1	Four statistically similar images	51
5.2	Magnitude autocorrelation for $\Delta u=1$, $\Delta v=0$	53
5.3	Magnitude autocorrelation for $\Delta u=0$, $\Delta v=1$	54
5.4	Phase difference histogram for case of no windowing, $\Delta u=1$, $\Delta v=0$	57-58
5.5	Phase difference histogram for case of no windowing, $\Delta u=0$, $\Delta v=1$	59-60
5.6	Phase difference histograms for case of no windowing, on axis, $\Delta u=1$, $\Delta v=0$	63-64
5.7	Phase difference histograms for case of no windowing, on axis, $\Delta u=0$, $\Delta v=1$	65-66
5.8	Phase difference histograms for case of Parzen windowing, $\Delta u=1$, $\Delta v=0$	67-68
5.9	Phase difference histograms for case of Parzen windowing, $\Delta u=0$, $\Delta v=1$	69-70
5.10	Standard deviation of the average vs. number of samples for a sample standard deviation of 54°	72
5.11	Comparison of magnitude estimates using knowledge of the undegraded image	77
5.12	Restorations	78
5.13	Comparison of magnitude estimates without knowledge of the undegraded image	79
5.14	Phases corresponding to a function convolved aperiodically and circularly	86

LIST OF FIGURES (CONT'D)

Figure	Page
5.15 Phases corresponding to a function convolved aperiodically and circularly	87
5.16 Phases corresponding to a function convolved aperiodically and circularly	88
5.17 Phases corresponding to a function convolved aperiodically and circularly	89
5.18 Candidate windows	90
5.19 Arbitrarily chosen subimage used in windowing study	91
5.20 Magnitude differences of Fourier transforms of subimage convolved aperiodically and circularly for different windows	92
5.21 Phase differences of Fourier transforms of subimage convolved aperiodically and circularly for different windows	94
5.22 Simulation results corresponding to no windowing	99
5.23 Simulation results corresponding to no windowing	100
5.24 Simulation results corresponding to Parzen windowing	102
5.25 Simulation results corresponding to Parzen windowing	103
5.26 Vector sum A + B	108
5.27 Average vector B corresponding to H(I)	108
5.28 The resultants $A_j + B_j$	109
5.29 Representation of the complex value $H(u_1, v_1)$	111
5.30 Vectors of average phase of roughly π radians	111
5.31 Phase differences corresponding to OTF, undegraded subimages, and degraded subimages	114
5.32 Phase zones	115
5.33 An image zeroed at the edges of the subimages and then blurred	118

LIST OF FIGURES (CONT'D)

Figure		Page
5.34	Corresponding subimage to which average phase differences of zeroed image converge to	119
5.35	Phase plane	121-122
6.1	PSF corresponding to motion blur	131
6.2	Comparison of magnitude of OTF and estimate	132
6.3	Comparison of phase of OTF and estimates	133
6.4	Comparison of phase of OTF and estimates	134
6.5	Restorations	135-136
6.6	PSF of square blur	137
6.7	Comparison of magnitude of OTF and estimate	138
6.8	Comparison of phase of OTF and estimates	139
6.9	Comparison of phase of OTF and estimates	140
6.10	Restorations	141-142
6.11	PSF corresponding to double exposure	143
6.12	Comparison of magnitude of OTF and estimate	144
6.13	Comparison of phase of OTF and estimates	145
6.14	Comparison of phase of OTF and estimates	146
6.15	Restorations	147-148
6.16	PSF corresponding to quadruple exposure	149
6.17	Comparison of magnitude of OTF and estimate	150
6.18	Comparison of phase of OTF and estimates	151
6.19	Comparison of phase of OTF and estimates	152
6.20	Restorations	153-154
6.21	Triangularly shaped PSF	155

LIST OF FIGURES (CONT'D)

Figure		Page
6.22	Comparison of magnitude of OTF and estimate	156
6.23	Comparison of phase of OTF and estimates	157
6.24	Comparison of phase of OTF and estimates	158
6.25	Restorations	159-160
6.26	Triangularly shaped PSF	161
6.27	Comparison of magnitude of OTF and estimate	162
6.28	Comparison of phase of OTF and estimates	163
6.29	Comparison of phase of OTF and estimates	164
6.30	Restorations	165-166
7.1	Scene before and after photographically induced blur	168
7.2	Estimates of magnitude and phase of OTF	169
7.3	Blurred image and restorations	170
7.4	Blurred image and restorations	171
7.5	Blurred image and restorations	172
7.6	Blurred image and restorations	173
7.7	Scene before and after photographically induced blur	175
7.8	Estimates of magnitude and phase of OTF	176
7.9	Blurred image and restorations	177
7.10	Blurred image and restorations	178
7.11	Blurred image and restorations	179
7.12	Blurred image and restorations	180
7.13	Estimate of magnitude and phase of OTF	182
7.14	Blurred image and restorations	183
7.15	Blurred image and restorations	184

LIST OF FIGURES (CONT'D)

Figure	Page
7.16 Comparison of restorations with restorations using a degraded point source	185

LIST OF TABLES

Table		Page
5.1	Correlation coefficients of phase autocorrelations	56
5.2	Standard deviations of histograms	71
5.3	Average magnitude ratio of category two vectors divided by category one vectors	107
5.4	Summary of adequacy of contingencies upon which recursions depend	123
6.1	Key to restorations	126

Chapter 1

INTRODUCTION

1.1 Introduction and Literature Review

The emergence of computer technology has drastically changed methodologies in diverse fields. As the cost per calculation has been reduced by orders of magnitude, techniques which were once considered too costly are now economically feasible. In addition, concomitant technologies have emerged. One of these concomitant technologies has come to be known as "digital image processing." This dissertation is concerned with an area of digital image processing termed image restoration; simply put, the removal of a blur or degradation from an image. Everyday examples of blurred imagery would include photographs which were taken with an out of focus camera or motion blur, photographs which were taken while the camera and/or the object were moving.

Although blurred photographs are the obvious examples, the technology of image restoration can be applied to any two dimensional display of data, for example, radar maps, sonar maps, and chest x-rays.

A mathematical model of the degrading process is as follows. Let $f(x,y)$ denote the undegraded image, $g(x,y)$ denote the degraded or blurred image, and $n(x,y)$ denote additive noise. The blurring process may be modeled by equation (1-1).

$$g(x,y) = \iint_{-\infty}^{\infty} h(x,y,\xi,\eta) f(\xi,\eta) d\xi d\eta + n(x,y) \quad (1-1)$$

The function $h(x,y,\xi,\eta)$ is termed the point spread function (PSF). Note that given the degraded image $g(x,y)$, one desires to obtain the

undegraded image $f(x,y)$.

A simpler form of the PSF, $h(x,y,\xi,\eta)$, is where h is a function only of the differences between respective coordinates. That is,

$$h(x,y,\xi,\eta) = h(x-\xi, y-\eta) .$$

When this is the case, the PSF is said to be spatially invariant. The significance of the PSF being spatially invariant lies in the fact that the blur is unchanged across the image. In addition, the degraded and undegraded images are related via convolution:

$$g(x,y) = \iint_{-\infty}^{\infty} h(x-\xi, y-\eta) f(\xi, \eta) d\xi d\eta + n(x,y) . \quad (1-2)$$

Or equivalently,

$$g(x,y) = \iint_{-\infty}^{\infty} h(\xi, \eta) f(x-\xi, y-\eta) d\xi d\eta + n(x,y) .$$

The convolution integral may be Fourier transformed to yield

$$G(u,v) = H(u,v)F(u,v) + N(u,v) \quad (1-3)$$

where the capital letters denote the Fourier transforms of their respective functions represented by lower case letters. Thus, when the PSF is spatially invariant, one has the advantage of being able to utilize the relationship in the spatial domain (equation (1-2)) or the relationship in the frequency domain (equation (1-3)). $H(u,v)$ will be referred to by the term optical transfer function (OTF). Note that $h(x,y)$ and $H(u,v)$ form a Fourier pair. As a result, knowledge of either one implies knowledge of the other.

Assuming knowledge of $h(x,y,\xi,\eta)$, one must solve the integral

equation (1-1) to obtain the undegraded image $f(x,y)$. Many examples of successful restorations given a priori knowledge of $h(x,y,\xi,\eta)$ can be found in the recent literature [1-18].

In contrast, in the majority of practical situations one would not have knowledge of $h(x,y,\xi,\eta)$. Thus, if one is to utilize techniques which are known to be successful for estimating $f(x,y)$ given $g(x,y)$ and $h(x,y,\xi,\eta)$, one must first estimate $h(x,y,\xi,\eta)$.

To date techniques for estimating $h(x,y,\xi,\eta)$ from the degraded image have concentrated on spatially invariant point spread functions, and hereafter $h(x,y,\xi,\eta)$ will be assumed to be of the form $h(x-\xi, y-\eta)$. When it is clear from its context, $h(x-\xi, y-\eta)$ will sometimes be denoted by $h(x,y)$.

One possibility of estimating $h(x,y)$ is that of obtaining the estimate from an isolated unresolved point which is known to exist in the undegraded image. Accordingly, the isolated region of the undegraded image can be modeled as

$$f(x,y) \approx \delta(x-\xi, y-\eta)$$

where δ denotes a Dirac delta function [19]. Thus,

$$g_{\text{isolated}}(x,y) \approx \iint_{-\infty}^{\infty} h(\xi, \eta) \delta(x-\xi, y-\eta) d\xi d\eta \\ \approx h(x,y).$$

This technique is obviously quite limited in that it assumes the existence of an isolated unresolved point which is known to exist in the undegraded image.

Another possibility is that of estimating $h(x,y)$ from sharp edges

which are assumed to exist in the undegraded image [20]. If h is one dimensional and the edge is perpendicular to this dimension, it can be shown that

$$h(x) = -\frac{dg(x)}{dx}$$

where $g(x)$ is defined over the degraded edge and the dimension x is perpendicular to the edge.

If one assumes the possible point spread functions are from a limited set, one may use this knowledge to identify $h(x,y)$. For example, the spectrum of an out of focus image will have zeros characteristic of an out of focus OTF. Namely, of

$$H(u,v) = \frac{J_1(2\pi ar)}{ar}$$

where J_1 denotes a first order Bessel function, $r^2 = u^2 + v^2$, and a is a constant related to the severity of the blur. Note that the zeros will be circularly symmetric and functionally related to parameter a . Similarly, the spectrum of a motion blurred image will have zeros characteristic of a motion blurred OTF. Taking the spectrum of a blurred image and displaying the results may be utilized to identify some blurs [21-23].

An automated version of this idea was demonstrated by Cannon [26-28]. He assumed a set of possible blurs of out of focus, motion, and Gaussian, and automatically via the computer program he had coded, identified the blurs and parameters associated with the blurs.

A technique developed by Stockham, Cole, and Cannon [25-28] which has been moderately successful is as follows. The degraded image

is divided into subimages which may overlap. If one assumes that the extent of the PSF is small compared to the extent of the subimage and ignoring the noise term, then approximately

$$g_i(x, y) \approx \iint h(x-\xi, y-\eta) f_i(\xi, \eta) d\xi d\eta \quad (1-4)$$

where the index i denotes the i -th subimage. Taking the Fourier transform of relationship (1-4) one obtains

$$G_i(u, v) \approx H(u, v) F_i(u, v) . \quad (1-5)$$

Note that in the Fourier domain the functions are now complex.

Expressing relationship (1-5) in magnitude phase form

$$|G_i(u, v)| e^{j\theta G_i(u, v)} \approx |H(u, v)| e^{j\theta H(u, v)} |F_i(u, v)| e^{j\theta F_i(u, v)} \quad (1-6)$$

Cole [25] obtained a reasonable estimate of $|H(u, v)|$ as follows. From equation (1-6)

$$|G_i(u, v)| \approx |H(u, v)| |F_i(u, v)|$$

$$\ln |G_i(u, v)| \approx \ln |H(u, v)| + \ln |F_i(u, v)| .$$

Averaging over the N subimages:

$$\frac{1}{N} \sum_{i=1}^N \ln |G_i(u, v)| \approx \ln |H(u, v)| + \frac{1}{N} \sum_{i=1}^N \ln |F_i(u, v)| .$$

Assuming the degraded image was not so degraded that one could not tell the general class to which the undegraded image belonged, it was shown experimentally that one could use an undegraded image of the same prototype class as the degraded image as an estimate of

$$\frac{1}{N} \sum_{i=1}^N \ln|F_i(u,v)|$$

That is,

$$\frac{1}{N} \sum_{i=1}^N \ln|P_i(u,v)| \approx \frac{1}{N} \sum_{i=1}^N \ln|F_i(u,v)|$$

where P_i denotes subimages of a prototype. Thus,

$$\ln|H(u,v)| \approx \frac{1}{N} \sum_{i=1}^N \ln|G_i(u,v)| - \frac{1}{N} \sum_{i=1}^N \ln|P_i(u,v)|.$$

Cole's restorations assumed optical transfer functions of zero phase.

That is, $\theta_H(u,v) = 0$.

Cannon [26-28] assumed stationarity and used the relationship

$$\omega_g(u,v) = \omega_f(u,v)|H(u,v)|^2 + \omega_n(u,v)$$

to calculate the magnitude of the OTF where ω denotes power spectral density. ω_g was estimated from $g(x,y)$ and ω_f was estimated from an undegraded prototype image. By limiting the possible blurs to out of focus, motion, and Gaussian, Cannon was able to identify the blur and the parameters associated with the given blur. Thus, Cannon was able to estimate both the magnitude and phase of the OTF for the three possible blurs.

The estimate of the phase of the OTF, $\theta_H(u,v)$, for the general spatially invariant case has proven to be a more difficult problem. Equation (1-6) together with the relative success achieved in estimating the magnitude of the OTF suggests a similar approach with respect to the phase of the OTF. That is, from equation (1-6)

$$\bar{\theta}_{G_i}(u,v) \approx \bar{\theta}_H(u,v) + \bar{\theta}_{F_i}(u,v) .$$

Averaging, where the bar denotes averaging in some sense yet to be defined, one obtains

$$\bar{\theta}_G(u,v) \approx \bar{\theta}_H(u,v) + \bar{\theta}_F(u,v) .$$

This approach was considered and/or tried by a number of researchers [24,25,29]. The basic problem is that $\bar{\theta}_F(u,v)$ does not converge to anything meaningful, and accordingly, $\bar{\theta}_F(u,v)$ cannot be estimated by a prototype or otherwise.

A method which is closely related to the estimate of $\bar{\theta}_H(u,v)$ is a technique studied by Knox [30-32]. Knox was concerned with obtaining clear photographs of astronomical objects. Since for earth bound telescopes astronomical objects must be viewed through the atmosphere, the clarity of these photographs is generally limited by atmospheric turbulence. Knox proposed a technique whereby many short exposure photographs of the same object together with short exposure photographs of a nearby star were taken. These photographs would then be digitally processed to remove the effects of the turbulence. Denoting the i -th short exposure photograph by $g_i(x,y)$ and its corresponding short exposure point spread function by $h_i(x,y)$ we have

$$g_i(x,y) = h_i(x,y)*f(x,y)$$

where $f(x,y)$ is the undegraded photograph of the given astronomical object. Or, in the Fourier domain

$$G_i(u,v) = H_i(u,v)F(u,v) . \quad (1-7)$$

Now consider the following autocorrelation

$$G_i(u, v)G_i^*(u+\Delta u, v+\Delta v) = H_i(u, v)H_i^*(u+\Delta u, v+\Delta v)F(u, v)F^*(u+\Delta u, v+\Delta v),$$

where the superscript * denotes complex conjugation. Averaging over the multiple images, we have

$$\overline{G_i(u, v)G_i^*(u+\Delta u, v+\Delta v)} = \overline{H_i(u, v)H_i^*(u+\Delta u, v+\Delta v)F(u, v)F^*(u+\Delta u, v+\Delta v)} \quad (1-8)$$

where the bar denotes averaging. Taking the phase of equation (1-8), we have

$$\begin{aligned} \overline{\text{Phase}\{G_i(u, v)G_i^*(u+\Delta u, v+\Delta v)\}} &= \overline{\text{Phase}\{H_i(u, v)H_i^*(u+\Delta u, v+\Delta v)\}} \\ &\quad + \overline{\text{Phase}\{F(u, v)F^*(u+\Delta u, v+\Delta v)\}} \quad (1-9) \end{aligned}$$

The Phase on the left hand side of equation (1-9) can be calculated from the multiple images and the $\overline{\text{Phase}\{H_i(u, v)H_i^*(u+\Delta u, v+\Delta v)\}}$ can be shown to be negligible for atmospheric turbulence. Denoting the phase of $F(u, v)$ by $\theta_F(u, v)$, thus, we have

$$\overline{\theta_F(u, v) - \theta_F(u+\Delta u, v+\Delta v)} \approx \overline{\text{Phase}\{G_i(u, v)G_i^*(u+\Delta u, v+\Delta v)\}} \quad (1-10)$$

Note that $\theta_F(0, 0)$ is by definition equal to 0. As a result, all the phases can be calculated from the phase difference estimates in equation (1-10).

Knox demonstrated this technique with computer simulations. The mathematics of the Knox approach represent a dual analogy to that underlying the motivation for the research reported herein.

Other approaches toward estimating $\theta_H(u, v)$ involve theoretical and in some cases numerical results concerned with relationships

between the magnitude and phase of the OTF [33-42]. Although these theoretical results are mainly one dimensional and attempts to utilize the theoretical results in practical algorithms have concentrated only on the most rudimentary functions, several examples will be mentioned to indicate the present state of these approaches which attempt to extract phase information from magnitude information.

For example, Walther [34] proves the following theorem.

Let $h(\xi)$ be a square integrable function in the interval $(-\frac{1}{2}, \frac{1}{2})$ and let it be zero outside of this interval. Let $z = x + jy$ be a complex variable, and let

$$H(z) = \int_{-\frac{1}{2}}^{\frac{1}{2}} h(\xi) e^{j2\pi\xi z} d\xi$$

Let the zeros of $H(z)$ be denoted by z_i . Then any solution of the equation

$$|\bar{H}(z)| = |H(z)|$$

for which the unknown function $\bar{H}(z)$ is band-limited, must be of the form

$$\bar{H}(z) = e^{jc_1 + jc_2 z} H(z) \prod_i \frac{1-z/z_i^*}{1-z/z_i} \quad (1-11)$$

in which c_1 and c_2 are real constants and in which the product is extended over arbitrarily many zeros of $H(z)$.

Note that if all of the zeros of $H(z)$ are real, then $H(z)$ is unique up to the phase factor $e^{jc_1 + jc_2 z}$. Examples of transfer functions with real zeros include

$$H_1(z) = \frac{\sin(z)}{z},$$

$$H_2(z) = \frac{\sin^2(z)}{z^2},$$

$$H_3(z) = \cos(z).$$

Preliminary results concerning attempts equivalent to calculating transfer function phase from transfer function magnitude for transfer functions with real zeros were presented in reference [40]. These results are necessarily one dimensional since the theory has not been extended to two dimensions.

Another approach is presented in [39]. Here Gonsalves assumes knowledge of both $|h(x)|$ and $|H(u)|$ and demonstrates two techniques on one dimensional examples. The techniques show promise; however, theoretical questions regarding uniqueness and convergence are yet to be worked out nor have the algorithms been demonstrated on practical examples.

1.2 Research Goals

The ultimate goal of course is to take a blurred image and with only the knowledge of the blurred image itself remove the blur. In the spatially invariant case the realization of this ultimate goal has been thwarted by lack of an algorithm which calculates the phase of the OTF, $\theta_H(u,v)$. Presented in Chapter 2 is a method, mathematically dual to the ideas of Knox [30-32], which shows promise of reaching forward closer to this ultimate goal. The research herein investigates the feasibility and extent to which this method will estimate both the phase of the OTF and the magnitude of the OTF.

Chapter 2

THE ALGORITHMS TO BE INVESTIGATED

The technique to be studied attempts to remove degradations from an image using a minimum of knowledge. Assumed as given will be the following:

- 1) a blurred image,
- 2) the PSF is spatially invariant,
- 3) the extent of the PSF is small compared to the extent of the image,
- 4) the image is not so severely blurred such that one cannot tell the general class, for example, building, outdoor scenes, etc., to which the blurred image belongs,
- 5) and the blurred image is relatively noise free.

The emphasis will be on estimating the complex OTF. That is, both magnitude and phase of the OTF. Once the OTF has been estimated, techniques known to be successful given knowledge of the OTF will be used to estimate the undegraded image.

The general philosophy will be to assume that all quantities are continuous, and any discretizations are a corruption of the continuous process and introduce errors into the system. For example, the image, $f(x,y)$, is assumed to represent a continuous function of intensity while, likewise, the PSF, $h(x,y)$, is assumed to represent a continuous function. Since convolutions of continuous functions are continuous functions, the blurred image, $g(x,y)$, will also be assumed to be a continuous function.

Dividing the degraded image into subimages which may overlap and indexing the subimages by i ,

$$G_i(u, v) \approx H(u, v)F_i(u, v) . \quad (2-1)$$

Or equivalently,

$$G_i(u, v) = H(u, v)F_i(u, v) + E_i(u, v)$$

where $E_i(u, v)$ is the error inherent in approximation (2-1).

Forming the product

$$G_i(u, v)G_i^*(u + \Delta u, v + \Delta v) \approx H(u, v)H^*(u + \Delta u, v + \Delta v)F_i(u, v)F_i^*(u + \Delta u, v + \Delta v) . \quad (2-2)$$

Or equivalently,

$$G_i(u, v)G_i^*(u + \Delta u, v + \Delta v) = H(u, v)H^*(u + \Delta u, v + \Delta v)F_i(u, v)F_i^*(u + \Delta u, v + \Delta v) + E_i(u, v, \Delta u, \Delta v)$$

where $E_i(u, v, \Delta u, \Delta v)$ is now used to denote the error inherent in approximation (2-2).

One approach toward estimating $H(u, v)$ would be to average over the subimages. That is,

$$\begin{aligned} \frac{1}{N} \sum_{i=1}^N G_i(u, v)G_i^*(u + \Delta u, v + \Delta v) &= H(u, v)H^*(u + \Delta u, v + \Delta v) \\ &\quad \cdot \frac{1}{N} \sum_{i=1}^N F_i(u, v)F_i^*(u + \Delta u, v + \Delta v) \\ &\quad + \frac{1}{N} \sum_{i=1}^N E_i(u, v, \Delta u, \Delta v) . \end{aligned} \quad (2-3)$$

Note that $\frac{1}{N} \sum_{i=1}^N G_i(u, v)G_i^*(u + \Delta u, v + \Delta v)$ can be calculated from the

degraded image. In addition note that if $\frac{1}{N} \sum_{i=1}^N F_i(u, v) F_i^*(u+\Delta u, v+\Delta v)$ and $\frac{1}{N} \sum_{i=1}^N E_i(u, v, \Delta u, \Delta v)$ can be estimated, then the products $H(u, v)H^*(u+\Delta u, v+\Delta v)$ can be estimated. For a lossless degradation, which simply means the volume under $f(x, y)$ is equal to the volume under $g(x, y)$,

$$H(0, 0) = 1.$$

If the products $H(u, v)H^*(u+\Delta u, v+\Delta v)$ can be estimated and given $H(0, 0) = 1$, rearranging equation (2-3) we have a recursive relationship where $H^*(u+\Delta u, v+\Delta v)$ is expressed in terms of $H(u, v)$:

$$H^*(u+\Delta u, v+\Delta v) = \frac{\frac{1}{N} \sum_{i=1}^N G_i(u, v) G_i^*(u+\Delta u, v+\Delta v) - \frac{1}{N} \sum_{i=1}^N E_i(u, v, \Delta u, \Delta v)}{H(u, v) \frac{1}{N} \sum_{i=1}^N F_i(u, v) F_i^*(u+\Delta u, v+\Delta v)} \quad (2-4)$$

Equation (2-4) defines a recursion which could be utilized to simultaneously estimate both magnitude and phase of $H(u, v)$.

Another approach would be to consider the magnitude and phase of approximation (2-2) separately. First considering the magnitude

$$|G_i(u, v) G_i^*(u+\Delta u, v+\Delta v)| = |H(u, v) H^*(u+\Delta u, v+\Delta v)| |F_i(u, v) F_i^*(u+\Delta u, v+\Delta v)| + E_i^M(u, v, \Delta u, \Delta v)$$

where $E_i^M(u, v, \Delta u, \Delta v)$ denotes the error inherent in taking the magnitude of approximation (2-2). Analogous to equation (2-4), we have

$$|H^*(u+\Delta u, v+\Delta v)| = \frac{\left[\frac{1}{N} \sum_{i=1}^N |G_i(u, v) G_i^*(u+\Delta u, v+\Delta v)| - \frac{1}{N} \sum_{i=1}^N E_i^M(u, v, \Delta u, \Delta v) \right]}{|H(u, v)| \frac{1}{N} \sum_{i=1}^N |F_i(u, v) F_i^*(u+\Delta u, v+\Delta v)|} \quad (2-5)$$

Similarly, assuming $\frac{1}{N} \sum_{i=1}^N |F_i(u, v)F_i^*(u+\Delta u, v+\Delta v)|$ and $\frac{1}{N} \sum_{i=1}^N E_i^M(u, v, \Delta u, \Delta v)$ can be estimated, equation (2-5) defines a recursive relationship whereby the magnitude of $H(u, v)$ can be calculated.

Now considering the phases of approximation (2-2), we have

$$\begin{aligned} \theta_{G_i}(u, v) - \theta_{G_i}(u+\Delta u, v+\Delta v) &= \theta_H(u, v) - \theta_H(u+\Delta u, v+\Delta v) \\ &\quad + \theta_{F_i}(u, v) - \theta_{F_i}(u+\Delta u, v+\Delta v) \\ &\quad + \theta_{E_i}(u, v, \Delta u, \Delta v) \end{aligned} \quad (2-6)$$

where the subscripts G_i , H , and F_i correspond to their respective functions and $\theta_{E_i}(u, v, \Delta u, \Delta v)$ denotes the error inherent in taking the phase of approximation (2-2).

If equation (2-6) is averaged in some sense over i , and if the average value of $\theta_{F_i}(u, v) - \theta_{F_i}(u+\Delta u, v+\Delta v) + \theta_{E_i}(u, v, \Delta u, \Delta v)$ can be estimated, then rearranging equation (2-6) and noting that $\theta_H(0, 0) = 0$, one may utilize equation (2-7) to recursively estimate $\theta_H(u, v)$.

$$\begin{aligned} \theta_H(u+\Delta u, v+\Delta v) &= \theta_H(u, v) - [\overline{\theta_{G_i}(u, v)} - \overline{\theta_{G_i}(u+\Delta u, v+\Delta v)}] \\ &\quad + [\overline{\theta_{F_i}(u, v)} - \overline{\theta_{F_i}(u+\Delta u, v+\Delta v)}] \\ &\quad + \overline{\theta_{E_i}(u, v, \Delta u, \Delta v)} . \end{aligned} \quad (2-7)$$

where the bar denotes averaging in some sense yet to be defined.

In summary, 1) assuming $\frac{1}{N} \sum_{i=1}^N |F_i(u, v)F_i^*(u+\Delta u, v+\Delta v)|$ and $\frac{1}{N} \sum_{i=1}^N E_i(u, v, \Delta u, \Delta v)$ can be estimated, the recursion defined by equation (2-4) can be utilized to estimate the OTF; or 2) assuming $\frac{1}{N} \sum_{i=1}^N |F_i(u, v)F_i^*(u+\Delta u, v+\Delta v)|$ and $\frac{1}{N} \sum_{i=1}^N E_i^M(u, v, \Delta u, \Delta v)$ and

$[\theta_{F_i}(u, v) - \theta_{F_i}(u + \Delta u, v + \Delta v)] + \theta_{E_i}(u, v, \Delta u, \Delta v)$ can be estimated, equations (2-5) and (2-7) can be used to estimate the OTF.

Note that the first choice involves averaging complex numbers whereas the second choice involves averaging real numbers. On this basis alone one could conjecture that the second choice is perhaps the preferable one. A theoretical development by McGlamery [43] confirms this intuitive notion that the second choice is preferable. Further confirmation has been obtained experimentally and is consistent with McGlamery's theoretical results. Thus, hereinafter it will be assumed that equations (2-5) and (2-7) define the basic recursions to be studied.

Chapter 3

NATURE OF THE PHASE

3.1 Discussion

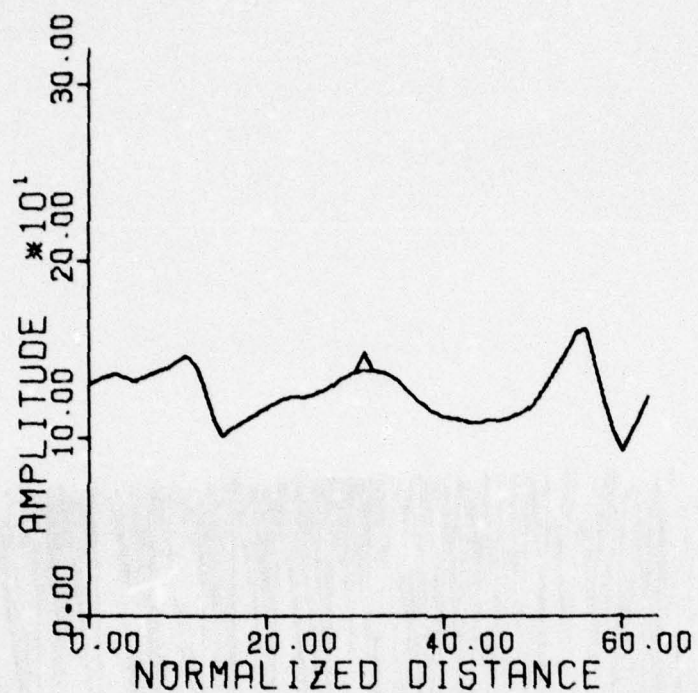
Because the emphasis of this research is on the study of a method for estimating the phase of the OTF, it is perhaps instructive to discuss and in some cases demonstrate the nature and properties of the phase in the Fourier transform domain.

Illustrated in Figure 3.1 is an attempt to present a perspective plot of the principal value of the phase of the Fourier transform of a 64 x 64 subimage arbitrarily chosen from a digital image. From Figure 3.1 it is evident that the phase corresponding to imagery is a rapidly changing and an extremely nonlinear function.

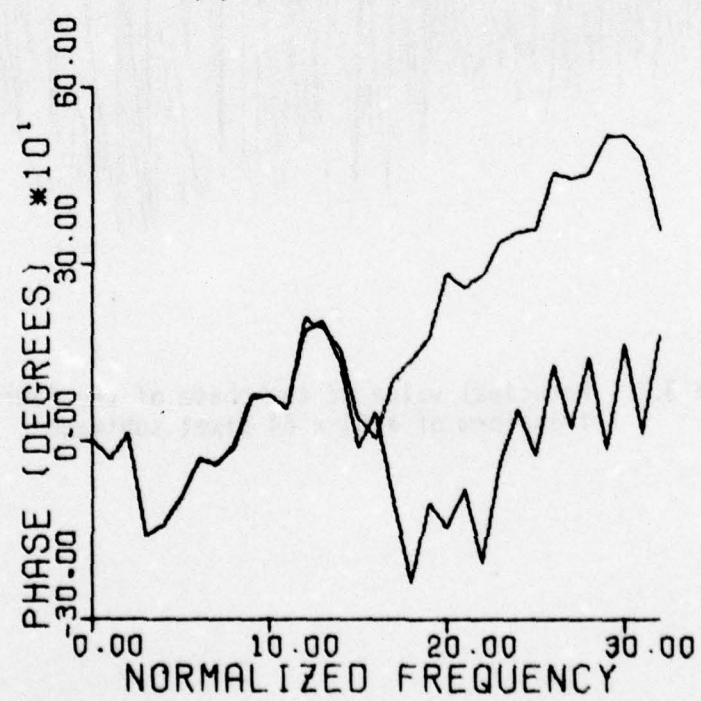
One property of the phase of the Fourier transform which merits attention is the ill-conditioned nature of the phase. That is, small changes in the spatial domain induce large changes in the phase domain. Illustrated in Each of Figures 3.2a, 3.3a, 3.4a, and 3.5a are two functions. The first function corresponds to a 64 pixel cross-section from an arbitrarily chosen image; the second function is identical to the first function except at a single point. Illustrated in Figures 3.2b, 3.3b, 3.4b, and 3.5b are the phases associated with the Fourier transforms of the respective two functions. Although some of the differences in the two phase functions are because of a possible incorrect unwrapping, the point to be made is fairly obvious, especially for the higher frequencies; the point being that small changes in a function generally will induce large changes in the phase of the



Figure 3.1 Principal value of the phase of the Fourier transform of a 64×64 pixel subimage

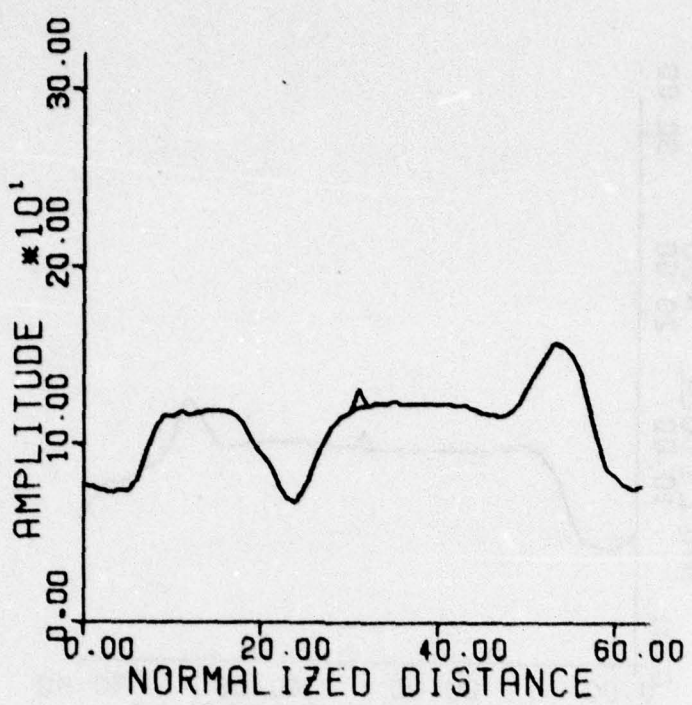


(a) two functions

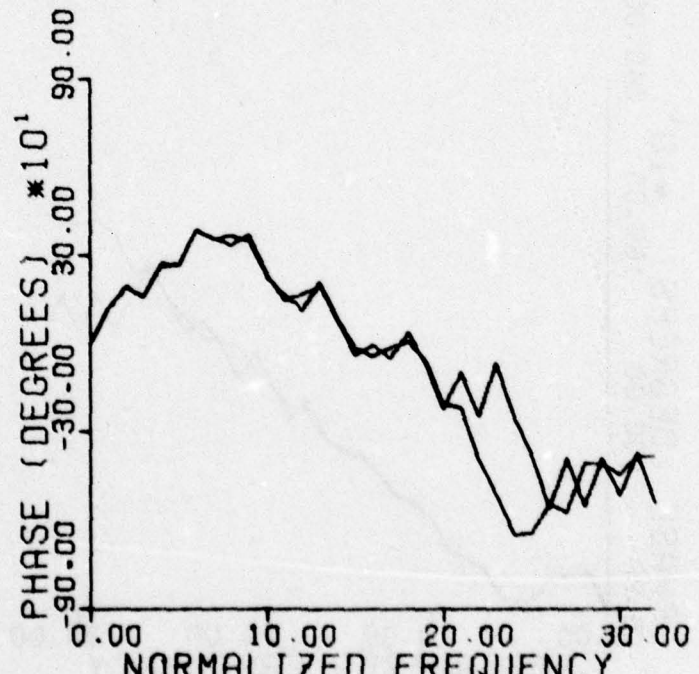


(b) corresponding phases

Figure 3.2 Phases corresponding to two functions

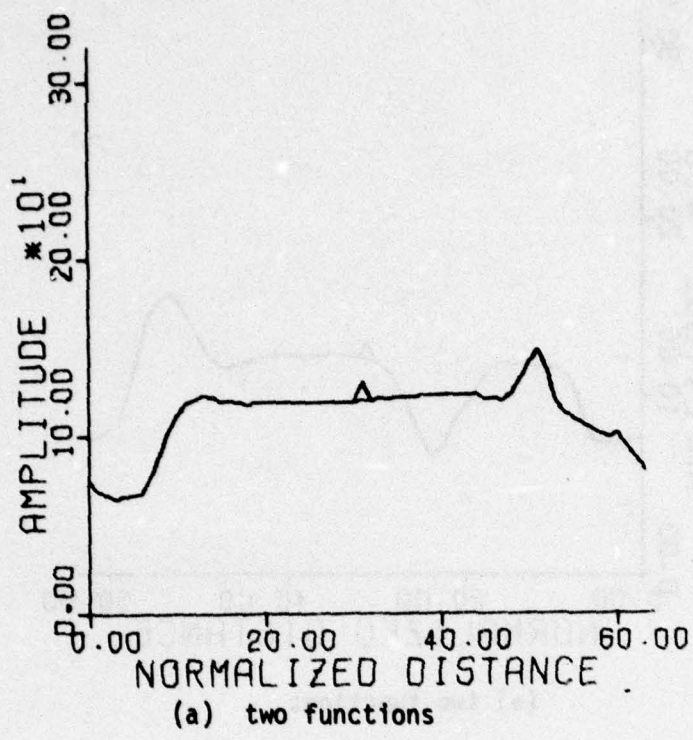


(a) two functions

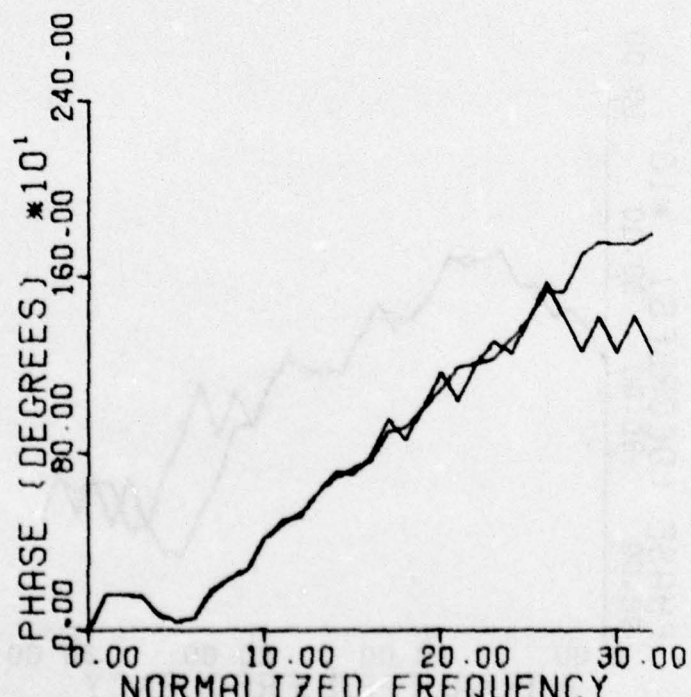


(b) corresponding phases

Figure 3.3 Phases corresponding to two functions

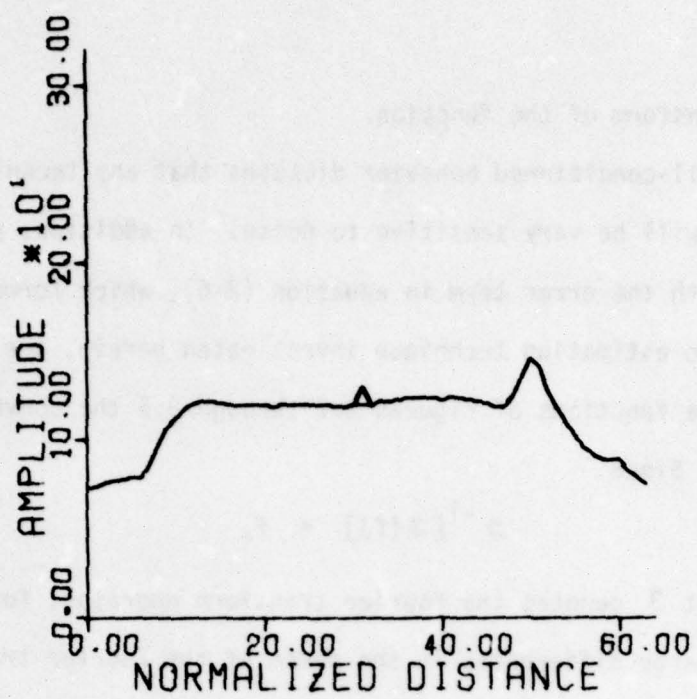


(a) two functions

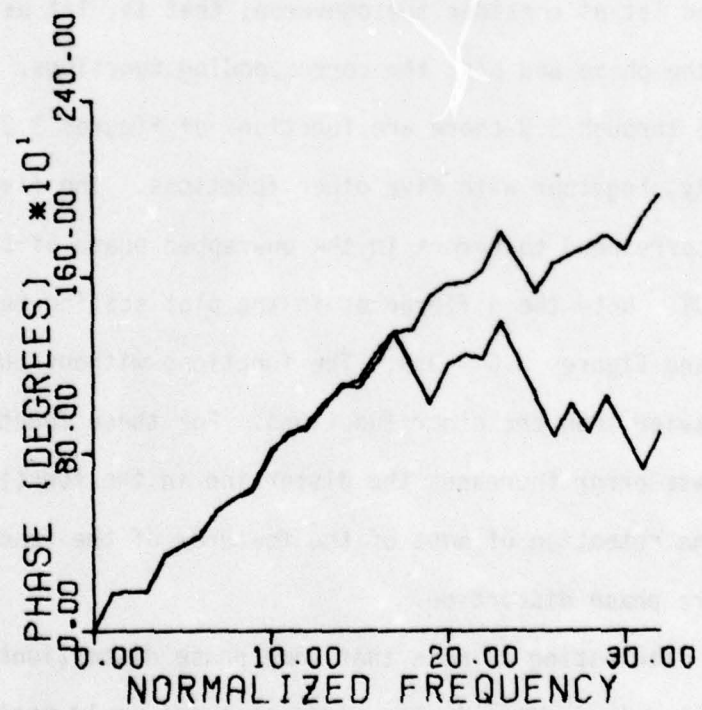


(b) corresponding phases

Figure 3.4 Phases corresponding to two functions



(a) two functions



(b) corresponding phases

Figure 3.5 Phases corresponding to two functions

Fourier transform of the function.

This ill-conditioned behavior dictates that any technique of phase estimation will be very sensitive to noise. In addition, possible problems with the error term in equation (2-6), which forms the basis of the phase estimation technique investigated herein, are foreshadowed.

For the functions of Figures 3.2 through 3.5 the converse would be true also. Since

$$\mathcal{F}^{-1}[\mathcal{F}(f)] = f,$$

where script \mathcal{F} denotes the Fourier transform operator, for these functions large differences in the phase of the Fourier transform correspond to small differences in the inverse Fourier transform. With this in mind let us consider the converse; that is, let us induce errors in the phase and plot the corresponding functions. In Figures 3.6 through 3.9 there are functions of Figures 3.2 through 3.5 respectively, together with five other functions. The five other functions correspond to errors in the unwrapped phase of 10%, 20%, 30%, 40%, and 50%. Note the differences in the plot scaling between Figures 3.2 - 3.5 and Figures 3.6 - 3.9. The functions without phase errors are plotted heavier than the other functions. For these functions increasing the phase error increases the distortion in the functions. Note, however, the retention of most of the features of the functions even under severe phase distortion.

It is interesting to note that some phase distortions do not produce a blurring effect in the sense that one would notice a smearing or fuzzing of an image. An obvious example of phase error producing no smearing is where the phase errors are the results of shifting the 22

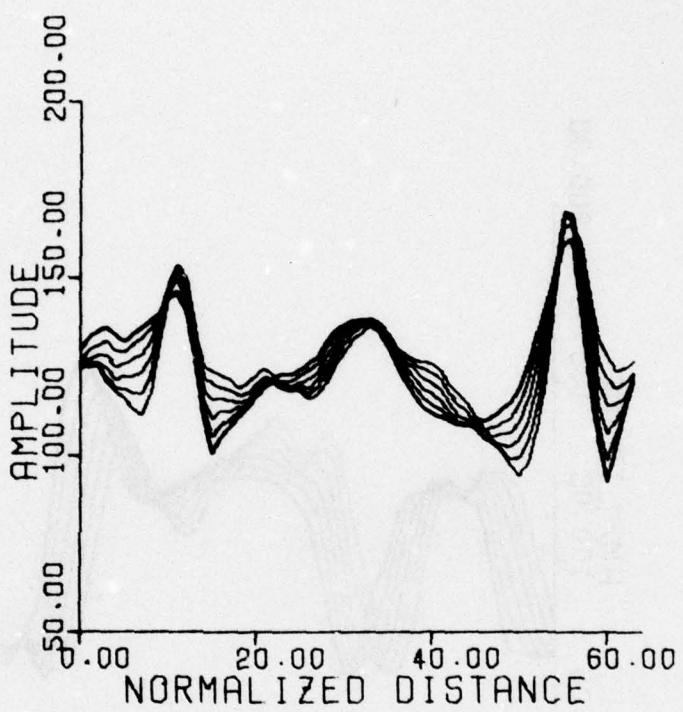


Figure 3.6 Function of Figure 3.2 together with functions corresponding to 10%, 20%, 30%, 40%, and 50% phase distortions

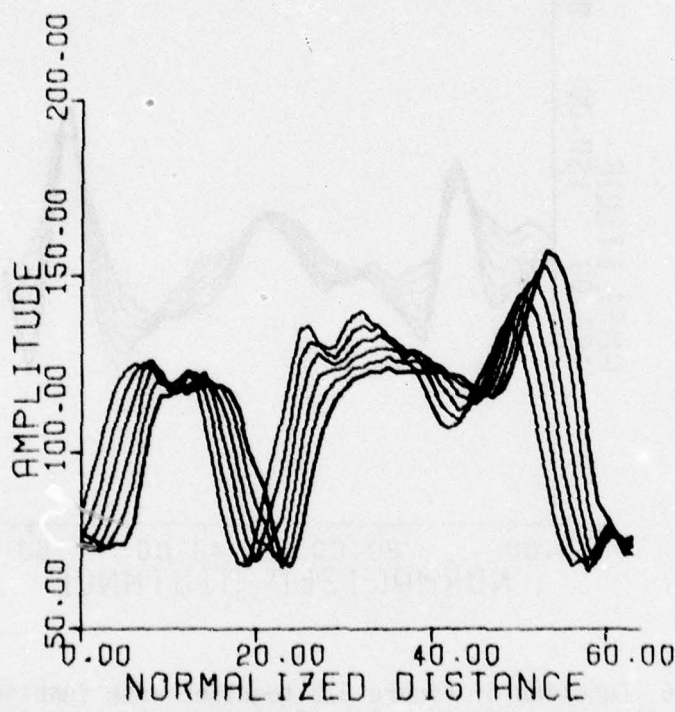


Figure 3.7 Function of Figure 3.3 together with functions corresponding to 10%, 20%, 30%, 40%, and 50% phase distortions

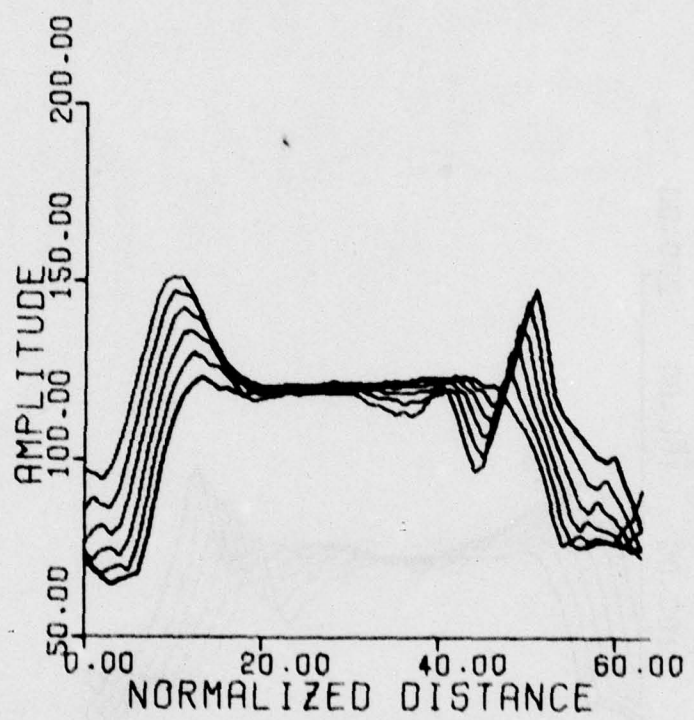


Figure 3.8 Function of Figure 3.4 together with functions corresponding to 10%, 20%, 30%, 40%, and 50% phase distortions

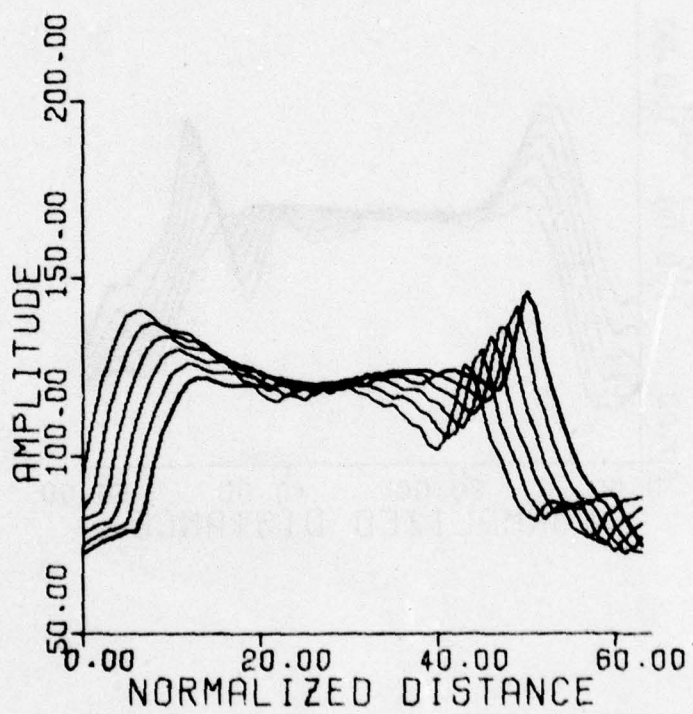


Figure 3.9 Function of Figure 3.5 together with functions corresponding to 10%, 20%, 30%, 40%, and 50% phase distortions

image. From elementary Fourier analysis we have

$$\mathcal{F}\{f(x-a, y-b)\} = e^{-j2\pi(au+bv)} F(u, v)$$

where $f(x-a, y-b)$ defines the image $f(x, y)$ shifted by an amount (a, b) .

Here there is a phase distortion but no blurring in the conventional sense of the word.

Let us now consider an example of a phase distorted image. Fourier transforming the image in Figure 3.10, multiplying the transform by the phase only filter illustrated in Figure 3.12, and then inverse transforming the result, Figure 3.11 was obtained. Although the phase errors introduced were substantial, as evidenced by Figure 3.11, very little smearing or blurring was obtained. This is consistent with the previous results whereby a substantial phase distortion in the Fourier domain induces minimal distortion in the picture domain.

The importance of the phase information should not be minimized, however. For example, if one Fourier transforms an image, retains the magnitude of the transform but replaces the phases with random phases, upon taking the inverse transform one obtains garbage. An example of this process is illustrated in Figure 3.13 whereupon a sharp, detailed image has been reduced to nonsense via this process.

3.2 Phase Bound

In this section is derived for the one dimensional case and also for the two dimensional case on axis a bound for the phase of the OTF. First let us consider the one dimensional case. Assume that the PSF is non-negative and is identically zero outside of an interval

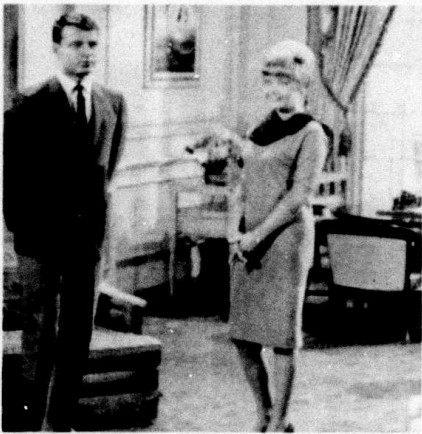


Figure 3.10 Original



Figure 3.11 Phase distorted image

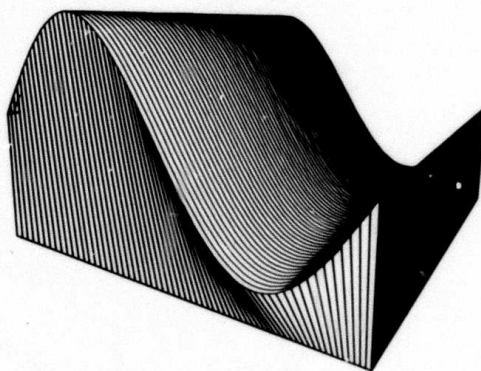


Figure 3.12 Phase distortion
(minimum amplitude = $-\pi$ radians,
maximum amplitude = π radians)

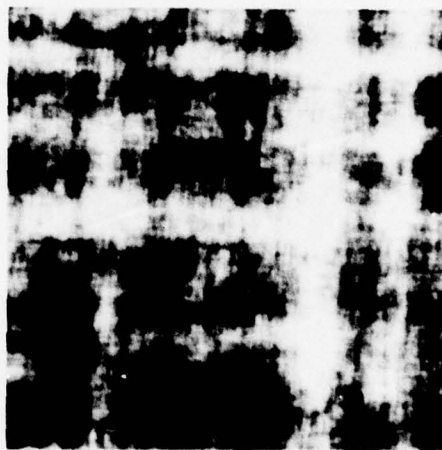


Figure 3.13 A once sharp image reduced to garbage

$[-x_1, x_1]$. Assume additionally that the PSF is sampled at the points $-\frac{N}{2}, -\frac{N}{2}+1, \dots, -1, 0, 1, \dots, \frac{N}{2}-1$ and that the samples $-L, -L+1, \dots, -1, 0, 1, \dots, L-1$, L correspond to the samples for x in the interval $[-x_1, x_1]$ as in Figure 3.14. Now consider the Fourier series

$$\begin{aligned}
 H(u) &= \sum_{k=-\frac{N}{2}}^{\frac{N}{2}-1} h(k) e^{-(j2\pi ku/N)} \\
 &= \sum_{k=-L}^L h(k) e^{-(j2\pi ku/N)} \\
 &= \sum_{k=-L}^L h(k) \cos\left(\frac{2\pi ku}{N}\right) - j \sum_{k=-L}^L h(k) \sin\left(\frac{2\pi ku}{N}\right) \\
 &= R(u) - jI(u)
 \end{aligned}$$

Note that $\theta(u) = \tan^{-1}\left\{\frac{-I(u)}{R(u)}\right\}$.

One can represent $H(u)$, for example, as in Figure 3.15 where the abscissa corresponds to the axis associated with the cosine portion of the transform, $R(u)$, the ordinate corresponds to the axis associated with the sine portion of the transform, $I(u)$, a unit of distance along the curve is du , and to each point on the curve corresponds a value u together with $R(u)$ and $I(u)$. $\theta(u)$ is the angle formed between the abscissa and the point on the curve corresponding to u .

Because the PSF, $h(x)$, is nonnegative, and ruling out the case where $h(x)=0$ everywhere, the point on the curve corresponding to $u=0$ will be on the positive $R(u)$ axis. Notice that for $\theta(u)$ to be greater than $\frac{\pi}{2}$ or less than $-\frac{\pi}{2}$ the cosine portion of the transform, $R(u)$, must go through zero. This simple idea forms the basis of the

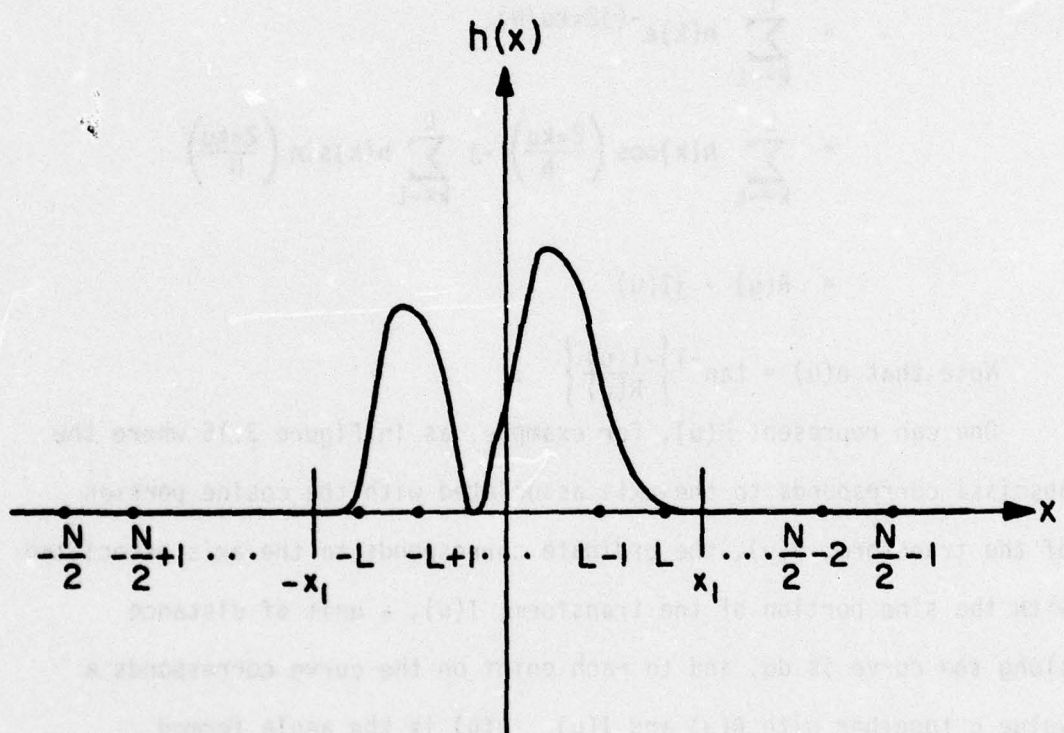


Figure 3.14 Location of sample points

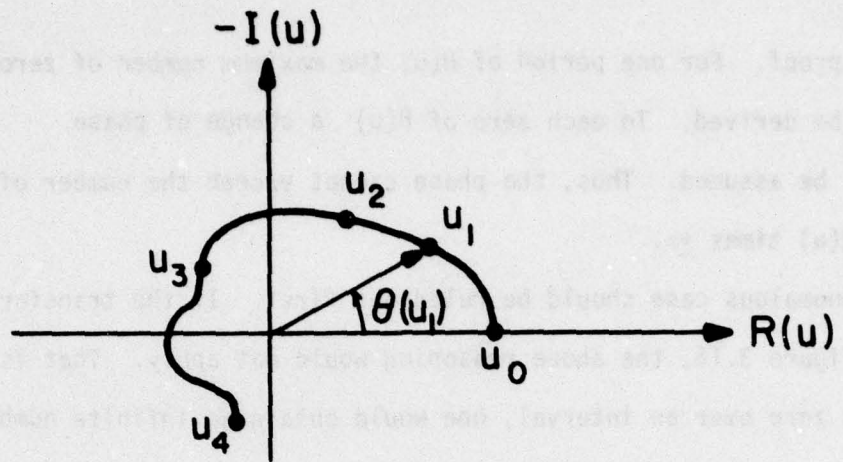


Figure 3.15 Representation of $H(u)$

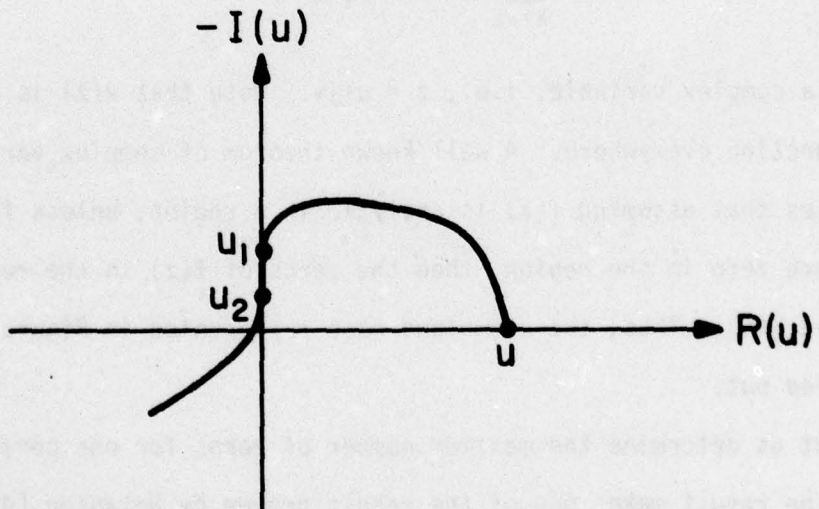


Figure 3.16 Representation of $H(u)$ with $R(u)$ zero on an interval

following proof. For one period of $H(u)$ the maximum number of zeros of $R(u)$ will be derived. To each zero of $R(u)$ a change of phase of $\pm\pi$ will be assumed. Thus, the phase cannot exceed the number of zeros of $R(u)$ times $\pm\pi$.

One anomalous case should be ruled out first. If the transform is as in Figure 3.16, the above reasoning would not apply. That is, if $R(u)$ is zero over an interval, one would obtain an infinite number of zeros. Let us consider the transform

$$R(u) = \sum_{k=-L}^L h_k \cos\left(\frac{2\pi k u}{N}\right)$$

where u is a real variable. Now consider the transform

$$R(z) = \sum_{k=-L}^L h_k \cos\left(\frac{2\pi k z}{N}\right)$$

where z is a complex variable, i.e., $z = u+jv$. Note that $R(z)$ is an analytic function everywhere. A well known theorem of complex variable theory states that assuming $f(z)$ is analytic in a region, unless $f(z)$ is everywhere zero in the region, then the zeros of $f(z)$ in the region are isolated [44]. Thus, the anomalous case represented in Figure 3.16 is ruled out.

Now let us determine the maximum number of zeros for one period of $R(u)$. The result makes use of the result proven by Natanson [45] that the trigonometric polynomial (3-1)

$$T(u) = \sum_{k=0}^L a_k \cos\left(\frac{2\pi k u}{N}\right) + b_k \sin\left(\frac{2\pi k u}{N}\right) \quad (3-1)$$

can have at most $2L$ real zeros in the interval $\left(-\frac{N}{2}, \frac{N}{2}\right]$, even if each multiple root is counted the number of times it occurs. For completeness the proof of this result is given in Appendix A.

Now consider

$$R(u) = \sum_{k=-L}^L h_k \cos\left(\frac{2\pi k u}{N}\right) .$$

Since the cosine function is an even function, we have

$$R(u) = \sum_{k=0}^L a_k \cos\left(\frac{2\pi k u}{N}\right)$$

where $a_0 = h_0$, $a_1 = h_{-1} + h_1$, $a_2 = h_{-2} + h_2, \dots, a_L = h_{-L} + h_L$.

$R(u)$ is now in the form (3-1) where $b_k = 0$, and thus, $R(u)$ can have at most $2L$ real zeros in the interval $\left(-\frac{N}{2}, \frac{N}{2}\right]$.

Again the cosine function is an even function, and since the linear combination of even functions is even, $R(u)$ will be even. As a result, if $R(u_1)$ is a zero of R , so is $R(-u_1)$. Therefore, $R(u)$ can have at most L real zeros in the interval $\left(0, \frac{N}{2}\right]$ and at most L real zeros in the interval $\left(-\frac{N}{2}, 0\right]$.

The same reasoning may be applied to $I(u)$, i.e.,

$$I(u) = \sum_{k=0}^L b_k \sin\left(\frac{2\pi k u}{N}\right)$$

where $b_0 = h_0$, $b_1 = h_1 - h_{-1}$, $b_2 = h_2 - h_{-2}, \dots, b_L = h_L - h_{-L}$.

$I(u)$ is now in the form (3-1) where $a_k = 0$, and accordingly, unless $I(u)$ is identically zero, $I(u)$ can have at most $2L$ real zeros in the interval $\left(-\frac{N}{2}, \frac{N}{2}\right]$. Since the sine function is an odd function and a

linear combination of odd functions is odd,

$$I(u) = -I(-u).$$

Thus, if $I(u_1)$ is a zero of $I(u)$, so is $I(-u_1)$ a zero. Again $I(u)$ can have at most L real zeros in the interval $\left[0, \frac{N}{2}\right]$ and at most L real zeros in the interval $\left(-\frac{N}{2}, 0\right]$.

For example, consider the case where $N=64$ and $L=3$. As u varies from 0 to 32, $R(u)$ has at most 3 real zeros, and unless $I(u)$ is identically zero, $I(u)$ has at most 3 real zeros. From Figure 3.17 note that $\theta(32)$ cannot exceed $\pm 3\pi$.

Given N and L , and assuming $I(u)$ is not identically zero,

$$-L\pi < \theta\left(\frac{N}{2}\right) < L\pi,$$

and since $\theta(u) = -\theta(-u)$

$$-L\pi < \theta\left(-\frac{N}{2}\right) < L\pi.$$

For the case in which $I(u)$ is identically zero we have

$$-L\pi \leq \theta\left(\frac{N}{2}\right) \leq L\pi \text{ and}$$

$$-L\pi \leq \theta\left(-\frac{N}{2}\right) \leq L\pi.$$

Note that the equality can be achieved. For example, if

$$R(u) = \sum_{k=-L}^L h_k \cos\left(\frac{2\pi k u}{N}\right)$$

where $h_{-L} = h_L = .5$ and $h_k = 0$ for $|k| \neq L$, then

$$R(u) = \cos\left(\frac{2\pi L u}{N}\right) \text{ and}$$

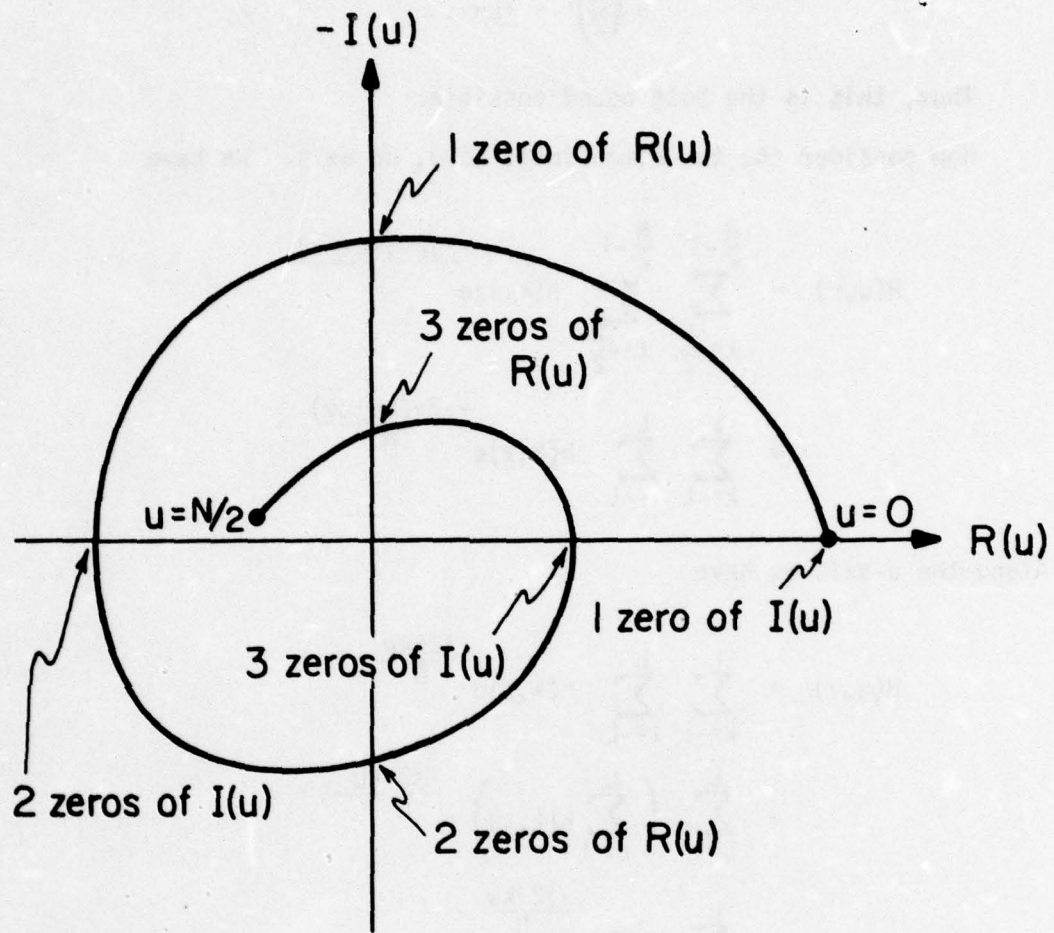


Figure 3.17 Example of phase bound for $L = 3$

$$\theta\left(\frac{N}{2}\right) = \pm L\pi .$$

Thus, this is the best bound possible.

Now consider the two dimensional case, on axis. We have

$$\begin{aligned} H(u, v) &= \sum_{k=-\frac{N}{2}}^{\frac{N}{2}-1} \sum_{\ell=-\frac{N}{2}}^{\frac{N}{2}-1} h(k, \ell) e^{\frac{-j2\pi(ku+\ell v)}{N}} \\ &= \sum_{k=-L}^L \sum_{\ell=-L}^L h(k, \ell) e^{\frac{-j2\pi(ku+\ell v)}{N}} \end{aligned}$$

Along the u -axis we have

$$\begin{aligned} H(u, v) &= \sum_{k=-L}^L \sum_{\ell=-L}^L h(k, \ell) e^{\frac{-j2\pi ku}{N}} \\ &= \sum_{k=-L}^L \left(\sum_{\ell=-L}^L h(k, \ell) \right) e^{\frac{-j2\pi ku}{N}} \\ &= \sum_{k=-L}^L \tilde{h}(k) e^{\frac{-j2\pi ku}{N}} \end{aligned}$$

But this we recognize as the one dimensional case. Thus,

$$-L\pi \leq \theta\left(\frac{N}{2}, 0\right) \leq L\pi,$$

$$-L\pi \leq \theta\left(-\frac{N}{2}, 0\right) \leq L\pi.$$

The result along the v -axis is analogous. Thus,

$$-L\pi \leq \theta\left(0, \frac{N}{2}\right) \leq L\pi ,$$

$$-L\pi \leq \theta\left(0, -\frac{N}{2}\right) \leq L\pi.$$

Chapter 4

RESTORATION

Once an estimate of both magnitude and phase of the OTF has been calculated, an estimate of the undegraded image will be made. In the Fourier domain

$$G(u,v) = H(u,v)F(u,v) .$$

One possible estimate of $F(u,v)$ would be

$$\hat{F}(u,v) = \frac{G(u,v)}{\hat{H}(u,v)} \quad \text{where } \hat{H}(u,v)$$

denotes the estimate of the OTF. This approach gives acceptable results in some cases, but in other cases zeros or near zeros in $\hat{H}(u,v)$ may provide unacceptable results.

As a general purpose filter which will give generally acceptable results, the Wiener filter defined in equation (4-1) is advantageous.

$$R(u,v) = \frac{H^*(u,v)\varphi_f(u,v)}{|H(u,v)|^2\varphi_f(u,v) + \varphi_n(u,v)} \quad (4-1)$$

where $\varphi_f(u,v)$ and $\varphi_n(u,v)$ denote power spectral densities of the undegraded image and noise respectively.

The Wiener filter is optimal in a minimum mean squared error sense. Even though the correlation between a minimum mean squared error criteria and the subjective quality of imagery is not high, the general purpose nature of the Wiener filter together with the acceptability of results obtained via Wiener filtering resulted in its exclusive use in this research.

Assuming the degraded image g is stationary in the wide sense [47], the power spectral density of the degraded image, $\omega_g(u,v)$, is the denominator in equation (4-1), i.e.,

$$\omega_g(u,v) = |H(u,v)|^2 \omega_f(u,v) + \omega_n(u,v) .$$

Accordingly, the denominator in the Wiener filter was estimated from the degraded image using a two dimensional extension of the method documented by Welch [46]. A prototype can be used to estimate $\omega_f(u,v)$.

In general a subimage size of 64×64 pixels was used in the calculations. This subimage size results in a Wiener filter of approximately 33×64 nonredundant complex numbers. Because the restorations were to be on imagery of 256×256 pixels, and the filter corresponded to imagery of 64×64 pixels, several different implementations of the restoration filter were available.

One approach would be to filter each nonredundant 64×64 pixel subimage of the degraded image.

Another approach would be to obtain the convolutional inverse of the restoration filter and convolve the degraded image with the convolutional inverse of the restoration filter. For example

$$R(u,v)G(u,v) = R(u,v)H(u,v)F(u,v)$$

$$\hat{f}(x,y) = \mathcal{F}^{-1}\{R(u,v)G(u,v)\}$$

where $\hat{f}(x,y)$ denotes an estimate of the undegraded image $f(x,y)$. Thus,

$$\hat{f}(x,y) = r(x,y)*g(x,y) .$$

This implementation requires convolving the 64×64 kernel, $r(x,y)$, 39

with the degraded image $g(x,y)$.

Still another implementation would be to interpolate the Wiener filter of approximately 33×64 nonredundant complex numbers to a Wiener filter of approximately 129×256 nonredundant complex numbers. The interpolated Wiener filter would then correspond to an image of 256×256 pixels. This implementation is diagrammed in Figure 4.1.

A comparison of the three implementations has been made. In Figure 4.2b is the resulting image after convolving the image in Figure 4.2a with a 5×5 matrix of elements of value $1/25$, i.e., a lossless PSF. Assuming knowledge of the PSF and filtering each 64×64 subimage of the degraded image, the image of Figure 4.2c was obtained. The severe artifacts at the subimage boundaries are apparent.

The reason for the artifacts merits attention. When a discrete Fourier transform (DFT) is calculated, the function being transformed is assumed to be periodic; as a result, in all likelihood the periodic version of the function will contain jump discontinuities at the ends of the period. These jump discontinuities induce artificial high frequencies in the Fourier domain and upon multiplication by the filter and subsequent inverse transforming cause severe artifacts in the restored imagery. These artifacts are usually located at sharp edges in the imagery and appear as waves propagating away from the edge boundary. Sometimes this phenomena is referred to as ringing.

Shown in Figure 4.3a is the result of using the same filter used to obtain the restoration in Figure 4.2 except the filter has been interpolated to correspond to a 256×256 image. The ringing around the image boundary is still bothersome. Multiplying the degraded

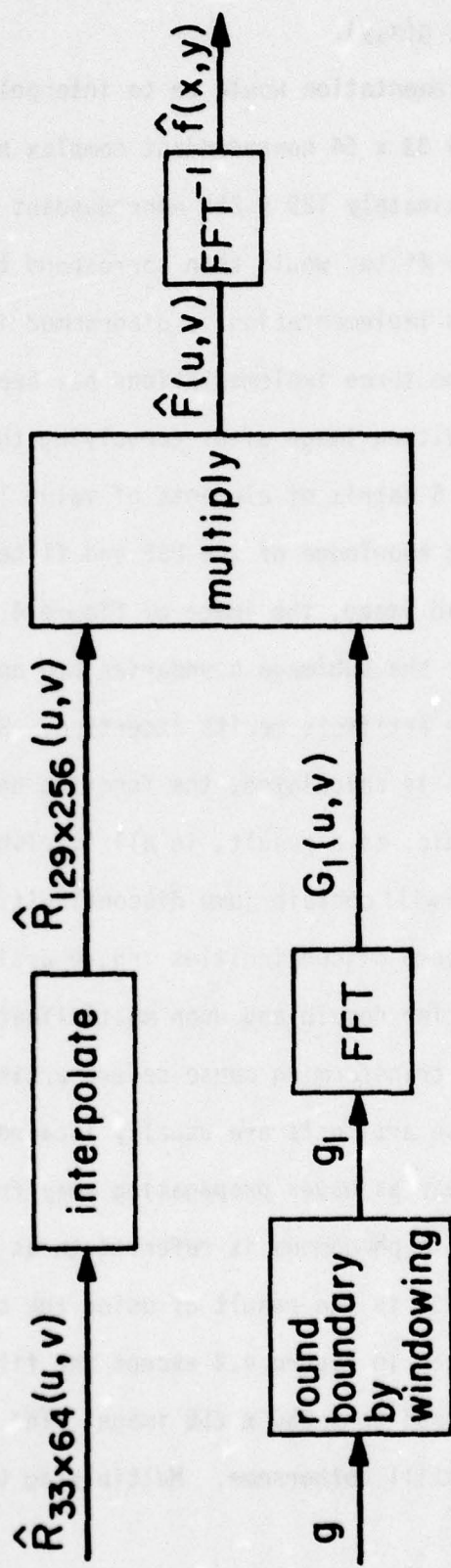
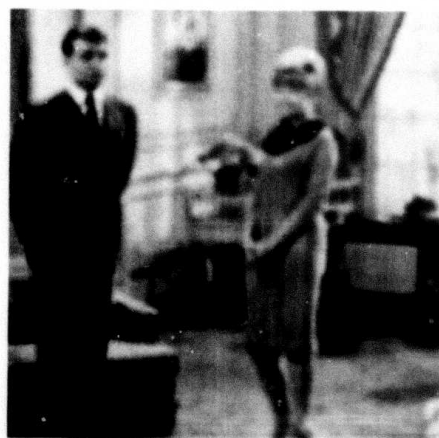


Figure 4.1 Schematic of restoration processing using interpolation in the Fourier domain

**Best
Available
Copy**



(a) original



(b) degraded



(c) restored

Figure 4.2 Restoration using 64 x 64 pixel sub-blocks



(a) with no rounding of the boundary edge



(b) with rounding of the boundary edge

Figure 4.3 Restoration using approach diagrammed in Figure 4.1

image by a window which rounds the outer boundary of the image, results in eliminating the ringing at the boundary of the restored image at the expense of removing some of the information at the boundary. This is illustrated in Figure 4.3b.

Comparison of the convolutional inverse approach and the approach diagrammed in Figure 4.1 can be seen in Figures 4.5 and 4.6. Figure 4.5a is a test pattern. Figure 4.5b is the result of convolving the PSF shown in Figure 4.4 with Figure 4.5a. Figures 4.5c and 4.5d are the result after applying the known filter via a 64 x 64 element convolutional inverse and also via the approach diagrammed in Figure 4.1 respectively. The results are essentially the same.

In Figure 4.6 is the same comparison except a different PSF has been used. In this case the discrete version of the PSF was a 9 x 9 matrix of elements of value 1/81. Figure 4.6a is the blurred image and Figures 4.6b and 4.6c are the result after applying the Wiener filter via a 64 x 64 element convolution and via the approach which interpolates the filter in the Fourier domain respectively. Again the results are essentially the same.

The OTF corresponding to the PSF diagrammed in Figure 4.4 is essentially nonzero near the frequency axes. Near the axes is where most of the energy in the frequency domain of an image is concentrated. On the other hand, the PSF used to arrive at the degraded image in Figure 4.6a has several zeros on axis. The absence of ringing in the restoration in Figure 4.5 together with the presence of ringing in the restoration in Figure 4.6 can be explained by the absence of zeros in the OTF assumed in Figure 4.5 and the presence of zeros in

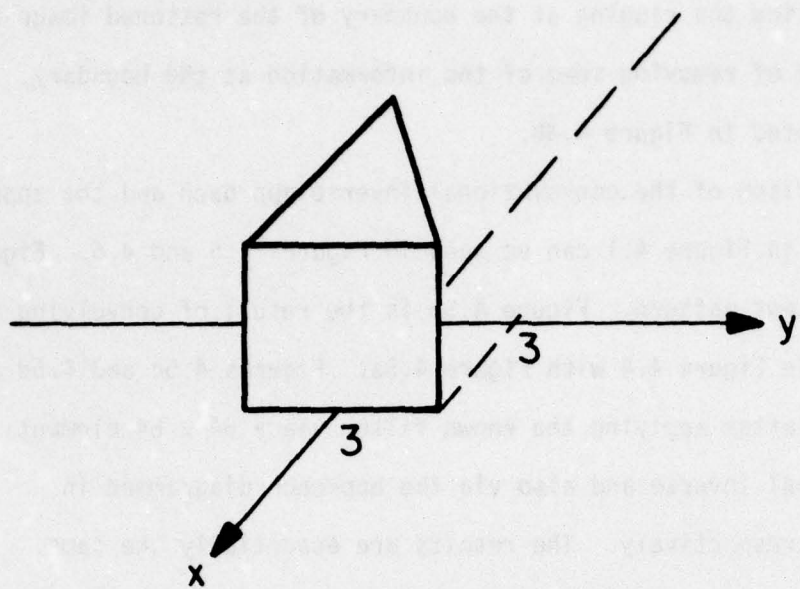
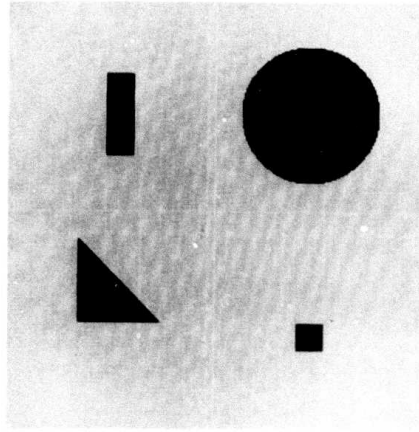
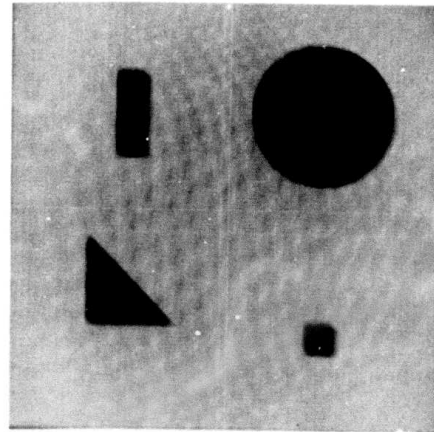


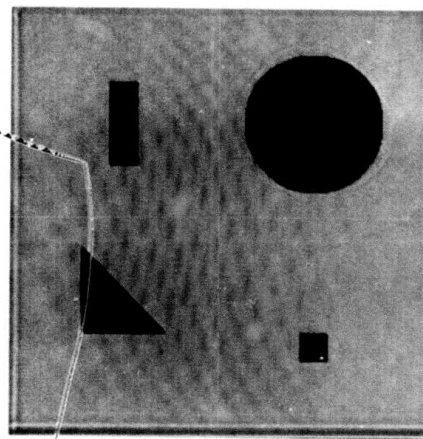
Figure 4.4 Triangularly shaped PSF



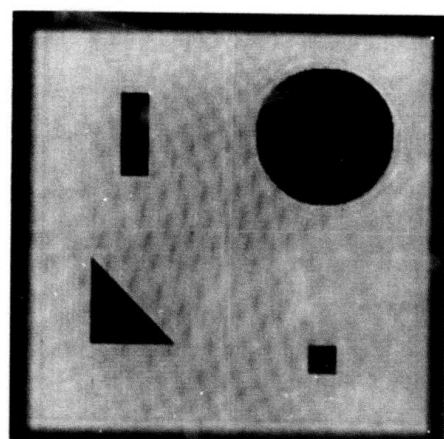
(a) test pattern



(b) degraded test pattern

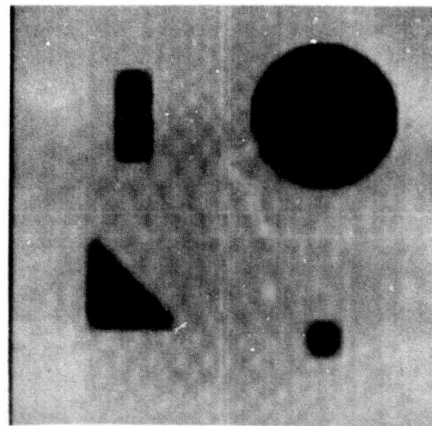


(c) restoration via convolutional inverse

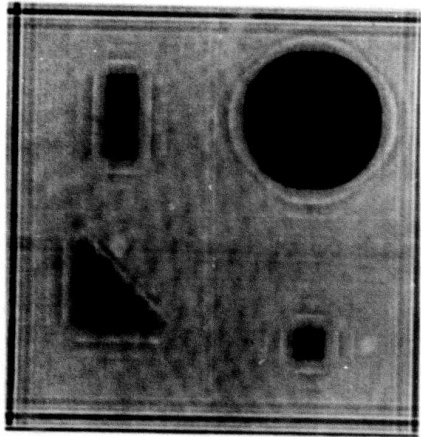


(d) restoration via interpolation of filter

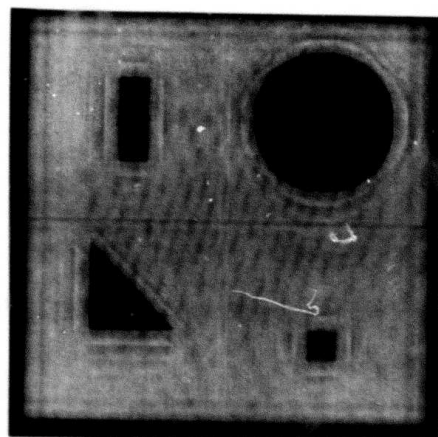
Figure 4.5 Comparison of approaches to restoration



(a) degraded test pattern



(b) restoration via convolutional inverse



(c) restoration via interpolation of filter

Figure 4.6 Comparison of approaches to restoration

the OTF assumed in Figure 4.6. For a Fourier series to adequately represent a sharp discontinuity many more terms are needed than would be needed to represent a smoother function. When an OTF contains zeros, the spatial frequencies of the undegraded image, where the zeros of the OTF are, are lost upon multiplication of the OTF and are not recoverable. Thus, the restored image lacks the spatial frequencies corresponding to the zeros of the OTF. As a result, upon restoration what were previously sharp discontinuities will be represented by fewer Fourier coefficients with the resulting ringing like artifacts at the sharp discontinuities.

Chapter 5

IMPLEMENTATION AND SYSTEM PERFORMANCE

5.1 Introduction

Equations (5-1) and (5-2) reiterate the two algorithms to be analyzed.

$$|H^*(u+\Delta u, v+\Delta v)| = \frac{\left[\frac{1}{N} \sum_{i=1}^N |G_i(u, v)G_i^*(u+\Delta u, v+\Delta v)| - \frac{1}{N} \sum_{i=1}^N \overline{E_i^M(u, v, \Delta u, \Delta v)} \right]}{\left| H(u, v) \right| \frac{1}{N} \sum_{i=1}^N |F_i(u, v)F_i^*(u+\Delta u, v+\Delta v)|} \quad (5-1)$$

with $H(0,0) = 1$.

$$\begin{aligned} \theta_H(u+\Delta u, v+\Delta v) = & \theta_H(u, v) - [\overline{\theta_{G_i}(u, v)} - \overline{\theta_{G_i}(u+\Delta u, v+\Delta v)}] \\ & + [\overline{\theta_{F_i}(u, v)} - \overline{\theta_{F_i}(u+\Delta u, v+\Delta v)}] \\ & + \overline{\theta_{E_i}(u, v, \Delta u, \Delta v)} \end{aligned} \quad (5-2)$$

with $\theta_H(0,0) = 0$.

The success or failure of the above algorithms in estimating the magnitude and phase of the OTF for real world blurred imagery is contingent on at least five conditions: 1) whether or not the mathematical model is adequate, 2) whether or not the ~~unknown~~ quantities $\frac{1}{N} \sum_{i=1}^N |F_i(u, v)F_i^*(u+\Delta u, v+\Delta v)|$ in the magnitude estimate and the ~~unknown~~ quantities $[\overline{\theta_{F_i}(u, v)} - \overline{\theta_{F_i}(u+\Delta u, v+\Delta v)}]$ in the phase estimate can be adequately estimated, 3) whether or not the averages adequately converge, 4) whether or not the iterations defined by equations (5-1) and (5-2) are stable, and 5) whether or not the error terms $\frac{1}{N} \sum_{i=1}^N \overline{E_i^M(u, v, \Delta u, \Delta v)}$ and $\overline{\theta_{E_i}(u, v, \Delta u, \Delta v)}$ in equations (5-1) and (5-2)

respectively are negligible. Assuming one does not incur the substantial expense of unwrapping phases and considers only the principal value of the phase, an additional contingency upon which the success or failure of the phase estimate depends is whether or not one can adequately overcome the problem of considering only the principal value of the phases $\theta_{F_i}(u,v)$ and $\theta_{G_i}(u,v)$.

5.2 On the Assumed Model

For the error free case experience has shown that the model of the degrading process, i.e., $g(x,y) = \iint_{-\infty}^{\infty} h(x,y,\epsilon,n) f(\epsilon,n) d\epsilon dn$, is reasonable, at least reasonable to the extent of enabling one to improve real world blurred imagery. The results of Cannon [26-28] on real world blurred imagery together with the results to be presented in Chapter 7 support this conclusion.

5.3 On the Question of Estimating Statistical Properties of the Unknowns/Convergence

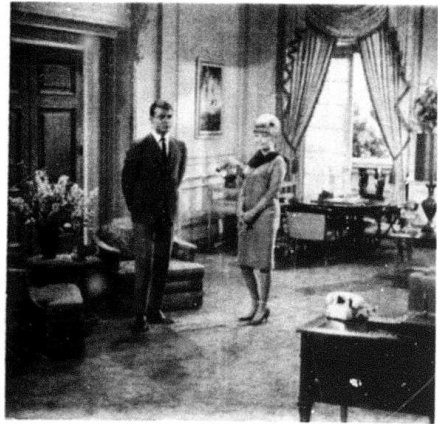
To what extent can

$$\frac{1}{N} \sum_{i=1}^N |F_i(u,v)F_i^*(u+\Delta u, v+\Delta v)| \text{ and } [\theta_{F_i}(u,v) - \theta_{F_i}(u+\Delta u, v+\Delta v)]$$

be estimated?

Using prototype images which were statistically similar, Cole [25] and Cannon [26] obtained estimates of $\frac{1}{N} \sum_{i=1}^N |F_i(u,v)|$ and $\omega_f(u,v)$ respectively. A similar approach has been studied herein. Figure 5.1 contains four statistically similar images, statistically similar in the sense that

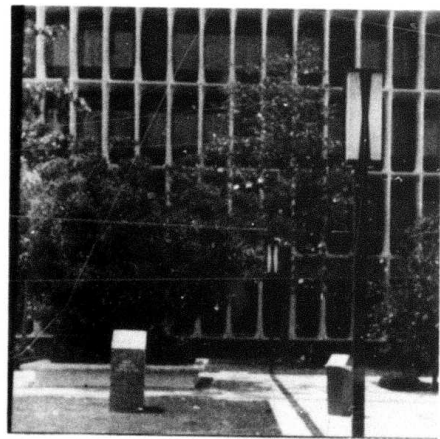
$$\frac{1}{N} \sum_{i=1}^N |F_{ik}(u,v)F_{ik}^*(u+\Delta u, v+\Delta v)|$$



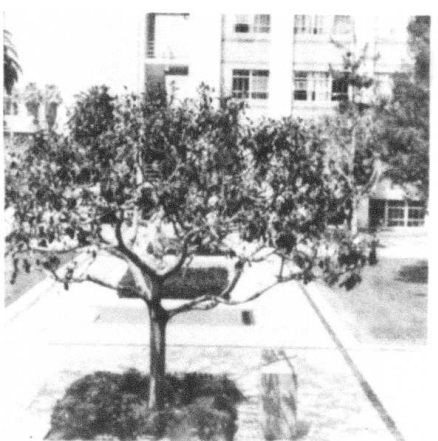
(a)



(b)



(c)



(d)

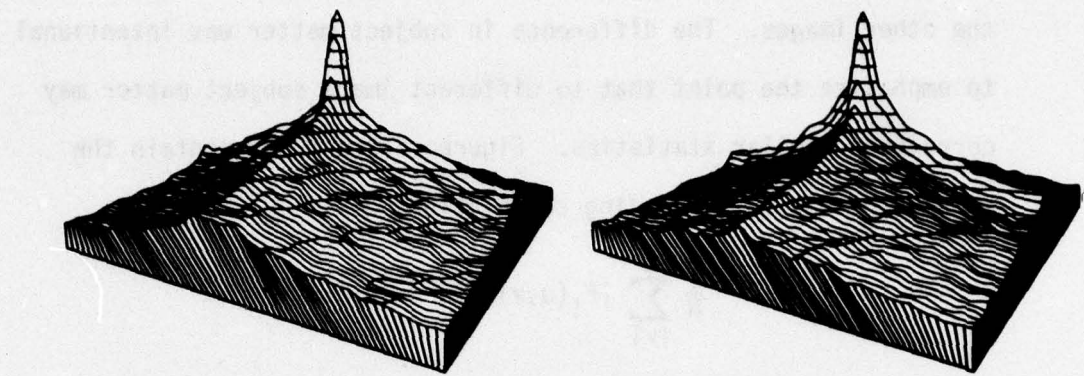
Figure 5.1 Four statistically similar images

is similar for $k=1,2,3$ and 4 where the index k denotes each of the four images. Note that the subject content of one image is different from the other images. The difference in subject matter was intentional to emphasize the point that two different image subject matter may correspond similar statistics. Figures 5.2 and 5.3 contain the results of the corresponding calculations of

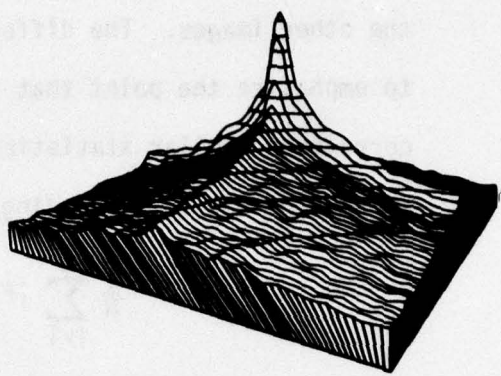
$$\frac{1}{N} \sum_{i=1}^N |F_i(u,v)F_i^*(u+\Delta u, v+\Delta v)|$$

for the four images. Figure 5.2 assumes $\Delta u=1$ in units of the fundamental frequency and $\Delta v=0$. Figure 5.3 assumes $\Delta u=0$ and $\Delta v=1$. Note the similarity of the results for the four images. The results were obtained with Parzen windowing (to be explained later), subimages of 64×64 pixels and a 50% overlap of subimages. Because the images each were represented with 512×512 pixels, N in this case was 225. The smoothness of the results can be taken as evidence that the averages have reasonably converged.

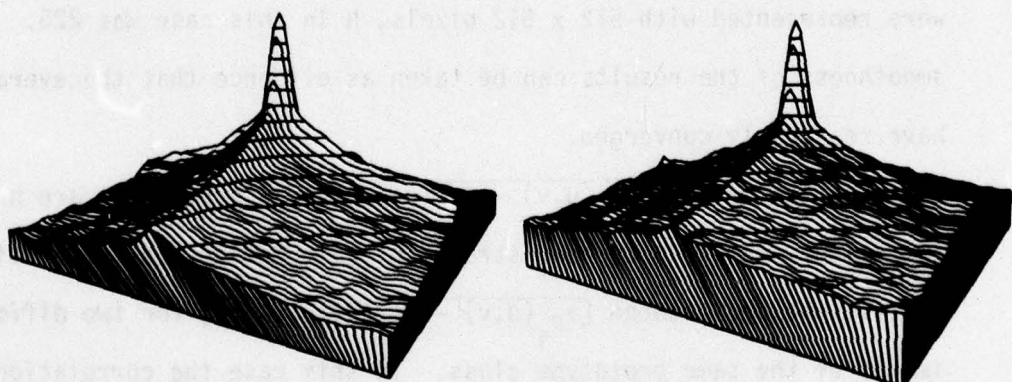
For estimating $[\theta_{F_i}(u,v) - \theta_{F_i}(u+\Delta u, v+\Delta v)]$ prototypes are not of any value. This can be demonstrated by calculating the correlation coefficient, r , between $[\theta_{F_i}(u,v) - \theta_{F_i}(u+\Delta u, v+\Delta v)]$ for two different images of the same prototype class. In this case the correlation coefficient measures the degree of tendency for small (large) average phase differences corresponding to one prototype to correspond to small (large) average phase differences corresponding to a second prototype. The correlation coefficient ranges between -1 and +1. If $r=-1$, small values in one set corresponds to large values in the second set and vice versa. If $r=0$, there is no correspondence between the two sets,



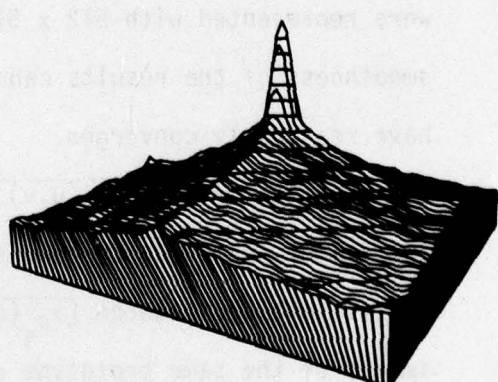
(a) autocorrelation correspond-
ing to Figure 5.1a



(b) autocorrelation correspond-
ing to Figure 5.1b

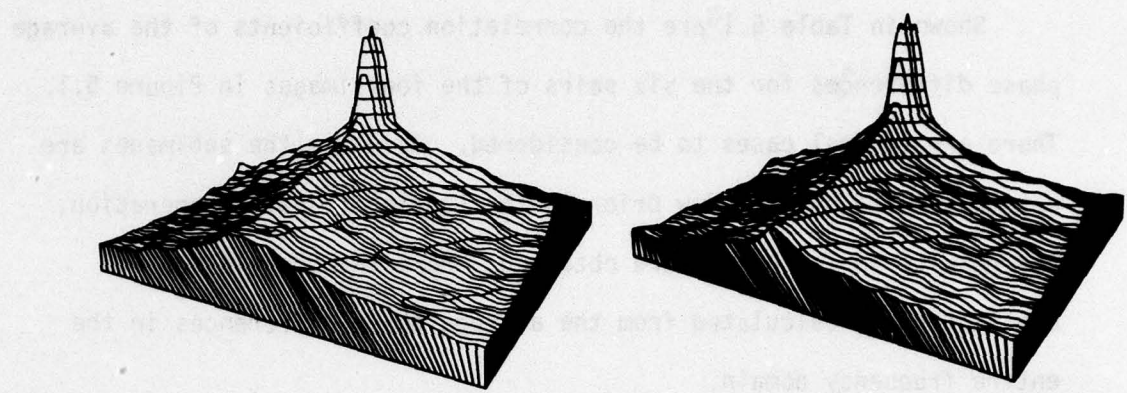


(c) autocorrelation correspond-
ing to Figure 5.1c

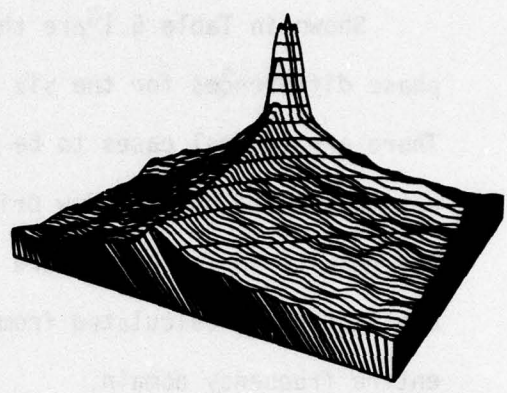


(d) autocorrelation correspond-
ing to Figure 5.1d

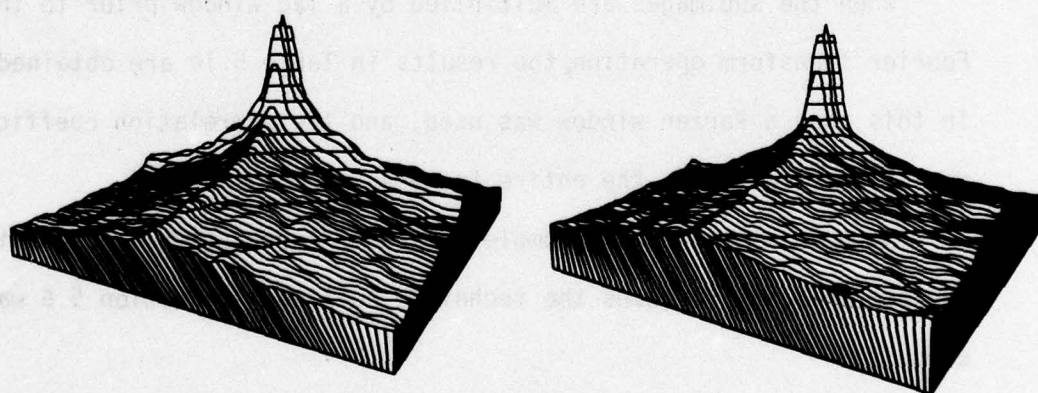
Figure 5.2 \log_{10} of magnitude autocorrelation for $\Delta u=1, \Delta v=0$



(a) autocorrelation corresponding to Figure 5.1a



(b) autocorrelation corresponding to Figure 5.1b



(c) autocorrelation corresponding to Figure 5.1c

(d) autocorrelation corresponding to Figure 5.1d

Figure 5.3 \log_{10} of magnitude autocorrelation for $\Delta u=0, \Delta v=1$

and if $r=1$, small values in one set correspond to small values in the second set and large values in one set correspond to large values in the other set.

Shown in Table 5.1 are the correlation coefficients of the average phase differences for the six pairs of the four images in Figure 5.1. There are several cases to be considered. Assuming the subimages are not multiplied by a window prior to the Fourier transform operation, the results in Table 5.1a are obtained. Here the correlation coefficient is calculated from the average phase differences in the entire frequency domain.

Again assuming the subimages are not multiplied by a window prior to the Fourier transform operation, but including only the on axis average phase differences in the calculation of the correlation coefficient, the results in Table 5.1b are obtained.

When the subimages are multiplied by a lag window prior to the Fourier transform operation, the results in Table 5.1c are obtained. In this case a Parzen window was used, and the correlation coefficient was calculated across the entire frequency domain.

Note in all cases the complete lack of correlation. To obtain the average phase differences the technique outlined in Section 5.6 was used.

These results dictate that another approach is necessary. Shown in Figures 5.4 and 5.5 are the histograms of the phase differences obtained when the four images of Figure 5.1 are divided into subimages, not multiplied by a window, and the results Fourier transformed. The histograms are across the subimages and also across the frequency

Table 5.1 Correlation coefficients between average phase differences of pairs of images of Figures 5.1

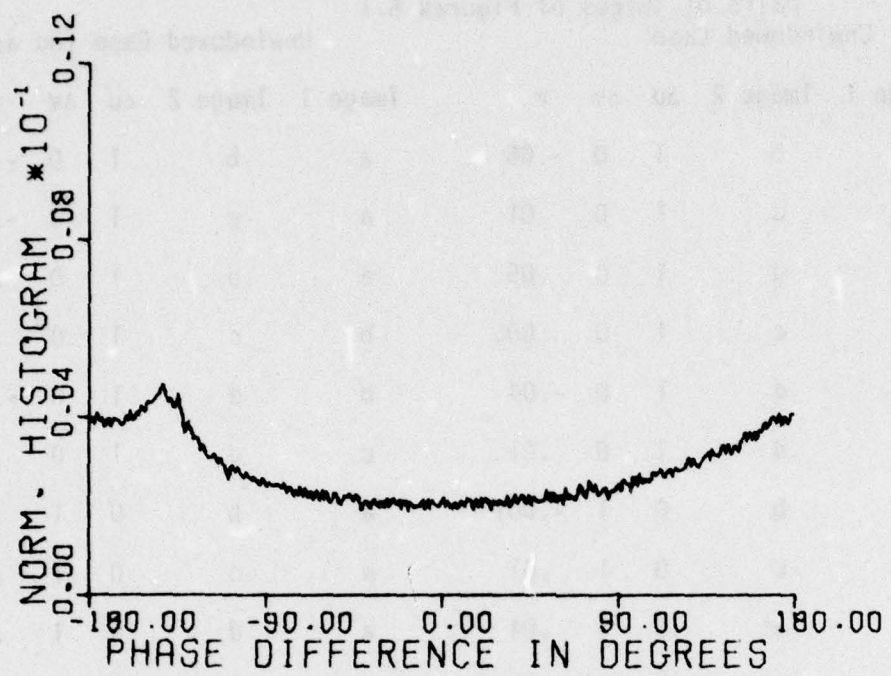
Unwindowed Case					Unwindowed Case (on axis)				
Image 1	Image 2	Δu	Δv	r	Image 1	Image 2	Δu	Δv	r
a	b	1	0	-.06	a	b	1	0	-.24
a	c	1	0	.01	a	c	1	0	-.02
a	d	1	0	.05	a	d	1	0	.16
b	c	1	0	.005	b	c	1	0	.07
b	d	1	0	-.04	b	d	1	0	-.09
c	d	1	0	.01	c	d	1	0	.21
a	b	0	1	-.001	a	b	0	1	.05
a	c	0	1	.01	a	c	0	1	.21
a	d	0	1	.04	a	d	0	1	.06
b	c	0	1	-.03	b	c	0	1	-.16
b	d	0	1	-.02	b	d	0	1	.10
c	d	0	1	-.03	c	d	0	1	.03

(a)

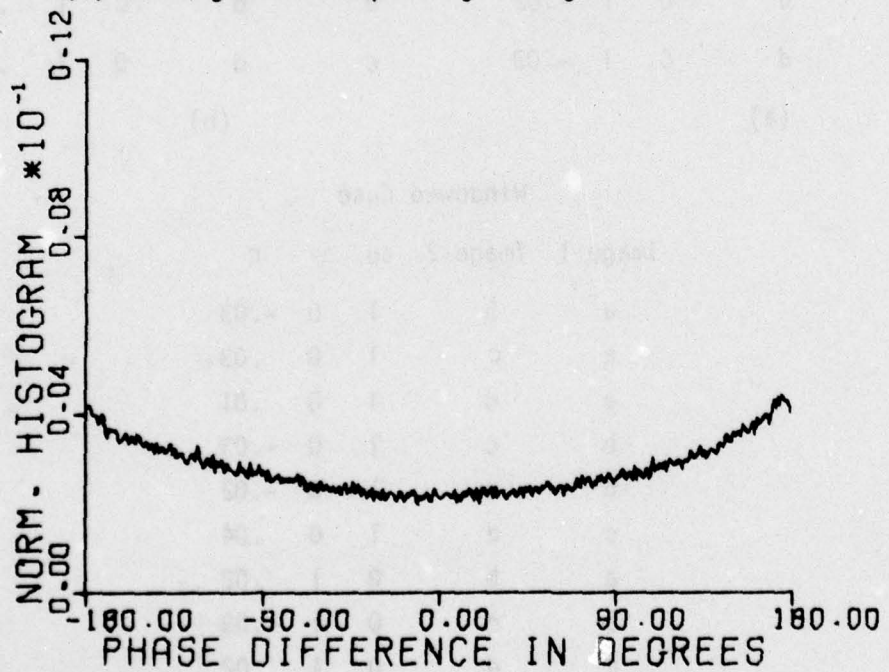
(b)

Windowed Case

Image 1	Image 2	Δu	Δv	r
a	b	1	0	-.03
a	c	1	0	.03
a	d	1	0	.01
b	c	1	0	-.03
b	d	1	0	-.02
c	d	1	0	.04
a	b	0	1	.02
a	c	0	1	-.03
a	d	0	1	.02
b	c	0	1	-.08
b	d	0	1	-.10
c	d	0	1	.08

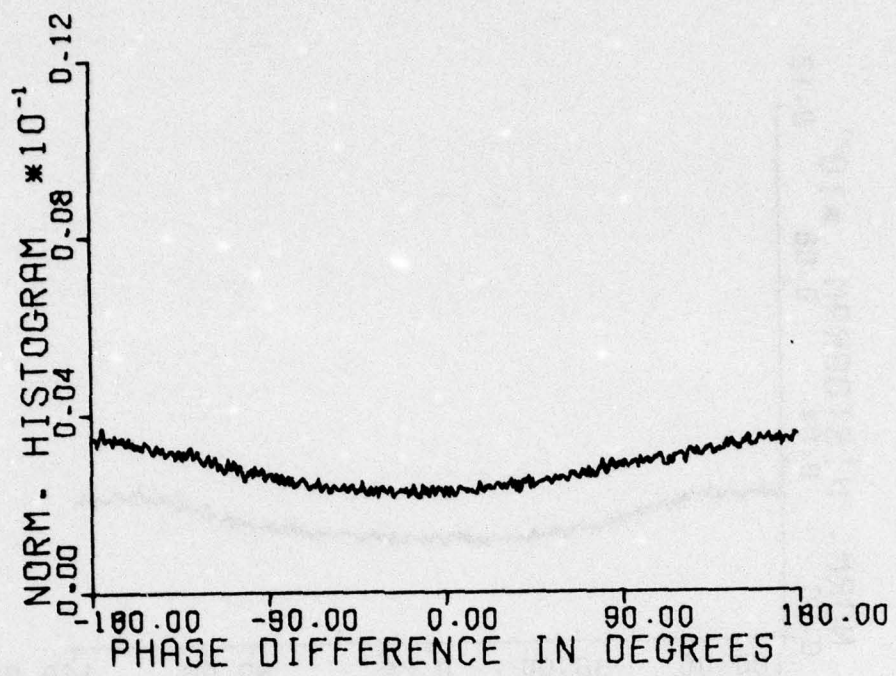


(a) histogram corresponding to Figure 5.1a

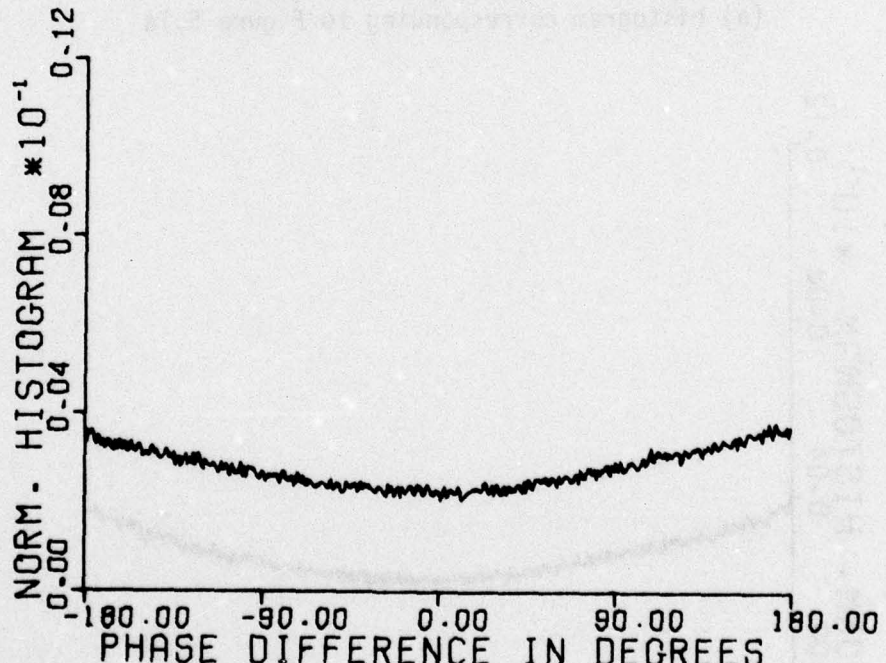


(b) histogram corresponding to Figure 5.1b

Figure 5.4 Phase difference histograms for case of no windowing, $\Delta u=1, \Delta v=0$

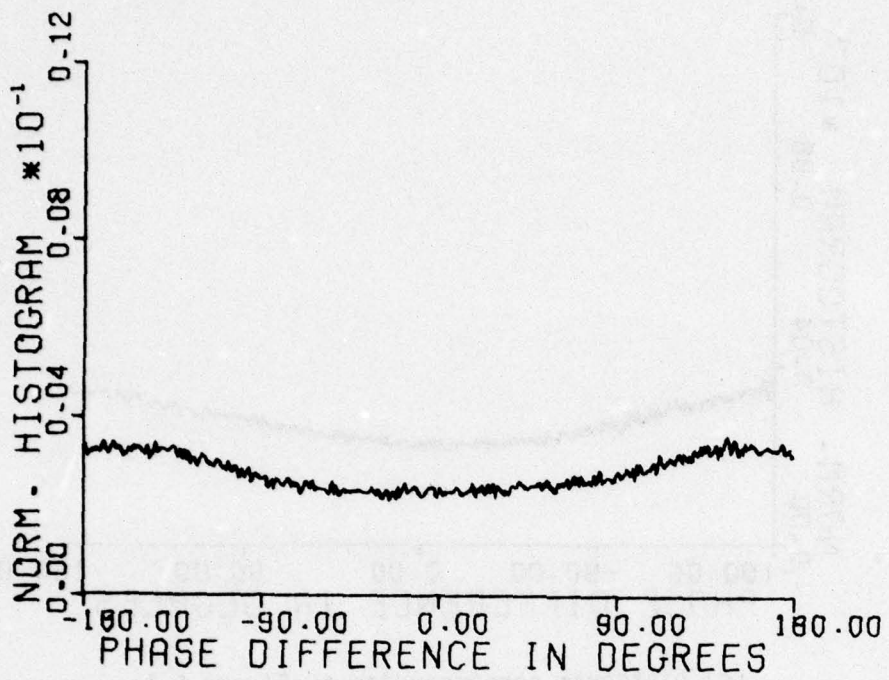


(c) histogram corresponding to Figure 5.1c

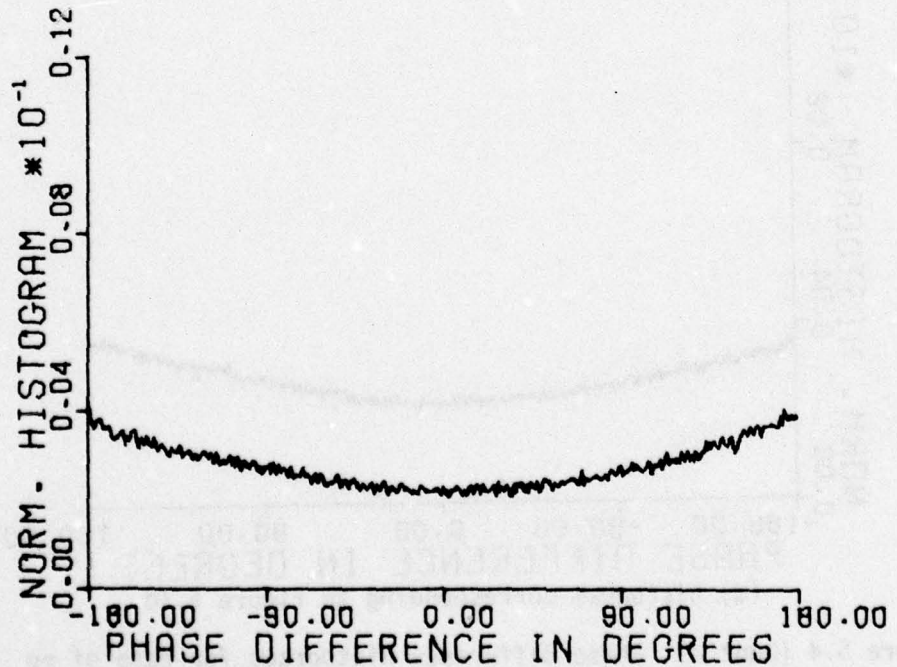


(d) histogram corresponding to Figure 5.1d

Figure 5.4 (Cont'd) Phase difference histograms for case of no windowing, $\Delta u=1, \Delta v=0$

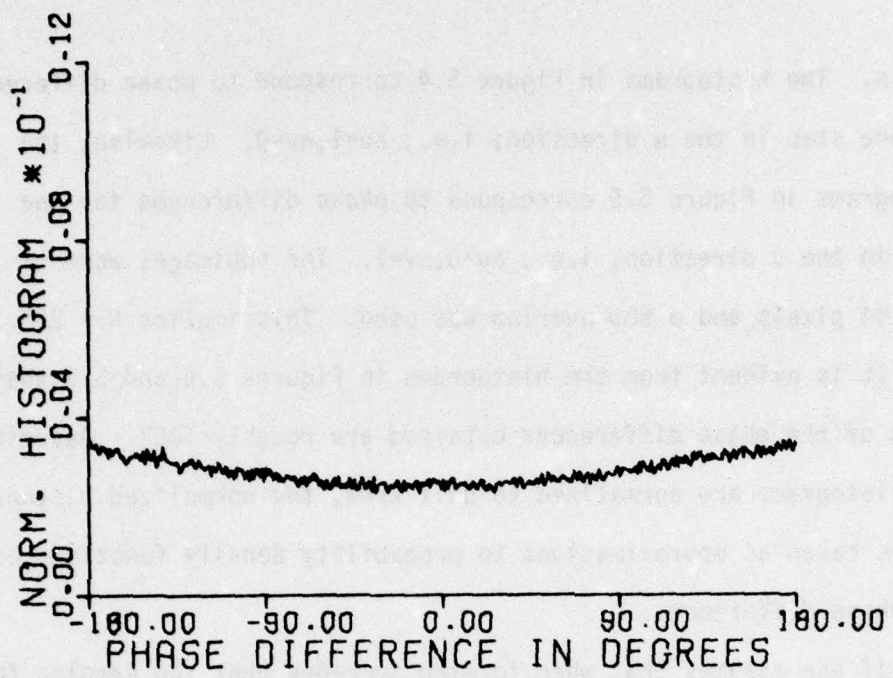


(a) histogram corresponding to Figure 5.1a

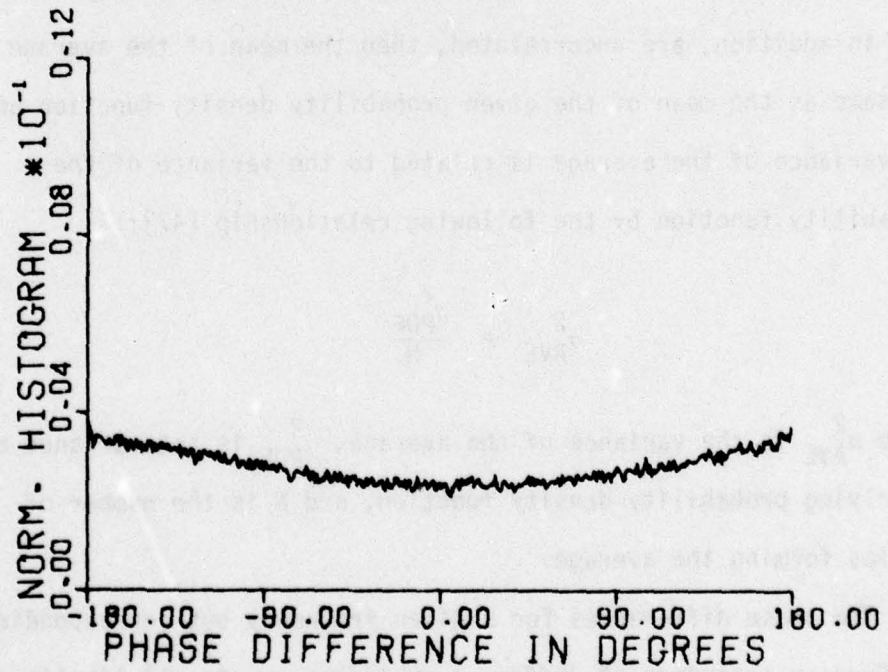


(b) histogram corresponding to Figure 5.1b

Figure 5.5 Phase difference histograms for case of no windowing,
 $\Delta u=0, \Delta v=1$ 59



(c) histogram corresponding to Figure 5.1c



(d) histogram corresponding to Figure 5.1d

Figure 5.5 (Cont'd) Phase difference histograms for case of no windowing, $\Delta u=0, \Delta v=1$

domain. The histograms in Figure 5.4 correspond to phase differences for one step in the u direction; i.e., $\Delta u=1, \Delta v=0$. Likewise, the histograms in Figure 5.5 correspond to phase differences for one step in the v direction; i.e., $\Delta u=0, \Delta v=1$. The subimages were of 64×64 pixels and a 50% overlap was used. This implies $N = 225$.

It is evident from the histograms in Figures 5.4 and 5.5 that the modes of the phase differences obtained are roughly 180° . Assuming the histograms are normalized to unit area, the normalized histograms can be taken as approximations to probability density functions of the phase differences.

If one assumes that when forming averages that the samples forming the average each come from the same probability density function and, in addition, are uncorrelated, then the mean of the average is the same as the mean of the given probability density function and the variance of the average is related to the variance of the probability function by the following relationship [47]:

$$\sigma_{\text{AVE}}^2 = \frac{\sigma_{\text{PDF}}^2}{N}$$

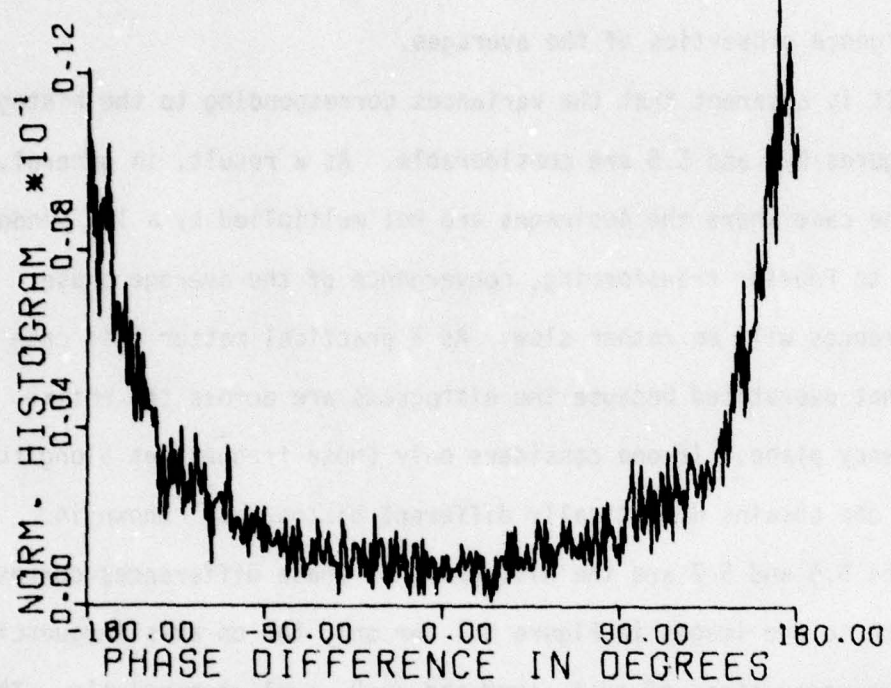
where σ_{AVE}^2 is the variance of the average, σ_{PDF}^2 is the variance of the underlying probability density function, and N is the number of samples forming the average.

The phase differences for a given frequency but corresponding to the Fourier transform of different subimages can in all likelihood be considered as independent and at least be considered uncorrelated. Thus, one may use the histograms in Figure 5.4 and 5.5 to estimate

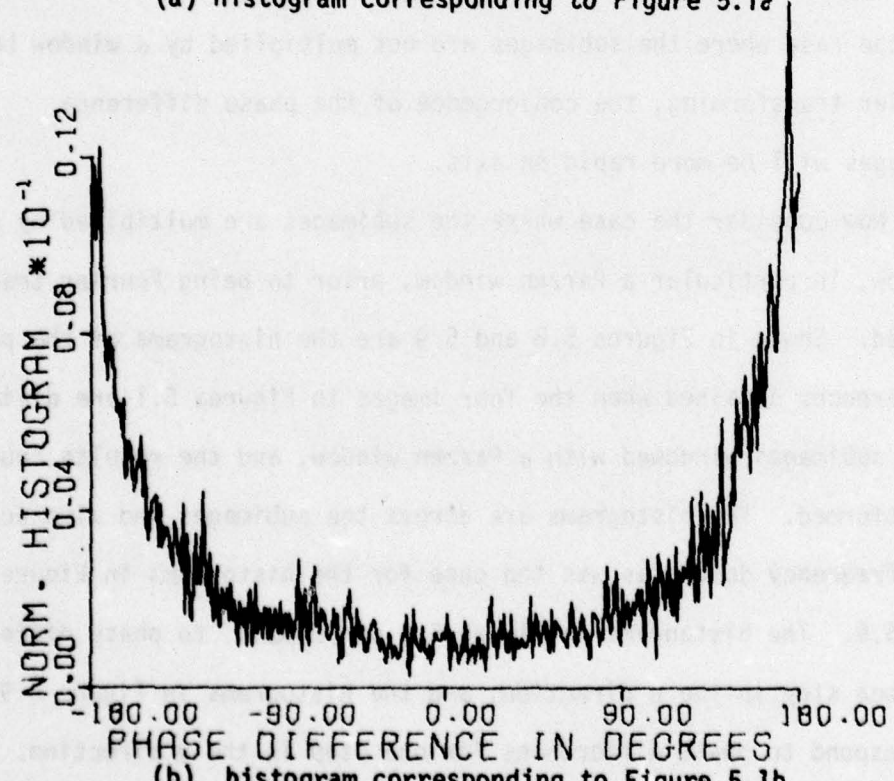
convergence properties of the averages.

It is apparent that the variances corresponding to the histograms in Figures 5.4 and 5.5 are considerable. As a result, in general, for the case where the subimages are not multiplied by a lag window prior to Fourier transforming, convergence of the average phase differences will be rather slow. As a practical matter this case is somewhat overstated because the histograms are across the entire frequency plane. If one considers only those frequencies along the axes, one obtains dramatically different histograms. Shown in Figures 5.6 and 5.7 are the histograms of phase differences corresponding to the images in Figure 5.1 for only the on axis frequencies and frequency steps of $\Delta u=1$, $\Delta v=0$ and $\Delta u=0$, $\Delta v=1$ respectively. Thus, for the case where the subimages are not multiplied by a window before Fourier transforming, the convergence of the phase difference averages will be more rapid on axis.

Now consider the case where the subimages are multiplied by a window, in particular a Parzen window, prior to being Fourier transformed. Shown in Figures 5.8 and 5.9 are the histograms of the phase differences obtained when the four images in Figures 5.1 are divided into subimages, windowed with a Parzen window, and the results Fourier transformed. The histograms are across the subimages and also across the frequency domain as was the case for the histograms in Figures 5.4 and 5.5. The histograms in Figure 5.8 correspond to phase differences for one step in the u direction, and the histograms in Figure 5.9 correspond to phase differences for one step in the v direction. Note that the mode for the windowed case is 0, whereas the mode is 180° for

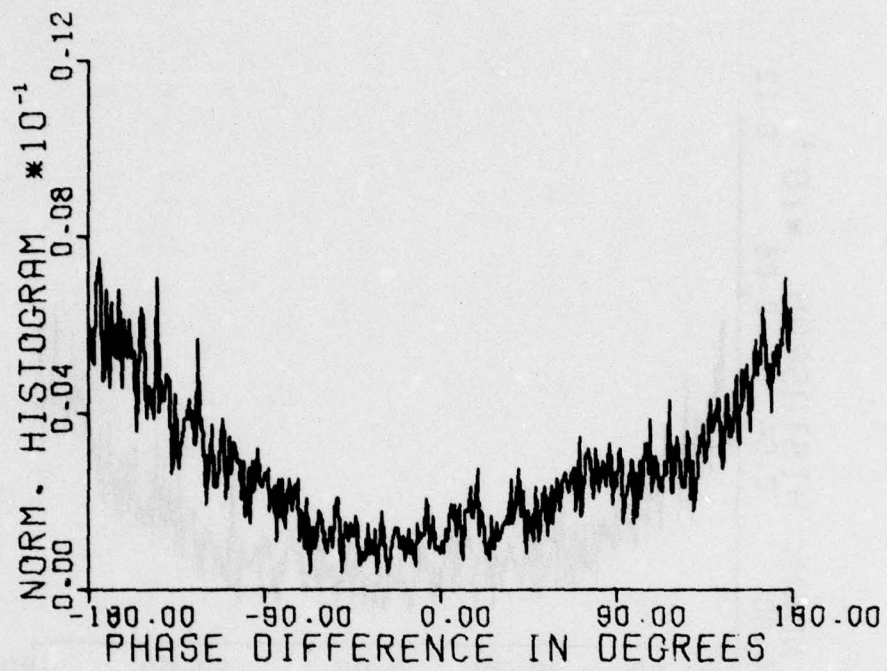


(a) histogram corresponding to Figure 5.1a

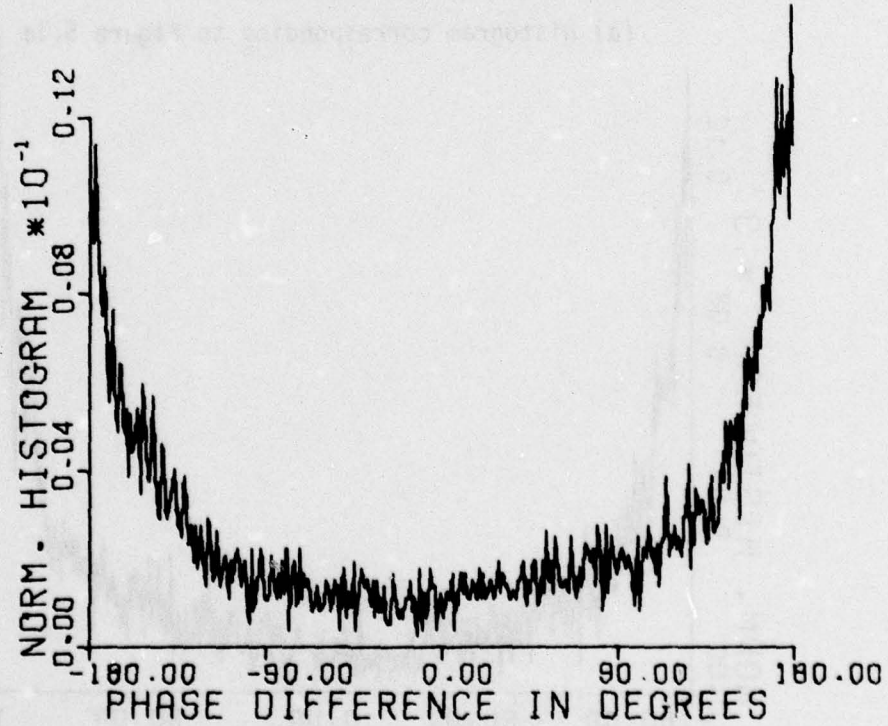


(b) histogram corresponding to Figure 5.1b

Figure 5.6 Phase difference histograms for the case of no windowing,
on axis, $\Delta u=1$, $\Delta v=0$

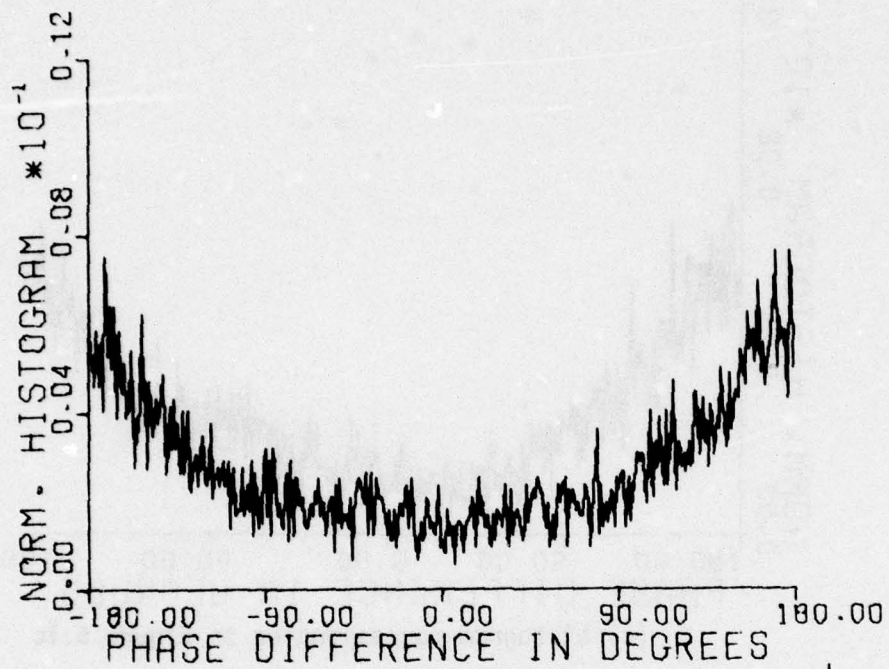


(c) histogram corresponding to Figure 5.1c

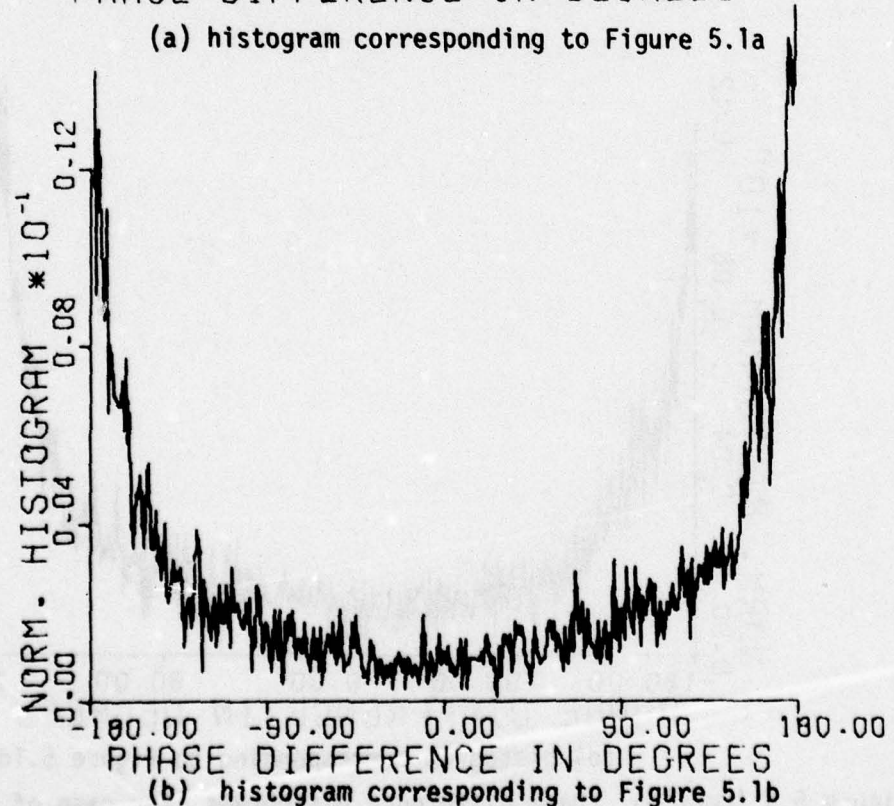


(d) histogram corresponding to Figure 5.1d

Figure 5.6 (Cont'd) Phase difference histograms for case of no windowing, on axis, $\Delta u=1$, $\Delta v=0$



(a) histogram corresponding to Figure 5.1a



(b) histogram corresponding to Figure 5.1b

Figure 5.7 Phase difference histograms for case of no windowing,
on axis, $\Delta u=0$, $\Delta v=1$

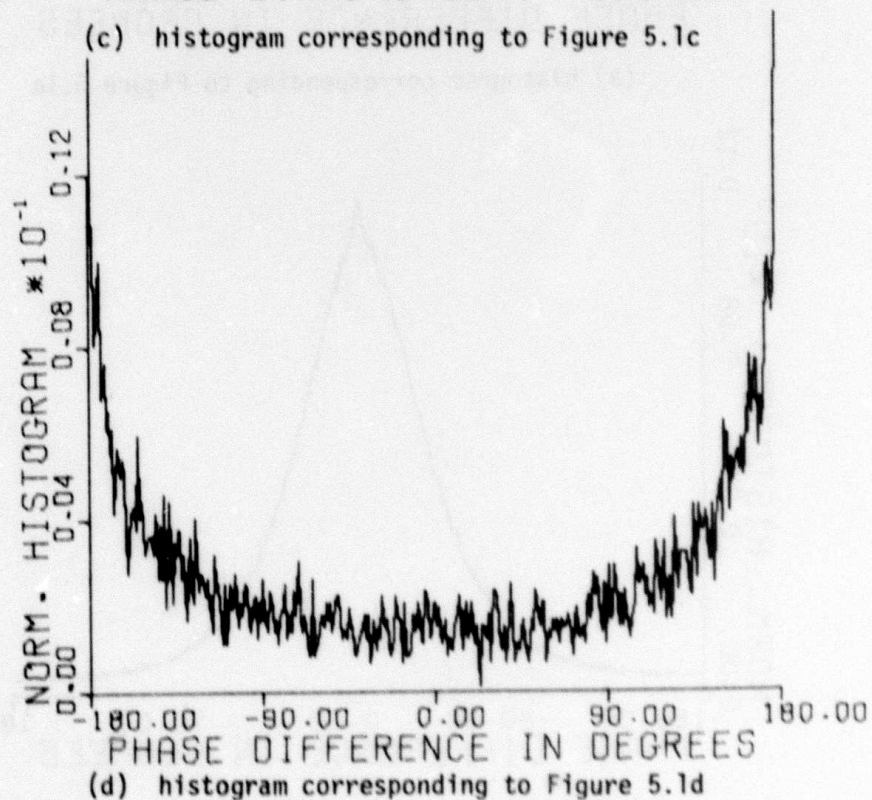
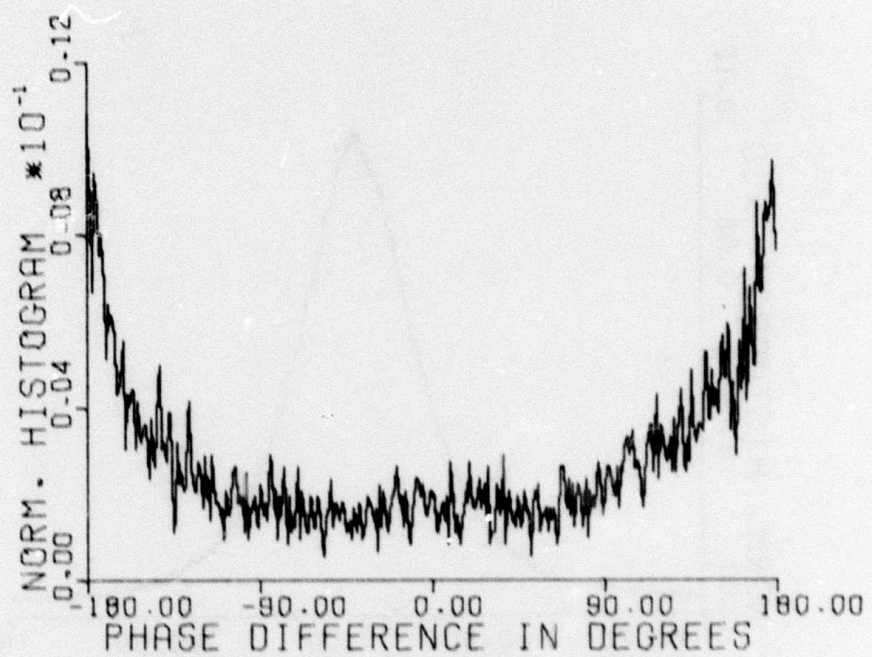
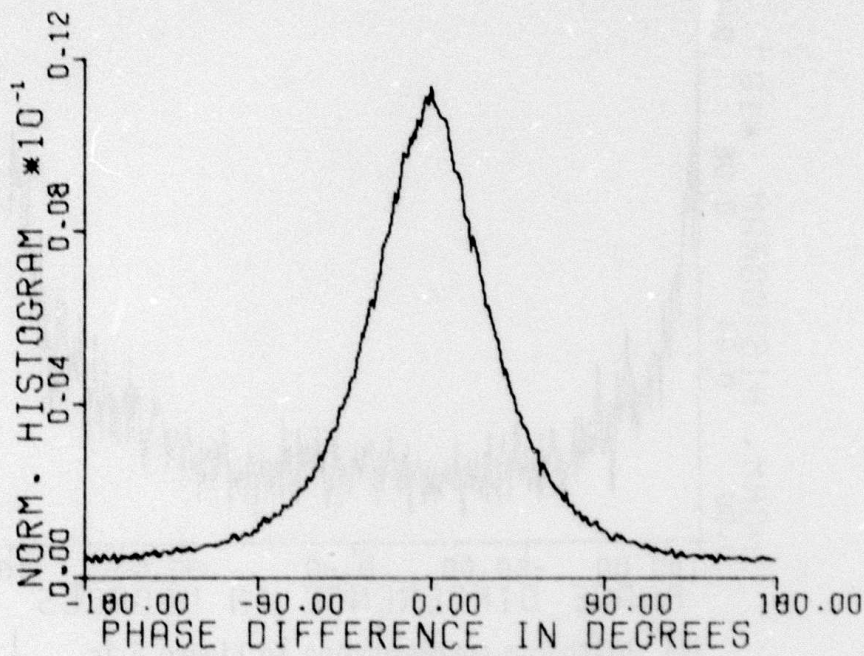
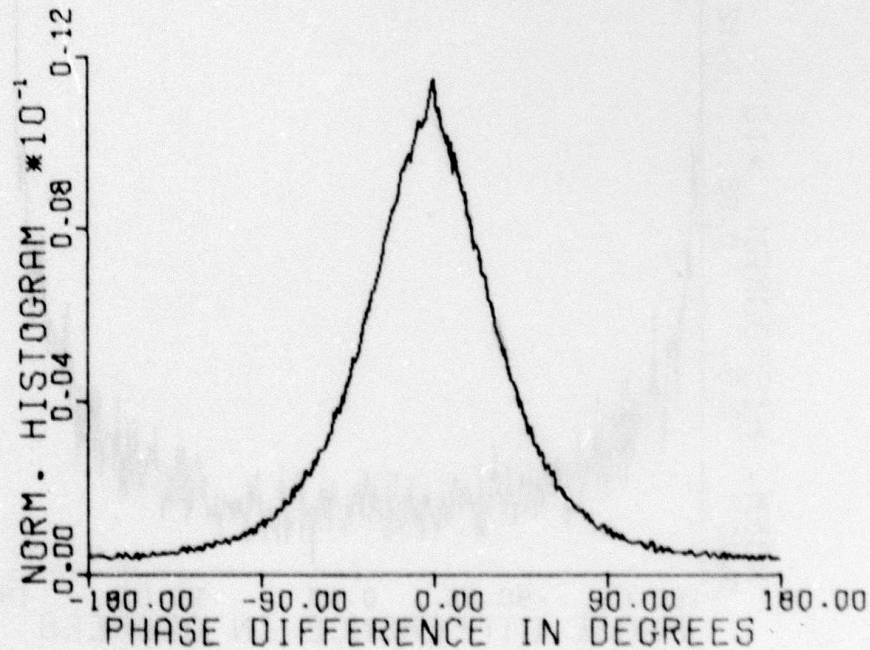


Figure 5.7 (Cont'd) Phase difference histograms for case of no windowing, on axis, $\Delta u=0$, $\Delta v=1$

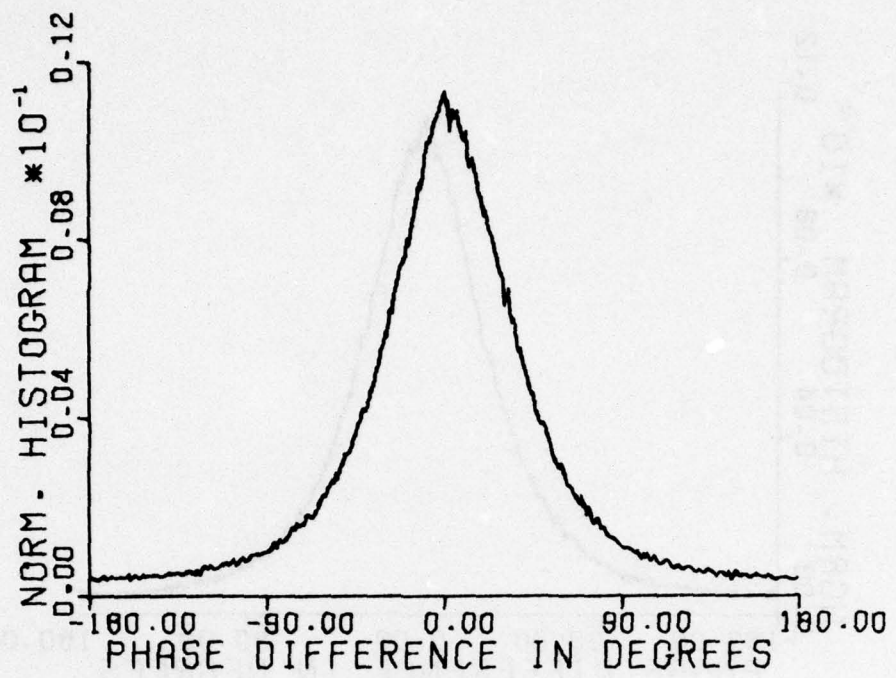


(a) histogram corresponding to Figure 5.1a

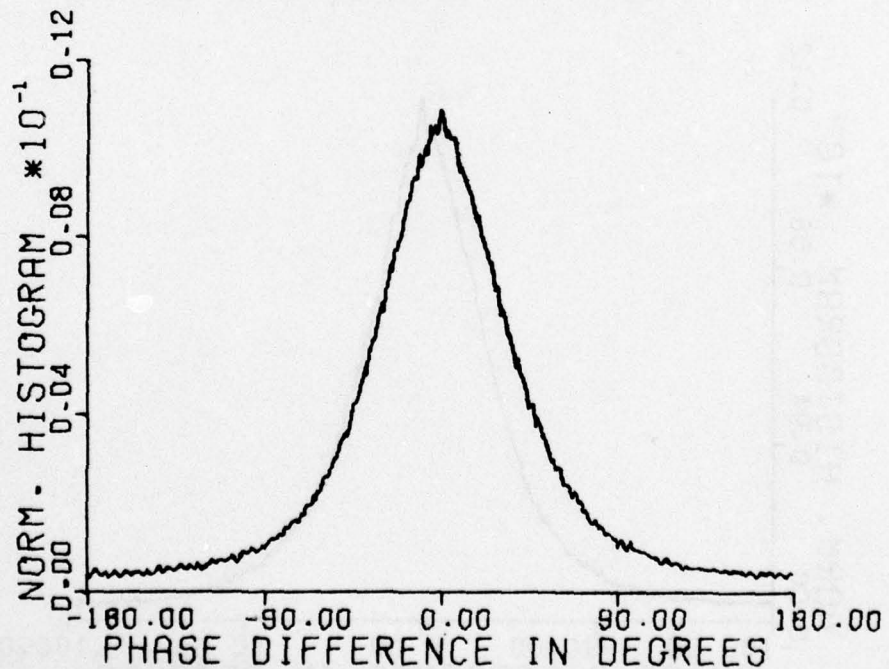


(b) histogram corresponding to Figure 5.1b

Figure 5.8 Phase difference histograms for case of Parzen windowing,
 $\Delta u=1$, $\Delta v=0$

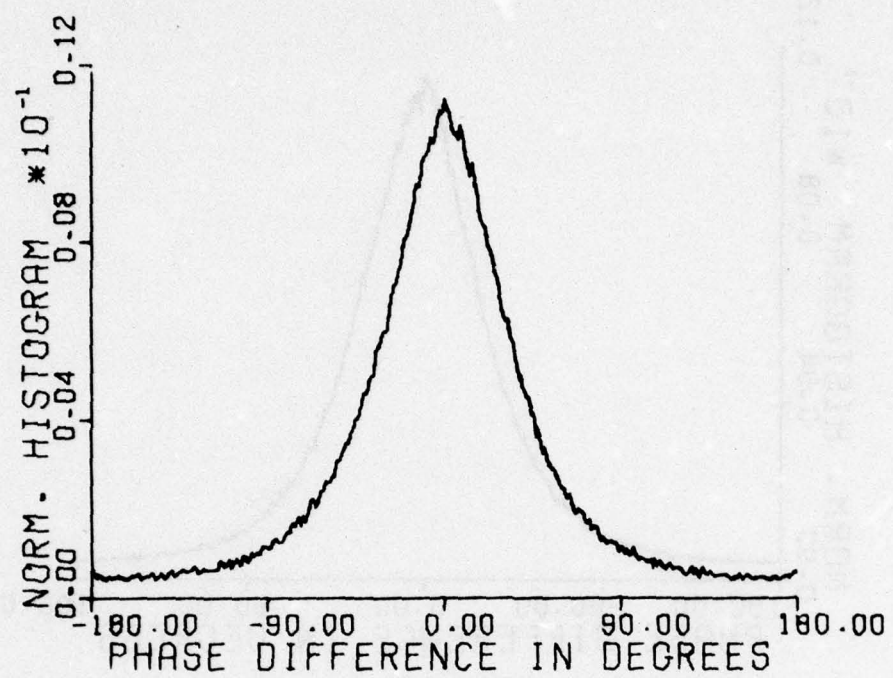


(c) histogram corresponding to Figure 5.1c

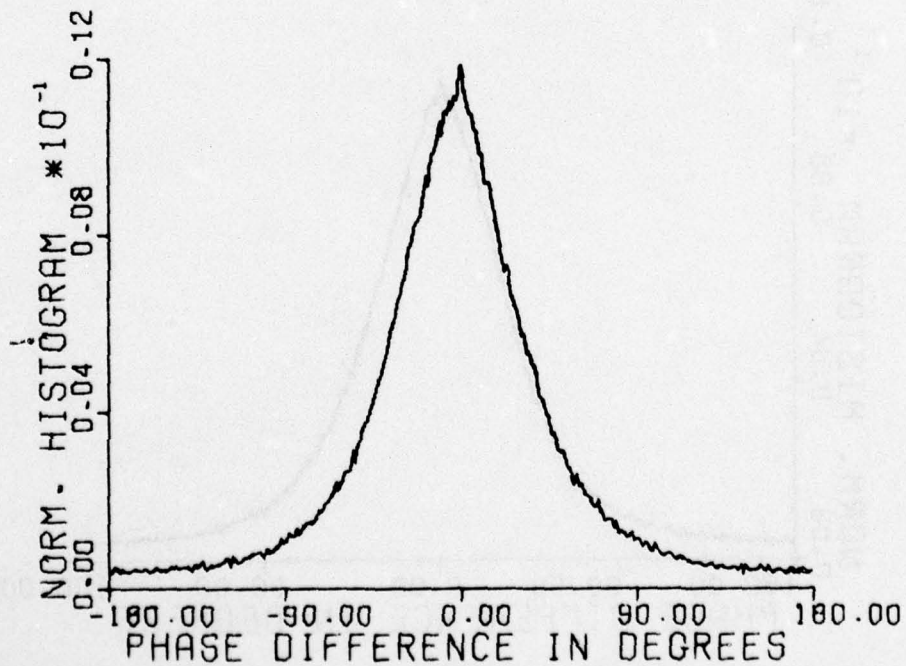


(d) histogram corresponding to Figure 5.1d

Figure 5.8 (Cont'd) Phase difference histograms for case of Parzen windowing, $\Delta u=1, \Delta v=0$

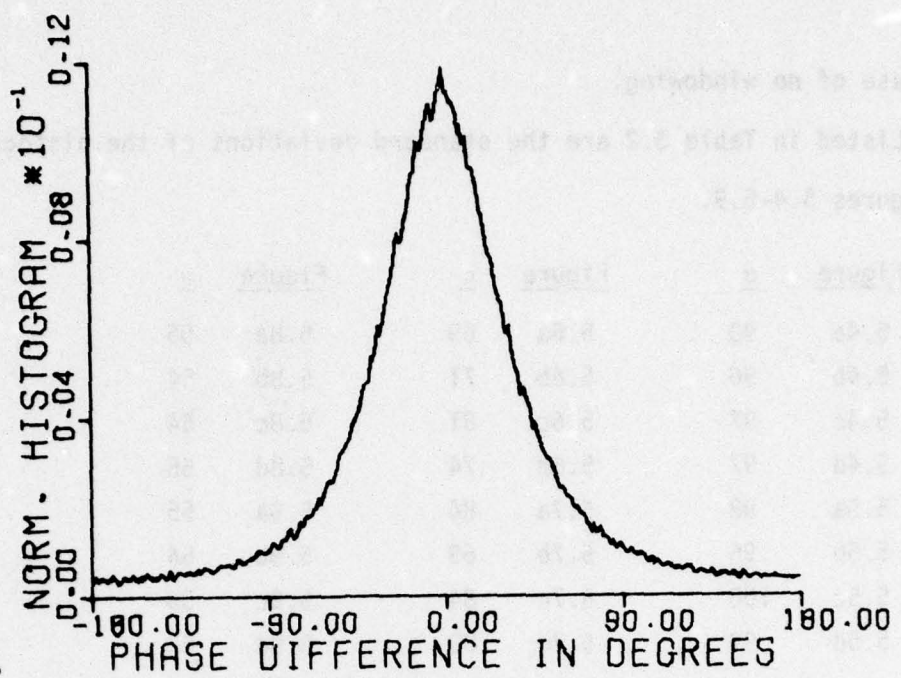


(a) histogram corresponding to Figure 5.1a

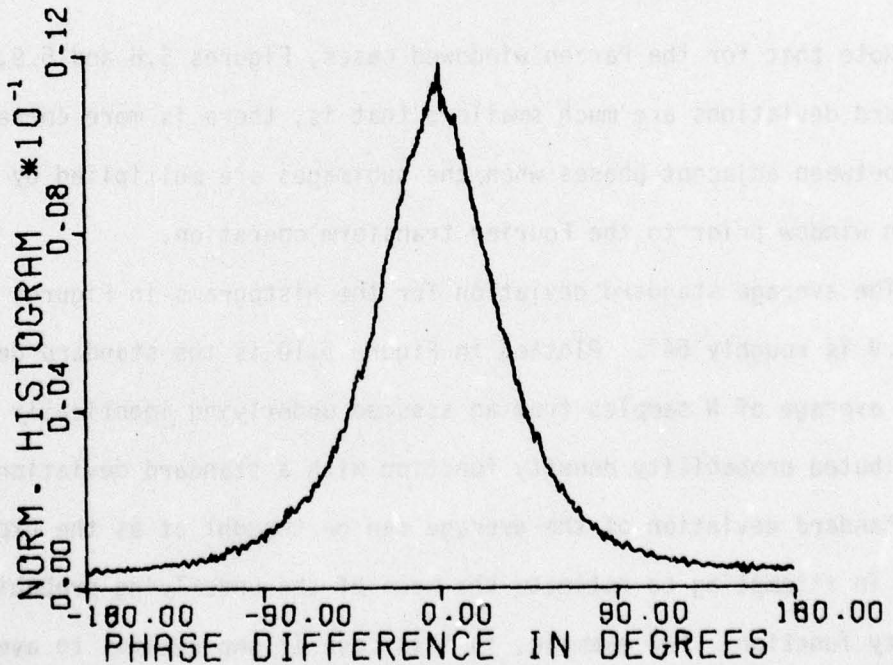


(b) histogram corresponding to Figure 5.1b

Figure 5.9 Phase difference histograms for case of Parzen windowing,
 $\Delta u=0, \Delta v=1$



(c) histogram corresponding to Figure 5.1c



(d) histogram corresponding to Figure 5.1d

Figure 5.9 (Cont'd) Phase difference histograms for case of Parzen windowing, $\Delta u=0, \Delta v=1$

the case of no windowing.

Listed in Table 5.2 are the standard deviations of the histograms in Figures 5.4-5.9.

<u>Figure</u>	<u>σ</u>	<u>Figure</u>	<u>σ</u>	<u>Figure</u>	<u>σ</u>
5.4a	93	5.6a	69	5.8a	55
5.4b	96	5.6b	71	5.8b	54
5.4c	97	5.6c	81	5.8c	54
5.4d	97	5.6d	74	5.8d	55
5.5a	98	5.7a	84	5.9a	55
5.5b	96	5.7b	69	5.9b	54
5.5c	100	5.7c	84	5.9c	53
5.5d	99	5.7d	80	5.9d	54

Table 5.2. Standard deviation in degrees of histograms in Figures 5.4 - 5.9

Note that for the Parzen windowed cases, Figures 5.8 and 5.9, the standard deviations are much smaller; that is, there is more correlation between adjacent phases when the subimages are multiplied by a Parzen window prior to the Fourier transform operation.

The average standard deviation for the histograms in Figures 5.8 and 5.9 is roughly 54° . Plotted in Figure 5.10 is the standard deviation of an average of N samples from an assumed underlying identically distributed probability density function with a standard deviation of 54° . The standard deviation of the average can be thought of as the expected error in attempting to estimate the mean of the underlying probability density function. For example, in this case if one desires to average the phase differences to the mean, and one uses $N = 225$ from Figure 5.10 on the average the estimate of the mean would be off by 3.5° .

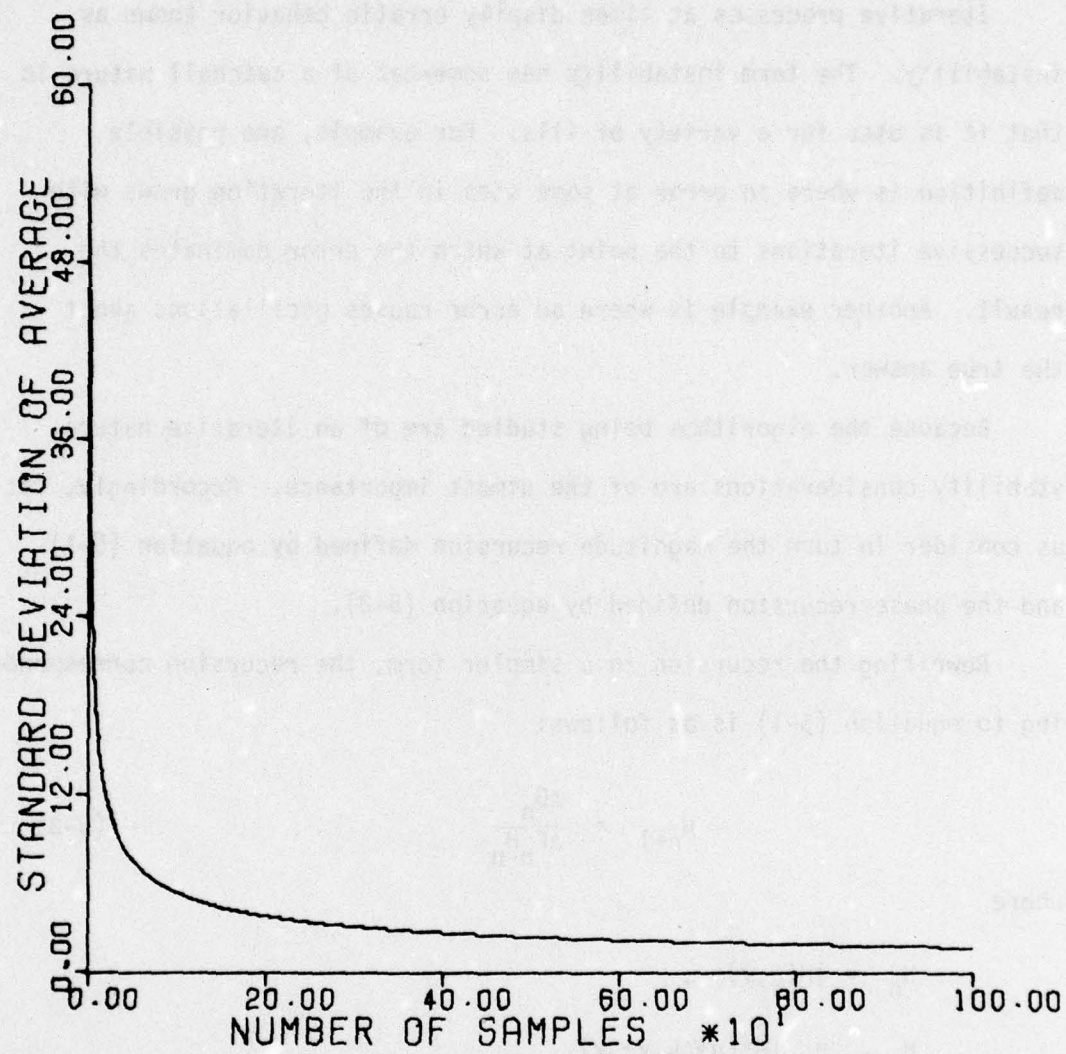


Figure 5.10 Standard deviation of the average vs number of samples for a sample standard deviation of 54°

5.4 On the Stability of the Iterations

Iterative processes at times display erratic behavior known as instability. The term instability has somewhat of a catchall nature in that it is used for a variety of ills. For example, one possible definition is where an error at some step in the iteration grows with successive iterations to the point at which the error dominates the result. Another example is where an error causes oscillations about the true answer.

Because the algorithms being studied are of an iterative nature, stability considerations are of the utmost importance. Accordingly, let us consider in turn the magnitude recursion defined by equation (5-1) and the phase recursion defined by equation (5-2).

Rewriting the recursion in a simpler form, the recursion corresponding to equation (5-1) is as follows:

$$H_{n+1} = \frac{\Delta G_n}{\Delta F_n H_n} \quad (5-3)$$

where

$$H_n = |H(u, v)| ,$$

$$H_{n+1} = |H^*(u + \Delta u, v + \Delta v)| ,$$

$$\Delta F_n = \frac{1}{N} \sum_{i=1}^N |F_i(u, v) F_i^*(u + \Delta u, v + \Delta v)| ,$$

and $\Delta G_n = \frac{1}{N} \sum_{i=1}^N |G_i(u, v) G_i^*(u + \Delta u, v + \Delta v)|$

$$- \frac{1}{N} \sum_{i=1}^N E_i^M(u, v, \Delta u, \Delta v) .$$

First let us consider the effects of roundoff error. Thus,

$$H_{n+1} = \frac{\Delta G_n}{\Delta F_n H_n} + E_n = \frac{\Delta G_n}{\Delta F_n H_n} (1 + \epsilon_n)$$

where

$$E_n = \frac{\Delta G_n}{\Delta F_n H_n} \epsilon_n.$$

Note

$$H_1 = \frac{\Delta G_0}{\Delta F_0 H_0} (1 + \epsilon_0)$$

$$H_2 = \frac{\Delta G_1}{\Delta F_1 H_1} (1 + \epsilon_1) = \frac{\Delta G_1}{\Delta F_1} \frac{\Delta F_0 H_0}{\Delta G_0} \frac{(1 + \epsilon_1)}{(1 + \epsilon_0)}$$

$$H_3 = \frac{\Delta G_2}{\Delta F_2 H_2} (1 + \epsilon_2) = \frac{\Delta G_2}{\Delta F_2} \frac{\Delta F_1}{\Delta G_1} \frac{\Delta G_0}{\Delta F_0 H_0} \frac{(1 + \epsilon_2)(1 + \epsilon_0)}{(1 + \epsilon_1)}$$

$$\vdots$$

$$H_{2n} = \frac{H_0 \prod_{k=1,3,\dots,2n-1}^{\infty} \Delta G_k \Delta F_{k-1} (1 + \epsilon_k)}{\prod_{k=0,2,4,\dots,2n-2}^{\infty} \Delta G_k \Delta F_{k+1} (1 + \epsilon_k)} \quad (5-4)$$

Intuitively, one may observe from equation (5-4) that the roundoff error will have a tendency to cancel out. More formally, taking expectation over the probability density function associated with the roundoff error and assuming the roundoff error at step n is uncorrelated with the roundoff error at step m , we have

$$\delta\{H_{2n}\} = \delta \left\{ \frac{H_0 \prod_{k=1,3,\dots,2n-1}^{\infty} \Delta G_k \Delta F_{k-1} (1 + \epsilon_k)}{\prod_{k=0,2,4,\dots,2n-2}^{\infty} \Delta G_k \Delta F_{k+1} (1 + \epsilon_k)} \right\}$$

$$\begin{aligned}
 \sigma \{H_{2n}\} &= \frac{H_0 \prod_{k \text{ odd}} \Delta G_k \Delta F_{k-1}}{\prod_{k \text{ even}} \Delta G_k \Delta F_{k+1}} \sigma \left\{ \frac{\prod_{k \text{ odd}} (1+\epsilon_k)}{\prod_{k \text{ even}} (1+\epsilon_k)} \right\} \\
 &= \frac{H_0 \prod_{k \text{ odd}} \Delta G_k \Delta F_{k-1}}{\prod_{k \text{ even}} \Delta G_k \Delta F_{k+1}} \prod_{k \text{ odd}} \sigma(1+\epsilon_k) \prod_{k \text{ even}} \sigma\left(\frac{1}{1+\epsilon_k}\right) \\
 &= \frac{H_0 \prod_{k \text{ odd}} \Delta G_k \Delta F_{k-1}}{\prod_{k \text{ even}} \Delta G_k \Delta F_{k+1}}
 \end{aligned}$$

since the mean of the roundoff error ϵ_k will be zero. Accordingly, at least with respect to roundoff error no instabilities are present.

To estimate a posteriori the magnitude of H one will not know ΔF_n in the above notation but must estimate ΔF_n by using a prototype image. Thus, instead of ΔF_n in equation (5-3) the iteration will be

$$H_{n+1} = \frac{\Delta G_n}{\Delta P_n H_n} = \frac{\Delta G_n}{(\Delta F_n + E_n) H_n} .$$

Let us now assume an error of 10% in approximating ΔF_0 by ΔP_0 , say +10%; assume no other errors and let us consider the propagation of this error on successive iterates.

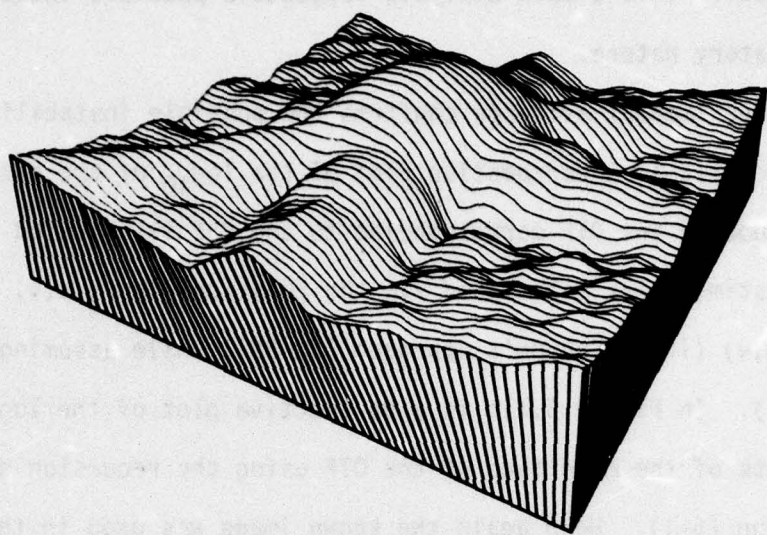
$$\begin{aligned}
 \hat{H}_1 &= \frac{\Delta G_0}{\Delta F_0 (1.1) H_0} = .91 \frac{\Delta G_0}{\Delta F_0 H_0} = .91 H_1 \\
 \hat{H}_2 &= \frac{\Delta G_1}{\Delta F_1 H_1} = \frac{\Delta G_1}{\Delta F_1 (.91 H_1)} = 1.1 H_2 \\
 \hat{H}_3 &= \frac{\Delta G_2}{\Delta F_2 H_2} = \frac{\Delta G_2}{\Delta F_2 (1.1) H_2} = .91 H_3
 \end{aligned}$$

Note the oscillation of the estimated magnitude about the true

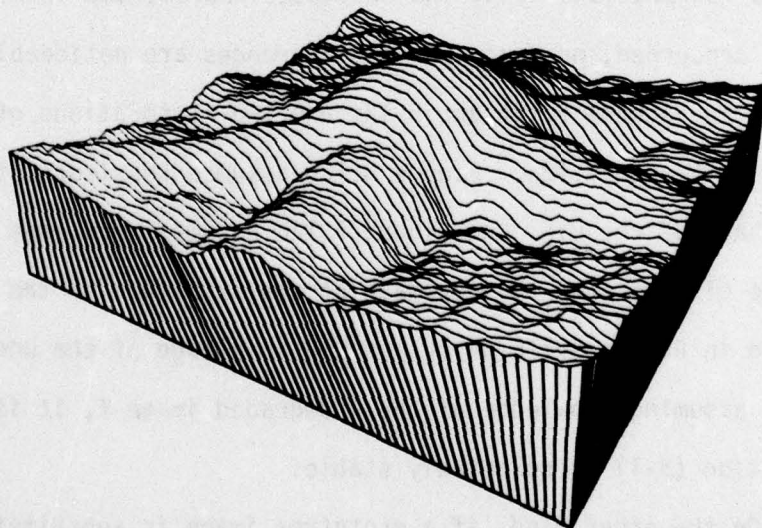
magnitude. This simple analysis suggests a possible instability of an oscillatory nature.

Experimental evidence confirms the possible instability. Shown in Figure 5.11a is a perspective plot of the \log_{10} of the estimate of the magnitude of the OTF corresponding to the PSF illustrated in Figure 4.4. This estimate was calculated via the relationship $\varphi_g(u,v) = |H(u,v)|^2 \cdot \varphi_f(u,v)$ (i.e., Cannon's approach [26-28]) while assuming knowledge of $\varphi_f(u,v)$. In Figure 5.11b is a perspective plot of the \log_{10} of an estimate of the magnitude of the OTF using the recursion defined in equation (5-1). Here again the known image was used in the calculations. That is, the quantities $\frac{1}{N} \sum_{i=1}^N |F_i(u,v)F_i^*(u+\Delta u, v+\Delta v)|$ were calculated from the known image. This estimate is not as smooth as the estimate illustrated in Figure 5.11a but is of roughly the same accuracy. As far as restorations using the estimates represented in Figures 5.11a and b are concerned, no perceivable differences are noticeable. For example, in Figures 5.12b and 5.12c are two restorations of the degraded image in Figure 5.12a. Figure 5.12b assumes knowledge of both magnitude and phase of the OTF, and Figure 5.12c assumes knowledge of the phase of the OTF and uses the estimate of the magnitude of the OTF represented in Figure 5.11b which assumed knowledge of the undegraded image. Thus, assuming knowledge of the undegraded image f , it is seen that the iteration (5-1) is relatively stable.

On the other hand, if a prototype image is substituted for the unknown image, the magnitude iteration cannot cope with the errors inherent in the substitution. In Figure 5.13a is an estimate of the magnitude of the OTF corresponding to the PSF illustrated in Figure 4.4.



(a) estimate via method of Cannon



(b) recursive estimate

Figure 5.11 Comparison of magnitude estimates using knowledge of the undegraded image

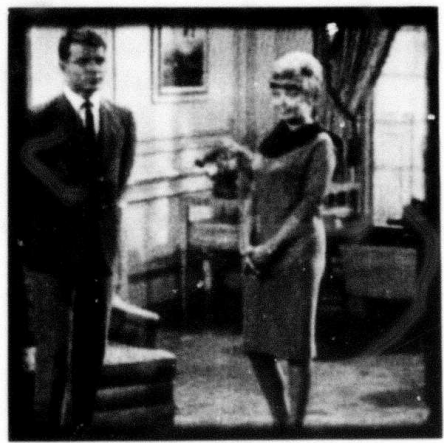
**Best
Available
Copy**



(a) degraded image

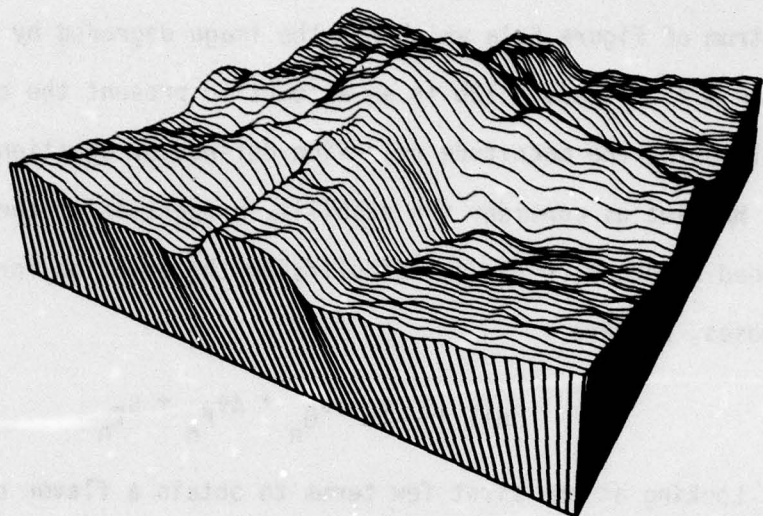


(b) restoration given both magnitude and phase of the OTF

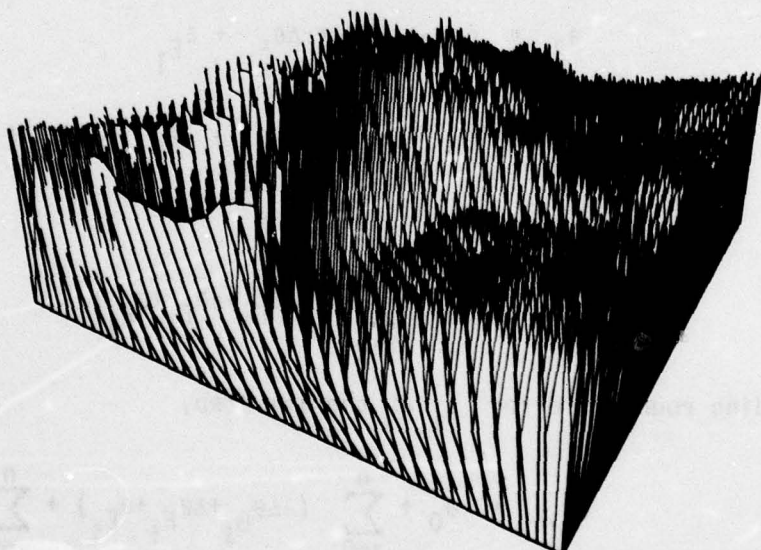


(c) restoration given phase of the OTF and using the magnitude estimate of Figure 5.11b

Figure 5.12 Restorations



(a) estimate via the method of Cannon



(b) recursive estimate

Figure 5.13 Comparison of magnitude estimates without knowledge of the undegraded image

This estimate used the method of Cannon and the average power spectrum calculated from Figures 5.1b, c and d as an estimate of the power spectrum of Figure 5.1a which was the image degraded by the PSF in Figure 4.4. Figure 5.13b is an attempt to present the corresponding result using the magnitude recursion defined by equation (5-1).

Now let us consider the stability properties of the phase iteration defined by equation (5-2). Simplifying the equation for illustrative purposes, we have

$$\theta_{n+1} = \theta_n - \Delta\theta_{G_n} + \Delta\theta_{F_n} + \theta_{E_n}$$

Looking at the first few terms to obtain a flavor of the propagation of the results, we have

$$\begin{aligned} \theta_1 &= \theta_0 - \Delta\theta_{G_0} + \Delta\theta_{F_0} + \theta_{E_0} \\ \theta_2 &= \theta_1 - \Delta\theta_{G_1} + \Delta\theta_{F_1} + \theta_{E_1} \\ &= \theta_0 - \Delta\theta_{G_0} - \Delta\theta_{G_1} + \Delta\theta_{F_0} + \Delta\theta_{F_1} + \theta_{E_0} + \theta_{E_1} \\ &\vdots \\ \theta_{n+1} &= \theta_0 + \sum_{i=0}^n (-\Delta\theta_{G_i} + \Delta\theta_{F_i} + \theta_{E_i}) \end{aligned} \quad (5-5)$$

Adding roundoff error ϵ_i at the $i+1$ step,

$$\theta_{n+1} = \theta_0 + \sum_{i=0}^n (-\Delta\theta_{G_i} + \Delta\theta_{F_i} + \theta_{E_i}) + \sum_{i=0}^n \epsilon_i$$

Taking mathematical expectation over the randomness inherent in the roundoff errors,

$$\begin{aligned}
 \delta \theta_{n+1} &= \theta_0 + \sum_{i=0}^n (-\Delta \theta_{G_i} + \Delta \theta_{F_i} + \theta_{E_i}) + \delta \sum_{i=0}^n \epsilon_i \\
 &= \theta_0 + \sum_{i=0}^n (-\Delta \theta_{G_i} + \Delta \theta_{F_i} + \theta_{E_i}) + \sum_{i=0}^n \delta \epsilon_i \\
 &= \theta_{n+1}
 \end{aligned}$$

since the roundoff error will be zero mean. Thus, roundoff errors will not induce any instabilities in the phase iteration.

In addition from equation (5-5) it is seen that errors will be additive. As a result, the iteration itself will be stable.

5.5 On Errors of Approximation

Let us first consider the errors involved in approximating a continuous process by a discrete process. Although the functions in the model of the blurring process are best considered as continuous functions, the digital computer is discrete and at some point the processes must be discretized to be compatible with digital processing. Attempting to estimate continuous functions from sampled versions is not something to be taken for granted.

Because a continuous function has been sampled at discrete points to form the digital image, errors due to the sampling may be introduced. For example, if the sampling rate is too low, high frequency components in the Fourier domain will impersonate low frequency components. This situation is referred to as aliasing. In addition to aliasing one must be aware of the problem referred to as leakage. Due to the necessity of considering finite subimages, frequency components corresponding to these finite subimages will be spread over or leaked to adjacent

frequency components.

When one extracts a subimage from an image and desires the continuous Fourier transform (CFT) as an economic necessity, what does one in general settle for? In general one settles for the discrete Fourier transform (DFT) as an approximation to the CFT. The DFT is defined in equation (5-6) below.

$$F(K,L) = \frac{1}{N^2} \sum_{I=0}^{N-1} \sum_{J=0}^{N-1} f(I,J) e^{-j2\pi(IK+JL)/N} \quad (5-6)$$

where $I, J, K, L = 0, 1, \dots, N-1$.

The DFT is calculated via the fast Fourier transform (FFT) which is an efficient algorithm for such calculations.

The DFT can be shown to be an approximation to the CFT. If one begins with the definition of the CFT, truncates the limits of integration to $(-\frac{T}{2}, \frac{T}{2})$, samples the integrand at equally spaced points, applies the trapezoidal rule [48] to numerically integrate, and ignores the linear phase factor due to shifting the lower limit of $-\frac{T}{2}$ on the integral to a lower limit of 0 on the summation, one obtains the DFT.

Considering the one dimensional case for simplicity, at the frequency $K = N-1$ it can be shown that the $e^{-j2\pi ux}$ factor in the integrand of the definition of CFT is sampled at two points per cycle where cycle refers to the periodic nature of $e^{-j2\pi ux}$, i.e., $e^{-j2\pi ux} = \cos 2\pi ux - j \sin 2\pi ux$. Thus, at the frequency $K = N-1$ the function to be transformed is multiplied by a function which is changing rapidly relative to the sampling. Thus, it is not hard to see that in using the FFT to approximate continuous Fourier transforms a degree of error

is introduced.

Both $f(I,J)$ and $F(K,L)$ are now assumed to be periodic, and as a consequence of the periodicity, typically the function $f(I,J)$, now considered as a periodic function, contains jump discontinuities at the ends of the periods. The jump discontinuities induce spurious high frequency components in the Fourier domain. To alleviate this situation the function $f(I,J)$ is multiplied by a function $w(I,J)$, called a window, which smoothes to zero the ends of the periodic function, thus eliminating the jump discontinuities and the associated sharp edges. As a consequence of the fact that multiplication in the picture domain corresponds to convolution in the frequency domain, we would have in the frequency domain upon multiplying $f(I,J)$ by $w(I,J)$

$$F(K,L) * W(K,L)$$

where $*$ denotes convolution.

At this point it is appropriate to consider the choice of the window $w(I,J)$ for the problem at hand. Ultimately, an estimate of $H(u,v)$ is desired. Since the blurred image is assumed to be a convolution across the entire image, we have only the approximate relationship

$$g_I(x,y) \approx h(x,y) * f_I(x,y) . \quad (5-7)$$

Referring to the width of $h(x,y)$ as the portion of the independent variables corresponding to nonzero $h(x,y)$, then for points of $g_I(x,y)$ within a half width of $h(x,y)$ from the boundary of $g_I(x,y)$, approximation (5-7) is exact. For points of $g_I(x,y)$ outside a half width of $h(x,y)$ from the boundary the relationship is erroneous. Note by

equation (1-2) approximation (5-7) assumes by definition an aperiodic convolution. On the other hand, in the discretized domain in which by necessity we must do our calculations, we have the pair

$$\text{and } g(I,J) = h(I,J) \circledast f(I,J)$$
$$G(K,L) = H(K,L)F(K,L)$$

where \circledast denotes a circular or periodic convolution. Here $h(I,J)$ and $f(I,J)$ are assumed to be periodic, and as a result, the circular convolution can be used as an approximation to the aperiodic convolution only with caution.

The relationship between the aperiodic and circular convolution is again for points of $g_i(x,y)$ within a half width of $h(x,y)$ from the boundary, the two are the same. For points of $g_i(x,y)$ outside a half width of $h(x,y)$ from the boundary, the difference between the aperiodic and circular convolution can be substantial.

The differences between the aperiodic and circular convolution are not only relevant as an approximation which induces error into the calculations but additionally because the errors in approximation (5-7) occur at the same points as the errors induced by replacing the aperiodic convolution with the circular convolution.

With this in mind let us consider several candidate windows, including the case of no window, and compare the error in the Fourier domain for functions convolved aperiodically and windowed by a candidate window and also convolved circularly and windowed by the same candidate window.

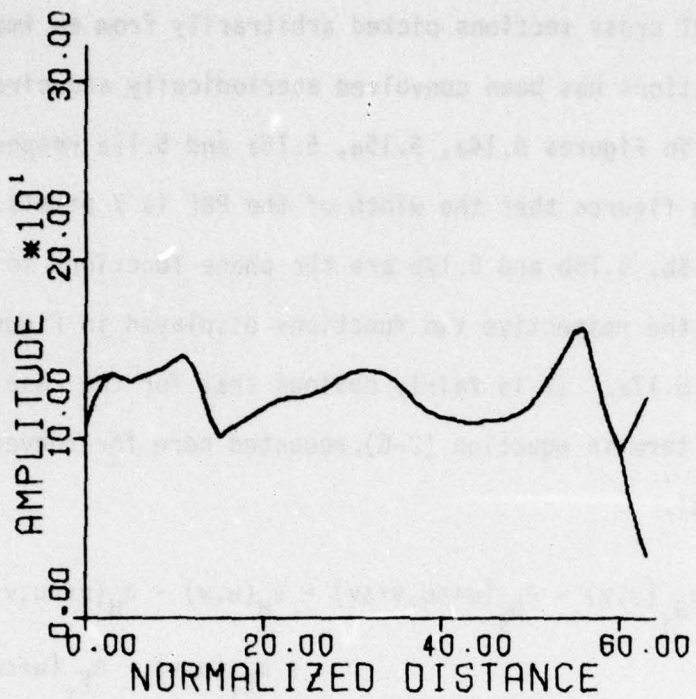
First let us consider the case of no windowing on several one

dimensional cross sections picked arbitrarily from an image. Each of these functions has been convolved aperiodically and circularly and displayed in Figures 5.14a, 5.15a, 5.16a and 5.17a respectively. Note from these figures that the width of the PSF is 7 pixels. In Figures 5.14b, 5.15b, 5.16b and 5.17b are the phase functions in the Fourier domain of the respective two functions displayed in Figures 5.14a, 5.15a, 5.16a and 5.17a. It is fairly obvious that for the case of no windowing the error term in equation (2-6), repeated here for convenience, can be substantial.

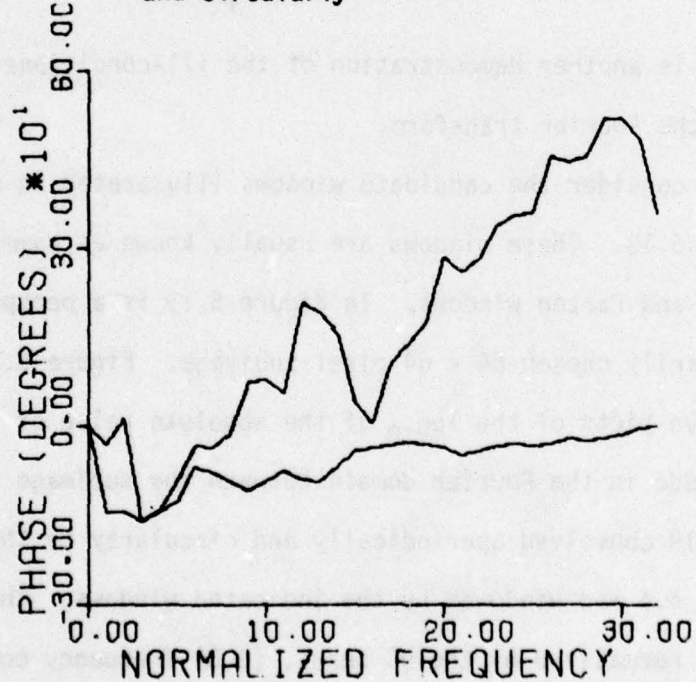
$$\begin{aligned}\theta_{G_i}(u, v) - \theta_{G_i}(u + \Delta u, v + \Delta v) &= \theta_H(u, v) - \theta_H(u + \Delta u, v + \Delta v) \\ &\quad + \theta_{F_i}(u, v) - \theta_{F_i}(u + \Delta u, v + \Delta v) \\ &\quad + \theta_{E_i}(u, v, \Delta u, \Delta v)\end{aligned}$$

This is another demonstration of the ill-conditioned nature of the phase of the Fourier transform.

Next consider the candidate windows illustrated in one dimension in Figure 5.18. These windows are usually known as Hamming, Hanning, triangle, and Parzen windows. In Figure 5.19 is a perspective plot of an arbitrarily chosen 64×64 pixel subimage. Figure 5.20 contains perspective plots of the \log_{10} of the absolute value of the difference in magnitude in the Fourier domain between the subimage illustrated in Figure 5.19 convolved aperiodically and circularly by the PSF displayed in Figure 4.4 and windowed by the indicated windows. The differences have been normalized by the DC terms, $(0,0)$ frequency component, of the aperiodically convolved result. Note that for all four windows the

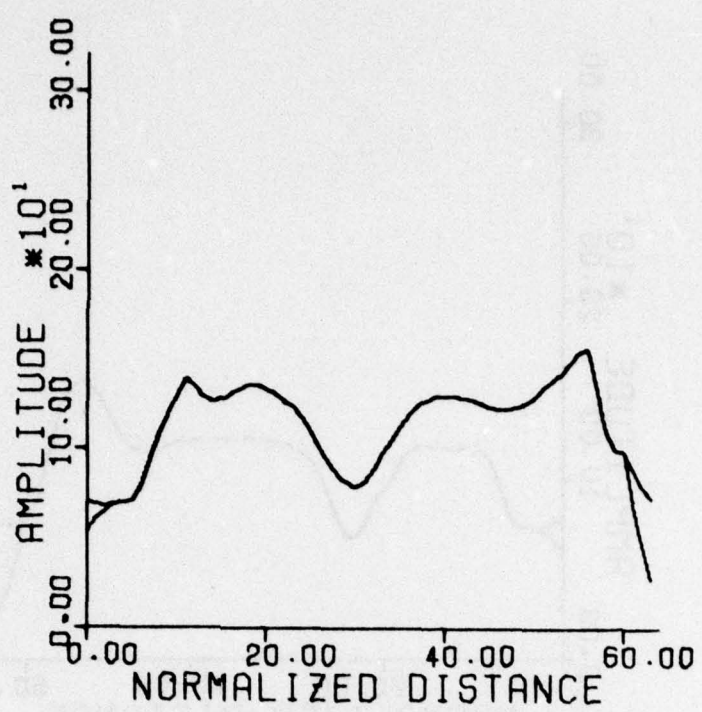


(a) a function convolved aperiodically and circularly

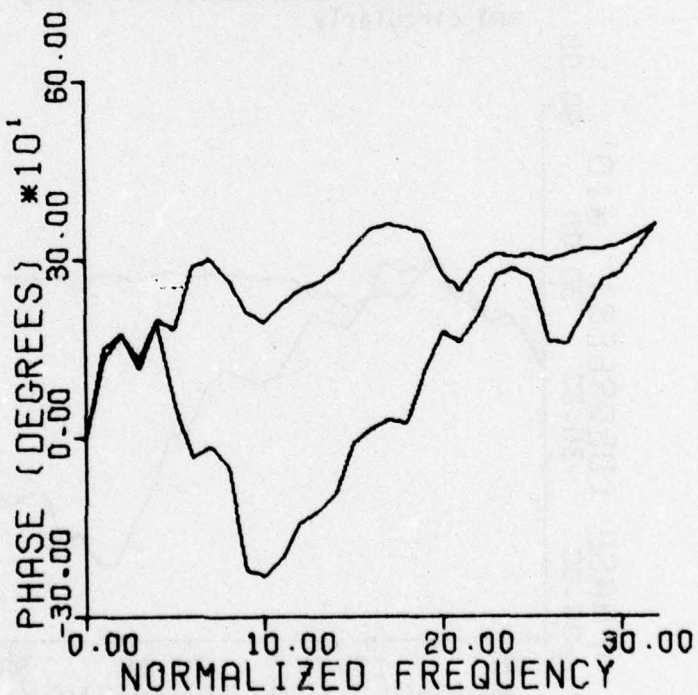


(b) corresponding phases

Figure 5.14 Phases corresponding to a function convolved aperiodically and circularly

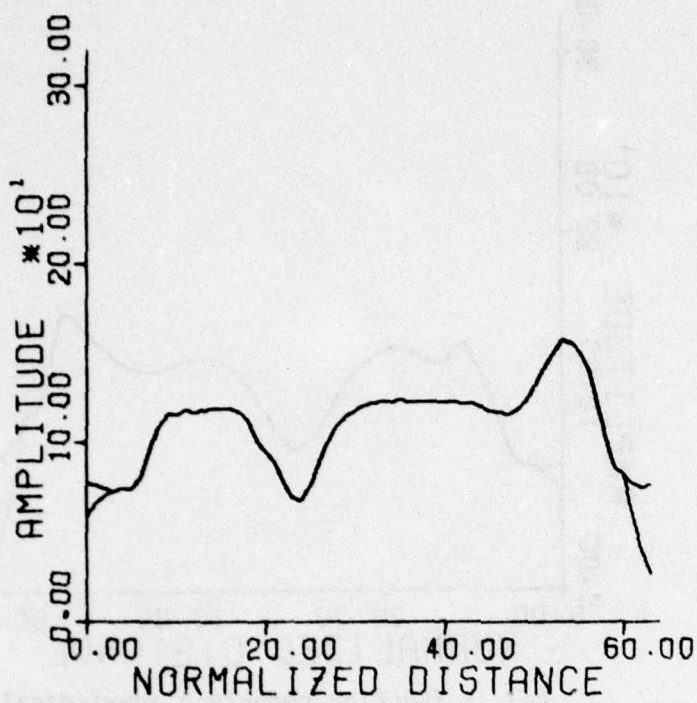


(a) a function convolved aperiodically
and circularly

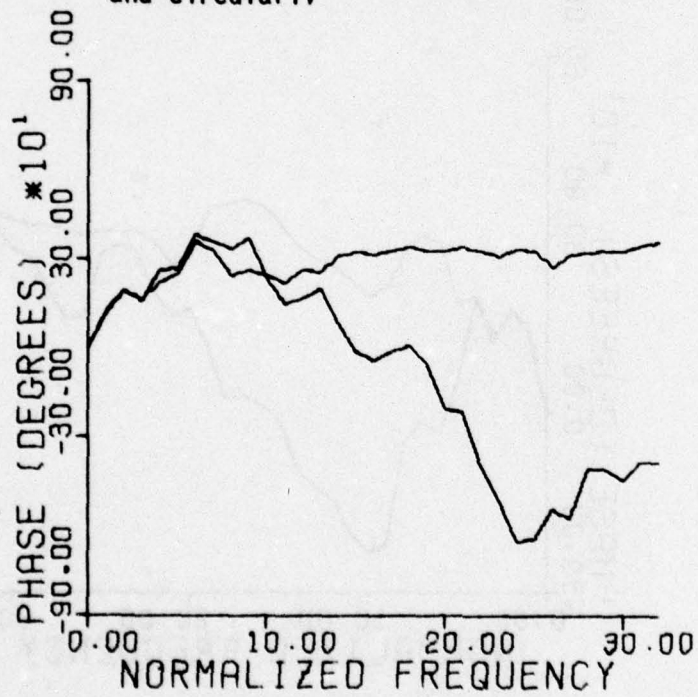


(b) corresponding phases

Figure 5.15 Phases corresponding to a function convolved aperiodically
and circularly

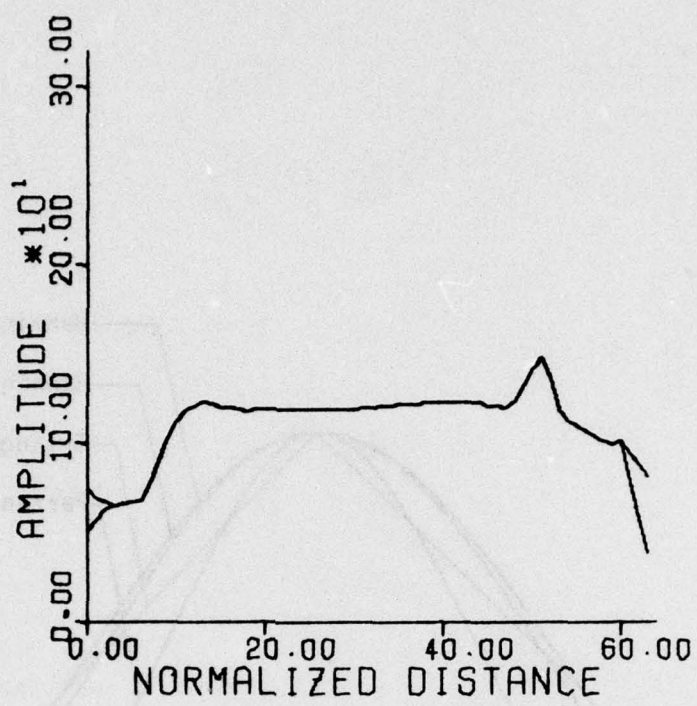


(a) a function convolved aperiodically and circularly

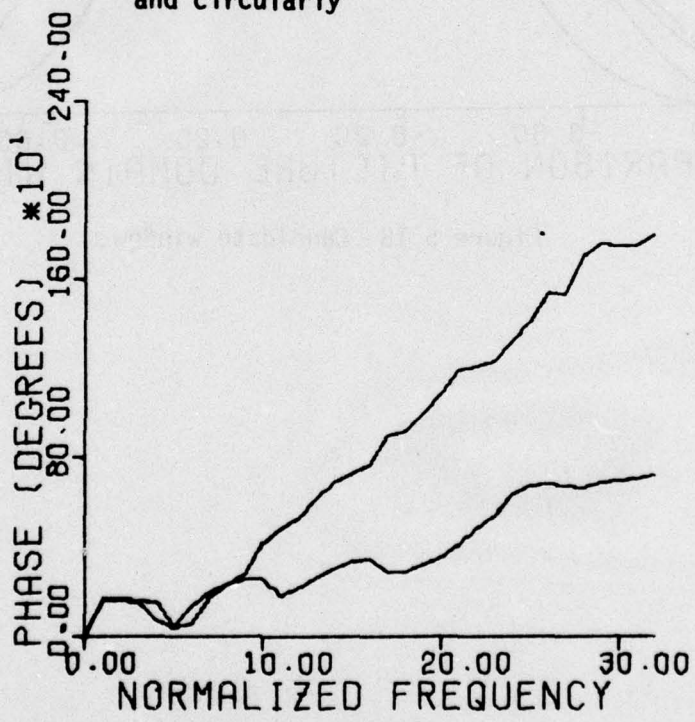


(b) corresponding phases

Figure 5.16 Phases corresponding to a function convolved aperiodically and circularly



(a) a function convolved aperiodically and circularly



(b) corresponding phases

Figure 5.17 Phases corresponding to a function convolved aperiodically and circularly

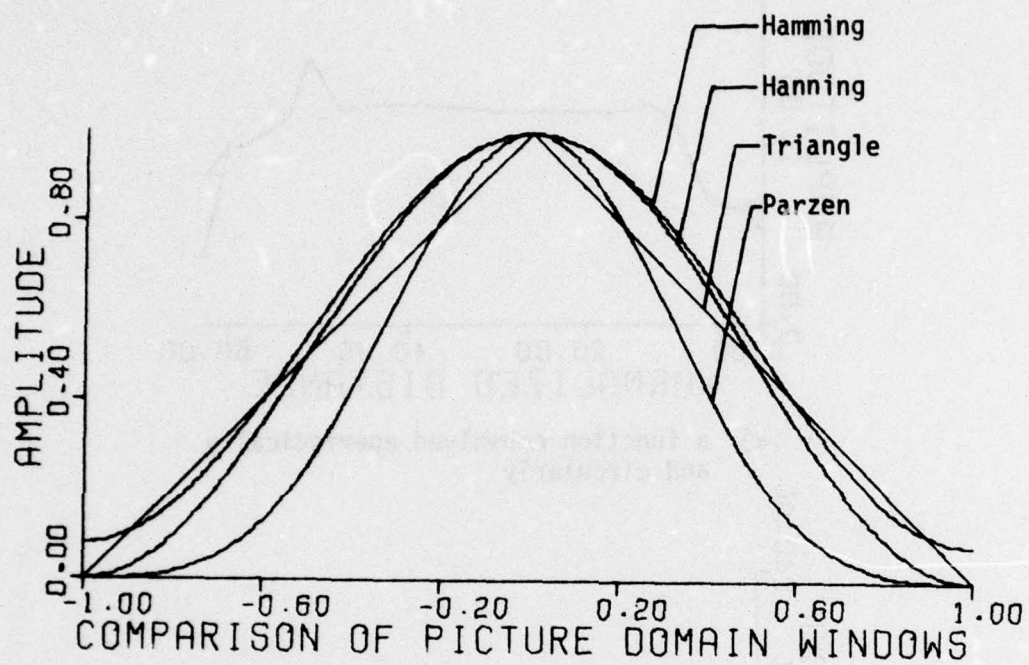


Figure 5.18 Candidate windows

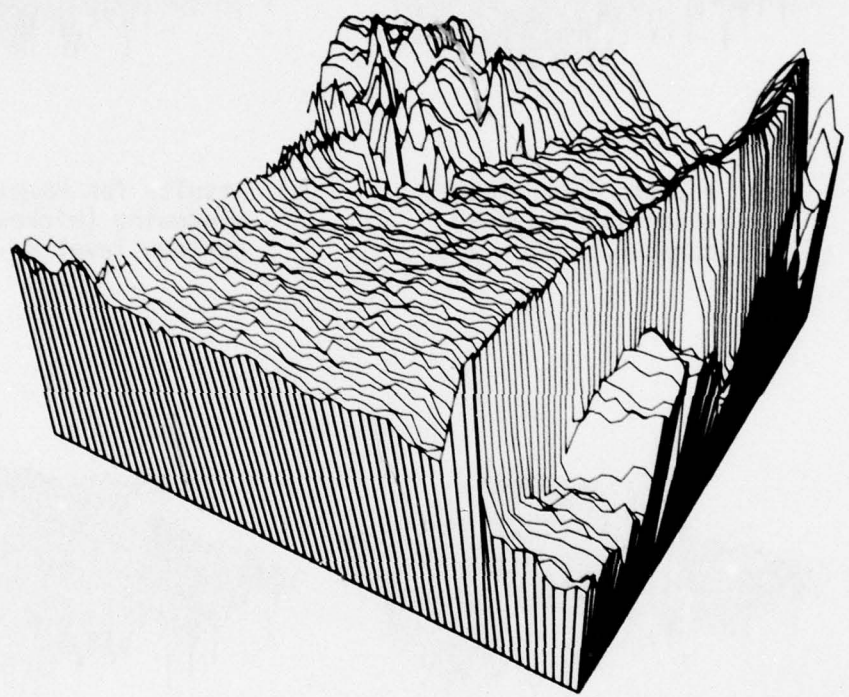
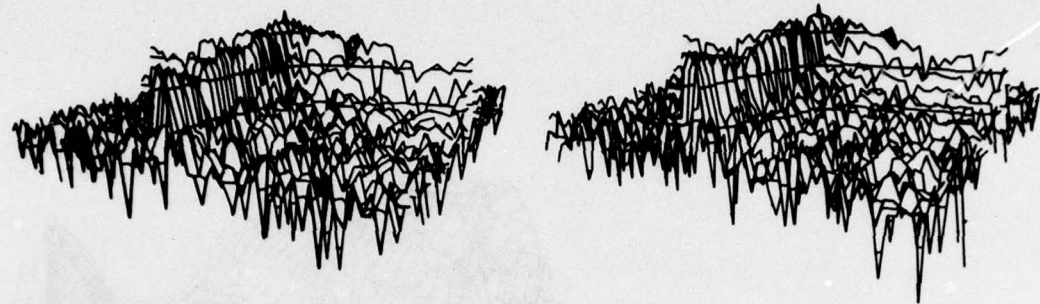
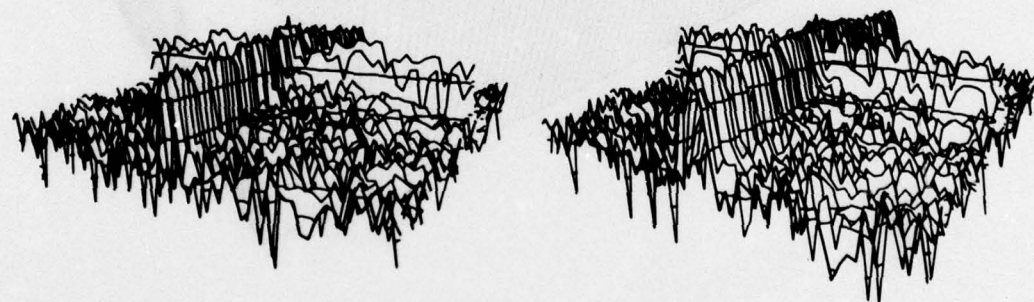


Figure 5.19 Arbitrarily chosen subimage used in windowing study



(a) results for triangle windowing (highest contour level = -3)

(b) results for Hamming windowing (highest contour level = -3)



(c) results for Hanning windowing (highest contour level = -4)

(d) results for Parzen windowing (highest contour level = -5)

Figure 5.20 Magnitude differences of Fourier transforms of subimage convolved aperiodically and circularly for different windows (difference in contour levels = 1)

differences are comparable and suggest that the approximation (used by both Cole [25] and Cannon [26-28])

$$|G_i(u,v)| \approx |H(u,v)| |F_i(u,v)|$$

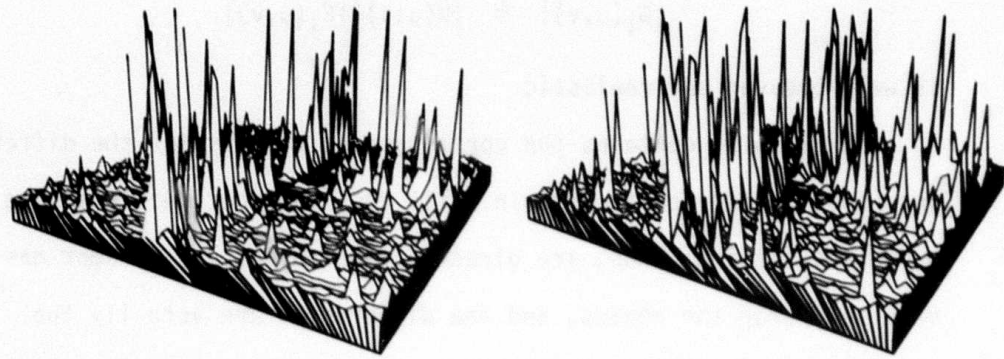
is well behaved and realistic.

Figure 5.21 contains the corresponding results for the differences in phases in the Fourier domain. All four perspective plots have the same plot scaling; thus, are directly comparable. No attempt has been made to unwrap the phases, and the differences are actually the absolute value of the principal value of the difference in principal values of the two sets of phases for a given windowing. Accordingly, the maximum error will be 180° . Although the phases have not been unwrapped, the point to be made, however, is clear. Because the phases in the Fourier domain are susceptible to large changes from small changes in the picture domain, i.e., ill-conditioning, the approximation

$$\theta_{G_i}(u,v) \approx \theta_H(u,v) + \theta_{F_i}(u,v) \quad (5-8)$$

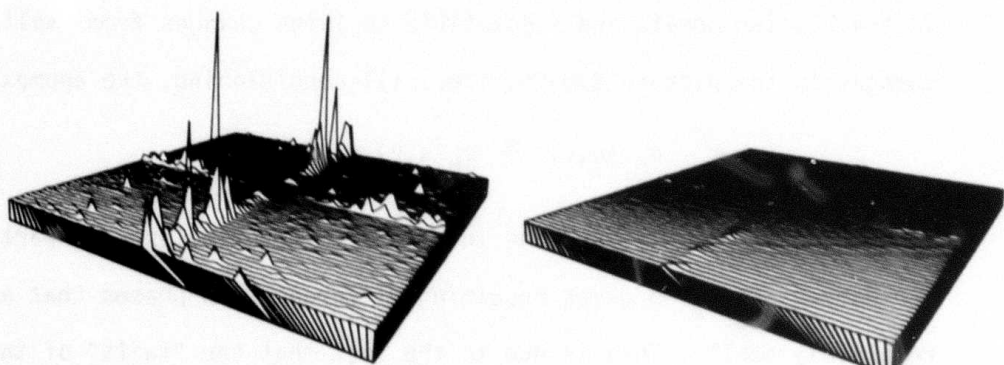
is not a particularly good one in general. Nevertheless, in particular the Parzen windowing gives resulting differences in phases that are relatively small. This is due to the fact that the "tails" of the Parzen window are essentially zero over the region in which the aperiodically convolved result and circularly convolved result differ. Thus, the Parzen windowing in effect throws away the values in the picture domain that differ as a result of the differences between the aperiodic and circular convolution.

Since approximation (5-8) is a crucial assumption leading to the



(a) results for triangle windowing

(b) results for Hamming windowing



(c) results for Hanning windowing

(d) results for Parzen windowing

Figure 5.21 Phase differences of Fourier transforms of subimage convolved aperiodically and circularly for different windowing.

recursive estimate of phase, that is, equation (5-2), and because the approximation is not a particularly sharp approximation, the technique must be reformulated to take advantage of the advantageous properties of the Parzen windowing. Accordingly, including the effects of the window, we now have

$$G(u,v)*W(u,v) = [H(u,v)F(u,v)]*W(u,v)$$

where W refers to the Fourier transform of the window. For a subimage we have approximately

$$G_i(u,v)*W(u,v) \approx [H(u,v)F_i(u,v)]*W(u,v) \quad (5-9)$$

and the further approximation

$$G_i(u,v)*W(u,v) \approx H(u,v)[F_i(u,v)*W(u,v)] \quad (5-10)$$

can be made. This approximation can be reasoned on the idea that $H(u,v)$ is essentially constant across the extent of the spectral window $W(u,v)$ and therefore can be factored outside the integral implicit in the convolution operator. If one is concerned with magnitudes at this point, then

$$|G_i(u,v)*W(u,v)| \approx |H(u,v)||F_i(u,v)*W(u,v)|. \quad (5-11)$$

Experimental evidence confirms the appropriateness of approximation (5-11), and as judged by the results of both Cole [25] and Cannon [26-28] who used this approximation in their work, the approximation is indeed realistic. As a result, the recursive estimate of OTF magnitude with the inclusion of the window is not substantially different than equation (5-1). For completeness the analogous recursion is included as defined by equation (5-12) below.

$$\frac{|\mathcal{H}^*(u+\Delta u, v+\Delta v)| = \left\{ \frac{1}{N} \sum_{i=1}^N |[G_i(u, v)*W(u, v)][G_i^*(u+\Delta u, v+\Delta v)*W(u+\Delta u, v+\Delta v)]| - \frac{1}{N} \sum_{i=1}^N E_i^M(u, v, \Delta u, \Delta v) \right\}}{|\mathcal{H}(u, v)| \frac{1}{N} \sum_{i=1}^N |[F_i(u, v)*W(u, v)][F_i^*(u+\Delta u, v+\Delta v)*W(u+\Delta u, v+\Delta v)]|} \quad (5-12)$$

where the error term $E_i^M(u, v, \Delta u, \Delta v)$ is denoted by the same notation as in equation (5-1) but is in general different.

Let us now include the effects of the window in the formulation of the phase estimate. Analogous to approximation (5-11) we have

$$\theta_{G_i*W}(u, v) \approx \theta_{\mathcal{H}}(u, v) + \theta_{F_i*W}(u, v)$$

where $\theta_{G_i*W}(u, v)$ denotes the phase of $G_i(u, v)*W(u, v)$ and $\theta_{F_i*W}(u, v)$ denotes the phase of $F_i(u, v)*W(u, v)$. This approximation leads to the phase recursion (5-13).

$$\begin{aligned}
 \theta_{\mathcal{H}}(u+\Delta u, v+\Delta v) = & \theta_{\mathcal{H}}(u, v) - [\overline{\theta_{G_i*W}(u, v)} - \overline{\theta_{G_i*W}(u+\Delta u, v+\Delta v)}] \\
 & + [\overline{\theta_{F_i*W}(u, v)} - \overline{\theta_{F_i*W}(u+\Delta u, v+\Delta v)}] + E(u, v, \Delta u, \Delta v)
 \end{aligned} \quad (5-13)$$

where E denotes the error inherent in the assumed approximations.

The operation of convolution in the transform domain results in a smearing or blurring of the Fourier coefficients. One might ask to what extent can one utilize the phase differences of the smeared quantities, i.e., $\theta_{G_i*W}(u, v)$ and $\theta_{F_i*W}(u, v)$, in estimating the phase differences of the OTF. To answer this question the following simulation was performed.

A 512 x 512 pixel image was subdivided into 225 64 x 64 pixel subimages where a 50% overlapping of subimages was allowed. Each of the 225 subimages were Fourier transformed and the Fourier coefficients on or within two fundamental frequencies of the axis were saved on tape for later processing.

In the simulation the saved coefficients correspond to $F_i(I, J)$ where I and J are associated with those indices on or within two steps of the frequency axes. At this point one can assume a given OTF, $H(I, J)$, multiply the given OTF times each $F_i(I, J)$ and obtain

$$G_i(I, J) = H(I, J)F_i(I, J) . \quad (5-14)$$

Note that by definition relationship (5-14) will be exact, and computer implementation of the multiplication will preserve the equality to within the roundoff error of the machine. Thus, using quantities calculated via equation (5-14), one can study the effects of various windows by the calculation of

$$G_i(I, J)*W(I, J) .$$

The simulation assumed that the Fourier coefficients along the u -axis and the Fourier coefficients along the v -axis had the same underlying probability density functions, and thus were lumped together. Accordingly, the results will be considered to be along an axis. For definiteness assume the I axis.

Letting the phase of H be linear and one dimensional,

$$\theta_H(I, J) = aI, \quad (5-15)$$

one can calculate

$$\overline{\theta_{G_i*W}(I,0) - \theta_{G_i*W}(I+1,0)}. \quad (5-16)$$

In the ideal case one would desire the average at each frequency I in (5-16) to be

$$aI - a(I+1) = -a.$$

Even if the ideal was not found, but if to each "a," the average (5-16) converged to a unique "b," then given a "b" the correct phase difference of the OTF could be found. That is, if

$$b(I) = f(a(I))$$

where f denotes a function and assuming to each $a(I)$ corresponds a unique $b(I)$, then

$$a(I) = f^{-1}(b(I))$$

where f^{-1} denotes the inverse mapping.

Shown in Figures 5.22 and 5.23 are the results of the simulation for the case of no windowing. The subimages used in the simulation corresponding to Figure 5.22 were taken from the image shown in Figure 5.1a; the subimages used in the simulation corresponding to Figure 5.23 were taken from the image shown in Figure 5.1b. In this simulation $\theta_H(I,J)$ assumed nine different linear functions. The first function was $\theta_{H_1}(I,J) = 0$. The second function was linear such that

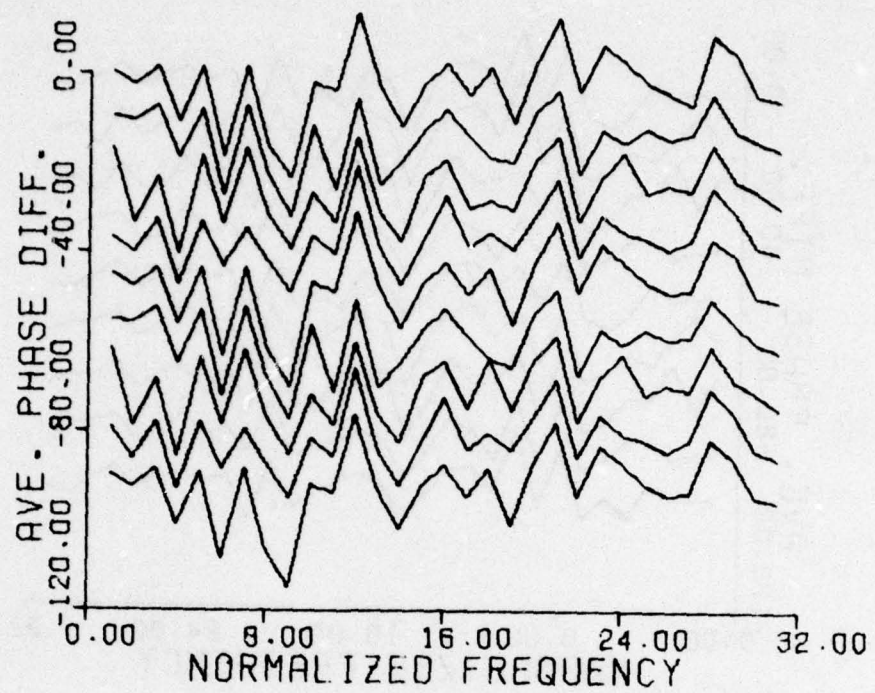
$$\theta_{H_2}(I,J) - \theta_{H_2}(I+1,J) = -11.25^\circ$$

The third function was linear such that

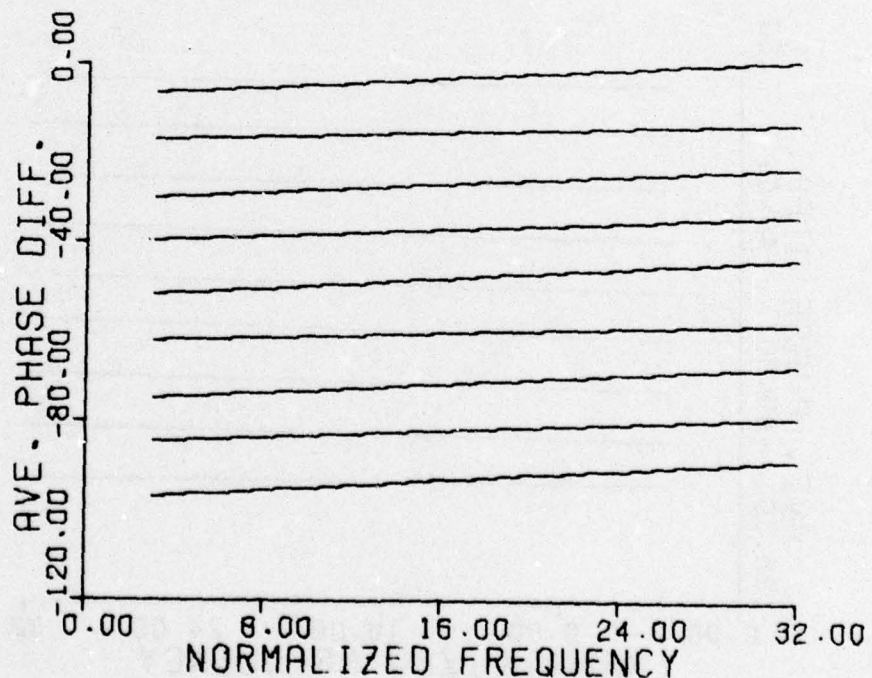
$$\theta_{H_3}(I,J) - \theta_{H_3}(I+1,J) = -22.50^\circ$$

⋮

and so on

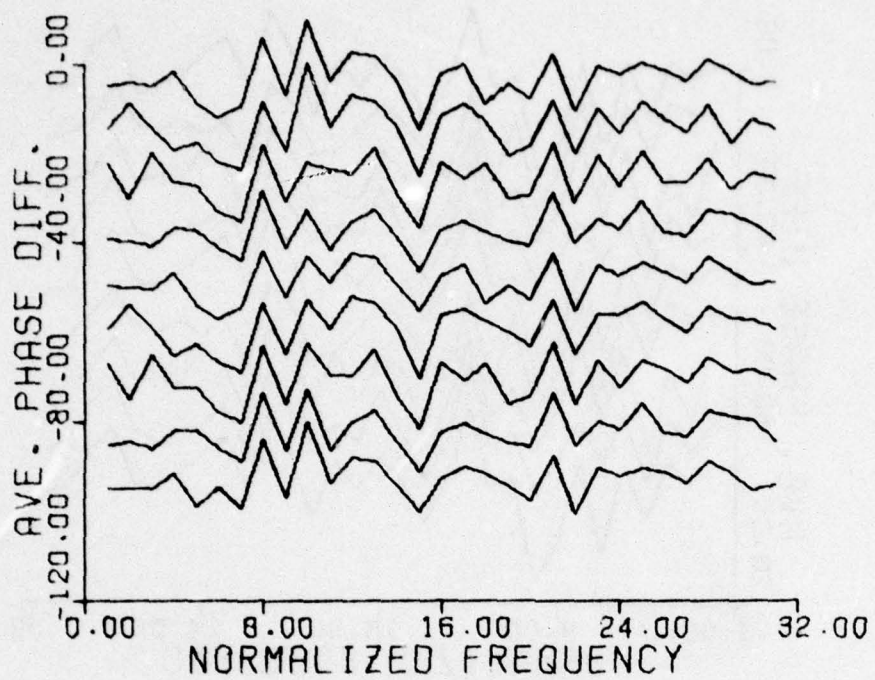


(a) phase averages

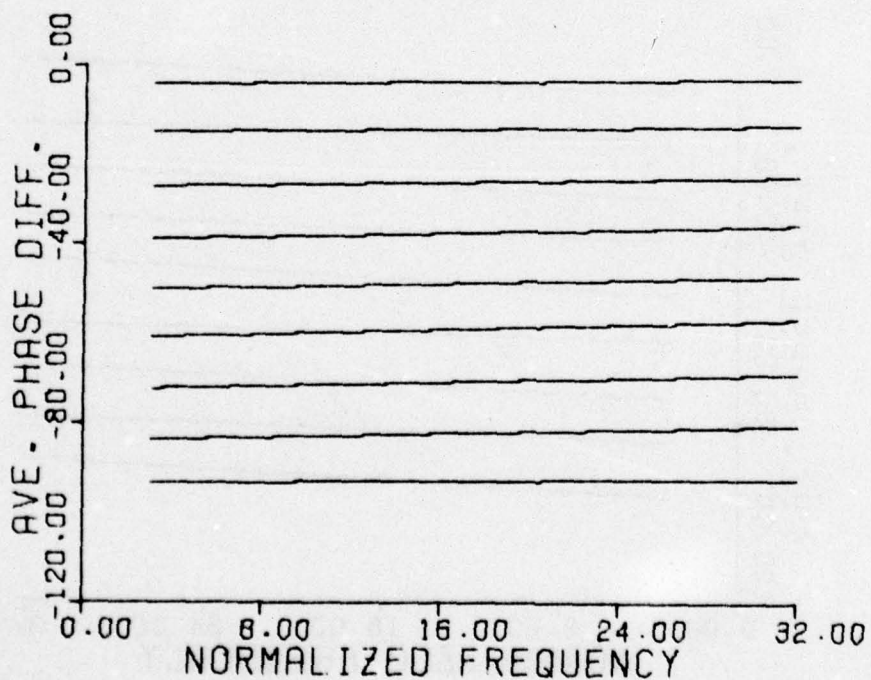


(b) linear least squares fits to functions in (a)

Figure 5.22 Simulation results corresponding to no windowing and Figure 5.1a



(a) phase averages



(b) linear least squares fits to functions in (a)

Figure 5.23 Simulation results corresponding to no windowing and Figure 5.1b

$$\theta_{H_9}(I,J) - \theta_{H_9}(I+1,J) = -90.00^\circ$$

Each curve in Figures 5.22a and 5.23a corresponds to the average

$$\overline{\theta_{G_i}(I,0) - \theta_{G_i}(I+1,0)}$$

corresponding to each of the nine $\theta_{H_k}(I)$ functions. Here i ranged over 225 subimages and the two axes which were lumped together. Each curve in Figures 5.22b and 5.23b is a linear least squares fit to the curves in Figures 5.22a and 5.23a respectively. Note from the least squares fits that the convergence is roughly to the correct phase differences.

Recall, however, that relationship (5-14) has been induced artificially and the problem inherent in approximation (5-8) has not been overcome.

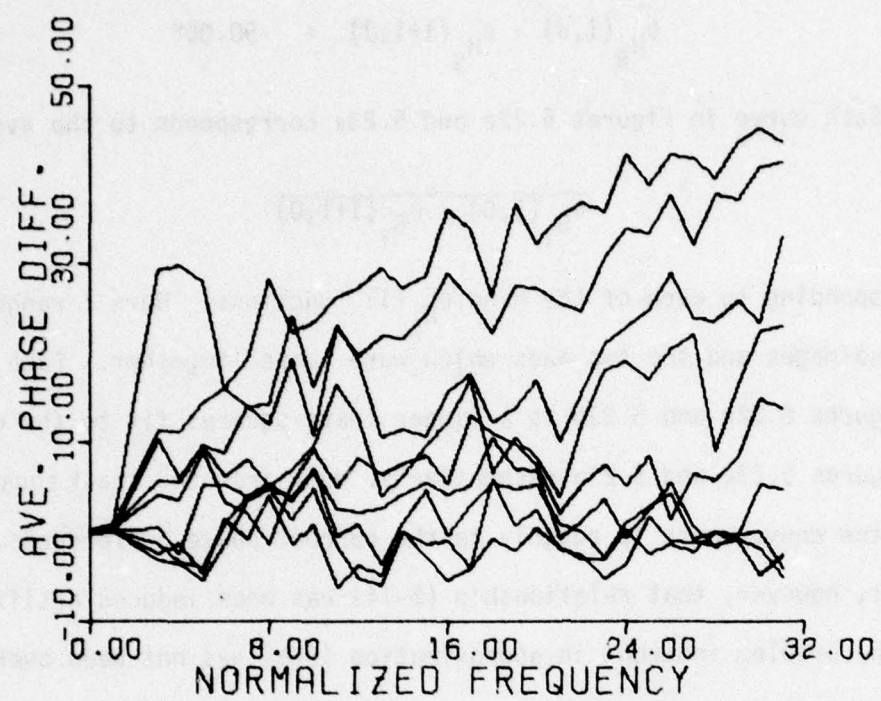
Assuming the same nine phase functions and assuming Parzen windowing, the curves in Figures 5.24 and 5.25 were calculated. Here each curve in Figures 5.24a and 5.25a correspond to the average

$$\overline{\theta_{G_i*W}(I) - \theta_{G_i*W}(I+1)} \quad (5-17)$$

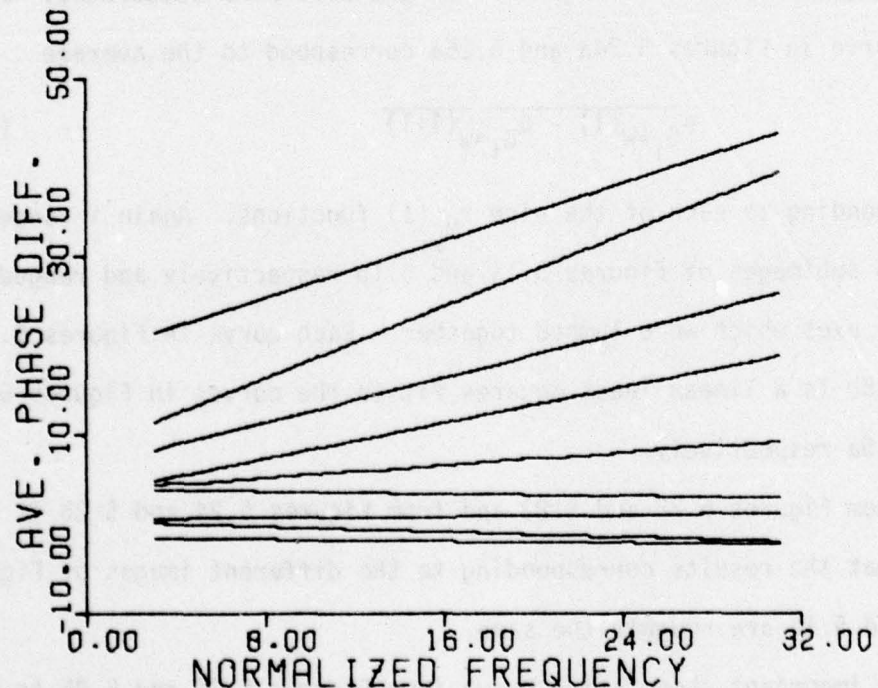
corresponding to each of the nine $\theta_{H_k}(I)$ functions. Again i ranged over the 225 subimages of Figures 5.1a and 5.1b respectively and ranged over the two axes which were lumped together. Each curve in Figures 5.24b and 5.25b is a linear least squares fit to the curves in Figures 5.24a and 5.25a respectively.

From Figures 5.22 and 5.23 and from Figures 5.24 and 5.25 it is seen that the results corresponding to the different images of Figures 5.1a and 5.1b are roughly the same.

An important observation drawn from Figures 5.24 and 5.25 is when assuming a Parzen window, the inability of the averages (5-17) to

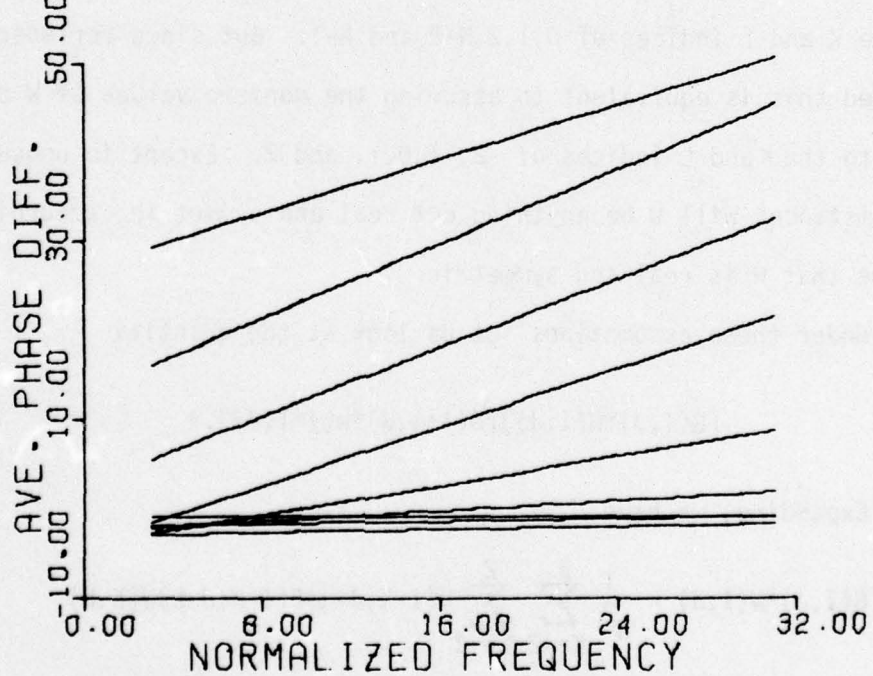
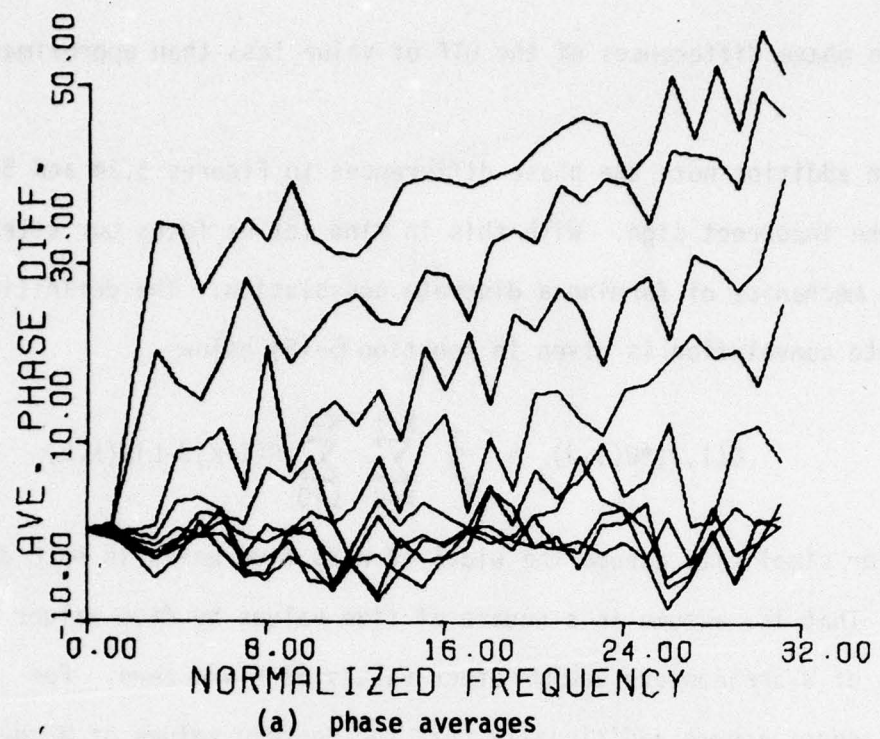


(a) phase averages



(b) linear least squares fits to functions in (a)

Figure 5.24 Simulation results corresponding to Parzen windowing and Figure 5.1a



(b) linear least squares fits to functions in (a)

Figure 5.25 Simulation results corresponding to Parzen windowing and Figure 5.1b

resolve phase differences of the OTF of value less than approximately 40°.

In addition note the phase differences in Figures 5.24 and 5.25 have the incorrect sign. With this in mind let us focus our attention on the mechanics of forming a discrete convolution. The definition of discrete convolution is given in equation (5-18) below

$$G(I,J)*W(I,J) = \frac{1}{N^2} \sum_{K=0}^{N-1} \sum_{L=0}^{N-1} G(I-K, J-L)W(K,L) \quad (5-18)$$

For simplicity assume the width of W is five units in each direction. That is, assume in a square of five values by five values the values of W are nonzero and the other values of W are zero. For definiteness assume additionally that the nonzero values of W correspond to the K and L indices of 0, 1, 2, $N-2$, and $N-1$. But since periodicity is assumed this is equivalent to assuming the nonzero values of W correspond to the K and L indices of -2, -1, 0, 1, and 2. Except in unusual circumstances will W be anything but real and symmetric; accordingly, assume that W is real and symmetric.

Under these assumptions let us look at the quantity

$$[G(I,J)*W(I,J)][G(I+1,J)*W(I+1,J)].* \quad (5-19)$$

Expanding, we have

$$G(I,J)*W(I,J) = \frac{1}{N^2} \sum_{K=-2}^2 \sum_{L=-2}^2 H(I-K, J-L)F(I-K, J-L)W(K,L) \quad (5-20)$$

and

$$[G(I+1,J)*W(I+1,J)].* = \frac{1}{N^2} \sum_{K=-2}^2 \sum_{L=-2}^2 H*(I+1-K, J-L)F*(I+1-K, J-L)W(K,L) \quad (5-21)$$

Multiplying the right hand side of equation (5-20) by the right hand side of equation (5-21) results in the sum of 625 terms. Let us group each of the 625 terms into two categories. The first category consists of terms which contain factors of the form

$$H(I,J)H^*(I,J)F(I,J)F^*(I,J)$$

and the second category consists of all other terms. In this example 20 of the 625 terms would be in the first category.

The terms in the first category contain no phase information, whereas the terms in the second category contain the phase information of the product.

Multiplying equation (5-20) times equation (5-21), we have

$$[G(I,J)*W(I,J)][G(I+1,J)*W(I+1,J)]^* = A(I,J) + B(I,J)$$

where A is the sum of those 20 terms of the first category and B is the sum of the remaining 605 terms of the second category. Figure 5.26 illustrates the vector sum A+B.

Assuming the degraded image is divided into subimages, the corresponding results would be

$$[G_i(I,J)*W(I,J)][G_i(I+1,J)*W(I+1,J)]^* = A_i(I,J) + B_i(I,J) .$$

Recall from Figures 5.4-5.7 that the phase differences corresponding to an unwindowed, undegraded image will on the average be out of phase for one step in the frequency domain. Additionally, the terms implicit in vector B_i which predominate will be those terms associated with one step in the frequency domain. As a result, on the average vector B_i will be out of phase by $\pm\pi$.

Surprisingly, on the average the magnitude of $A_i(I, J)$ is roughly the same as the magnitude of $B_i(I, J)$. Experimental evidence of the calculated average,

$$\frac{1}{100} \sum_{i=1}^{100} \frac{|B_i(I, 0)|}{|A_i(I, 0)|}$$

for I corresponding to the data on axis, using Parzen windowing, and 100 subimages of Figure 5.1a is given in Table 5.3.

This explains the results of Figures 5.4-5.7 compared to the results of Figures 5.8 and 5.9 in the sense that the phase differences corresponding to unwindowed subimages tended to be out of phase while the phase differences corresponding to the Parzen windowed subimages tended to be in phase. For example, assuming vectors A and B are roughly the same magnitude, the vector $A+B$ in Figure 5.26 will tend to have a mean of zero phase even though the vector B will have a mean of $\pm\pi$ phase.

In addition this explains the sign discrepancy in the results of Figures 5.24 and 5.25 where the Parzen window was used. Assuming that the phase between index I and index $I+1$ of the OTF is increasing, the phase difference $\theta_H(I) - \theta_H(I+1)$ will be negative. The average of the vector B corresponding to this index will be as illustrated in Figure 5.27. But the averages corresponding to Figures 5.24 and 5.25 are the averages

$$\overline{\theta_{G_i} * W(I) - \theta_{G_i} * W(I+1)} .$$

In Figure 5.28 is an illustration of the dynamics behind the results of Figures 5.24 and 5.25. This illustration assumes seven subimages for

<u>I</u>	<u>I+1</u>	<u>Average magnitude ratio</u>
0 (DC)	1	.01
2	3	3.30
4	5	.93
6	7	.99
8	9	.91
10	11	1.01
12	13	1.03
14	15	1.00
16	17	.92
18	19	.98
20	21	.96
22	23	1.02
24	25	.93
26	27	.93
28	29	.88
30	31	.90

Table 5.3 Average magnitude ratio of category two vectors divided by category one vectors

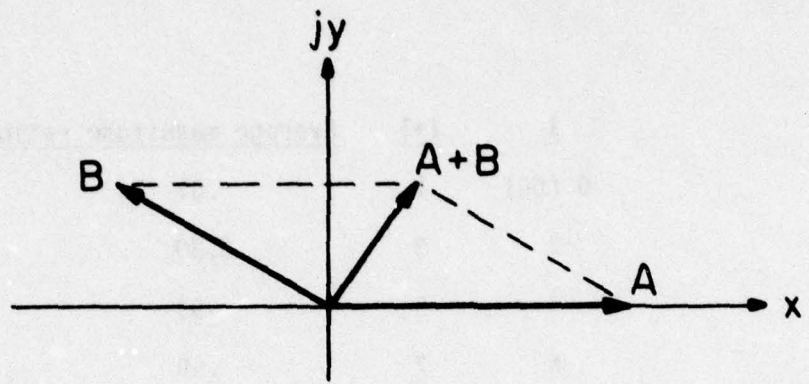


Figure 5.26 Vector sum $A+B$

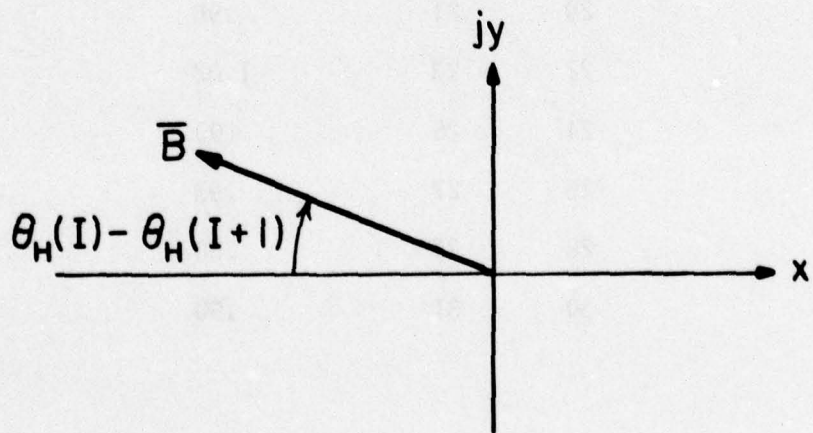


Figure 5.27 Average vector B corresponding to $H(I)$

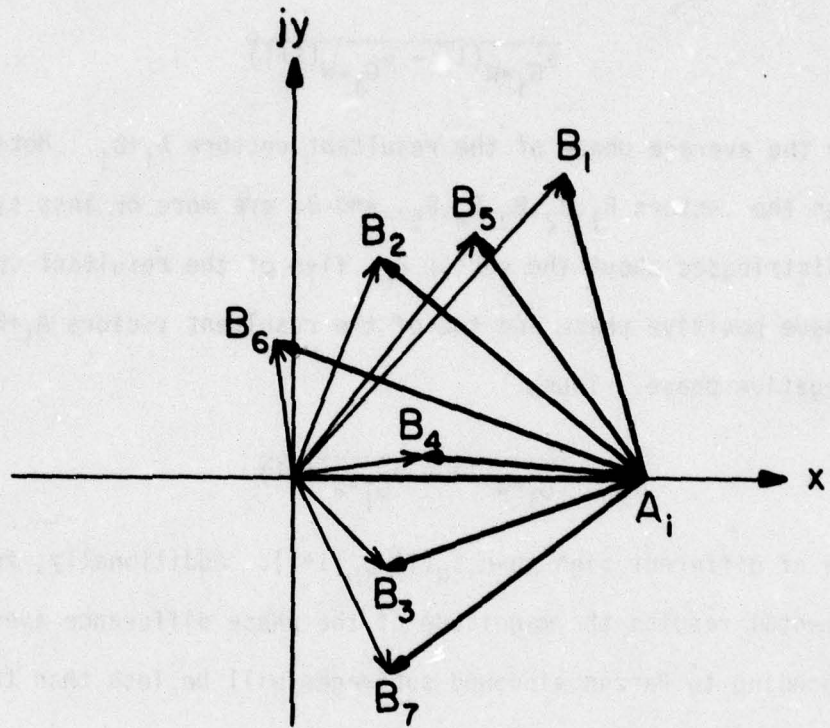


Figure 5.28 The resultants $A_i + B_i$

simplicity. Assume that \bar{B} is roughly the vector denoted by B_6 . Note that each of the A_i have zero phase and that $\theta_H(I) - \theta_H(I+1)$ is roughly -30° . The quantity

$$\overline{\theta_{G_i*W}(I) - \theta_{G_i*W}(I+1)}$$

will be the average phase of the resultant vectors $A_i + B_i$. Note that although the vectors B_1, B_2, B_3, B_4, B_5 , and B_7 are more or less symmetrically distributed about the vector B_6 , five of the resultant vectors $A_i + B_i$ have positive phase and two of the resultant vectors $A_i + B_i$ have negative phase. Thus,

$$\overline{\theta_{G_i*W}(I) - \theta_{G_i*W}(I+1)}$$

will be of different sign than $\theta_H(I) - \theta_H(I+1)$. Additionally, from the experimental results the magnitude of the phase difference average corresponding to Parzen windowed subimages will be less than the magnitude of the phase difference of the underlying OTF.

5.6 On Phase Averaging

Forming a phase average presents difficulties. Usually one only knows the principal value of the phase. Illustrated in Figure 5.29 is a representation of the complex value for an example $H(u, v)$, i.e., $H(u_1, v_1)$. Here x and y refer to the complex number $z=x+jy$. Normally one does not know whether the phase of $H(u_1, v_1)$ is $\theta_H(u_1, v_1)$ as illustrated or $\theta_H(u_1, v_1) \pm 2\pi i$ where i is an integer.

Using the definition (5-22) as the definition of the average may lead to incorrect results.

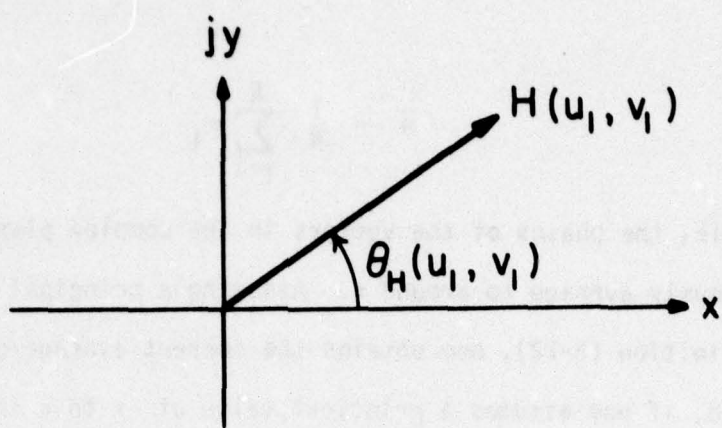


Figure 5.29 Representation of the complex value $H(u_1, v_1)$

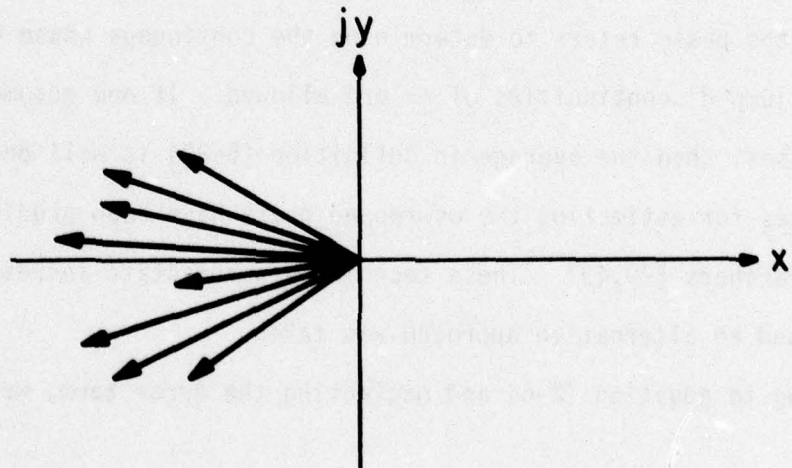


Figure 5.30 Vectors of average phase of roughly π radians

$$\bar{\theta} = \frac{1}{N} \sum_{i=1}^N \theta_i \quad (5-22)$$

For example, the phases of the vectors in the complex plane of Figure 5.30 obviously average to around π . Assuming a principal value of 0 to 2π in definition (5-22), one obtains the correct average of π . On the other hand, if one assumes a principal value of $-\pi$ to π in definition (5-22), then the average phase will be an erroneous 0.

Because the Fourier transform of a continuous function is continuous, the real and imaginary parts of the Fourier transform are continuous. As a result, for the most part the phase of the Fourier transform is continuous. The exception being possible jump discontinuities of $\pm\pi$ when the complex valued Fourier transform goes through 0.

"Unwrapping" the phase refers to determining the continuous phase where the possible jump discontinuities of $\pm\pi$ are allowed. If one assumes unwrapped phases, then the average in definition (5-22) is well defined.

Techniques for estimating the unwrapped phase have been studied by other researchers [29,49]. These techniques necessitate increased computation and an alternative approach was taken.

Referring to equation (2-6) and neglecting the error term, we have

$$\begin{aligned} \theta_{G_i}(u,v) - \theta_{G_i}(u+\Delta u, v+\Delta v) &\approx \theta_H(u,v) - \theta_H(u+\Delta u, v+\Delta v) \\ &\quad + \theta_{F_i}(u,v) - \theta_{F_i}(u+\Delta u, v+\Delta v) . \end{aligned}$$

The phase difference corresponding to the degraded subimage is the sum of the phase difference of the OTF and the phase difference corresponding to the undegraded subimage. For a fixed $u, v, \Delta u$, and Δv , say $u=u_1$,

$v=v_1$, $\Delta u=\Delta u_1$, and $\Delta v=\Delta v_1$, $\theta_H(u_1, v_1) - \theta_H(u_1 + \Delta u_1, v_1 + \Delta v_1)$ will be fixed for each subimage and

$$\theta_{F_i}(u_1, v_1) - \theta_{F_i}(u_1 + \Delta u_1, v_1 + \Delta v_1)$$

will vary from subimage to subimage. For example, in Figure 5.31a is represented a unit vector of phase equal to $\theta_H(u_1, v_1) - \theta_H(u_1 + \Delta u_1, v_1 + \Delta v_1)$; in Figure 5.31b is represented unit vectors corresponding to $\theta_{F_i}(u_1, v_1) - \theta_{F_i}(u_1 + \Delta u_1, v_1 + \Delta v_1)$ associated with several subimages; Figure 5.31c represents the unit vectors obtained by summing the phase difference in Figure 5.31a to each of the phase differences in Figure 5.31b. Note that the vectors in Figure 5.31c are the vectors in Figure 5.31b rotated by the phase of the vector in Figure 5.31a.

If the phase differences in Figure 5.31b are of zero mean, then the mean of the phase differences in Figure 5.31c should be

$$\theta_H(u_1, v_1) - \theta_H(u_1 + \Delta u_1, v_1 + \Delta v_1) .$$

For this example definition (5-22) can again lead to erroneous results. Again the assumed principal value will affect the average. That is, whether the vector in quadrant III of Figure 5.31c is considered to be in the range π to $3\pi/2$ or in the range $-\pi/2$ to $-\pi$ will affect the phase average. Also, whether the vector in quadrant IV of Figure 5.31c is considered to be in the range $3\pi/2$ to 2π or in the range 0 to $-\pi/2$ will affect the phase average.

This problem may be circumvented as follows. The complex plane is divided into phase zones. For example, in Figure 5.32 the complex plane has been divided into eight phase zones. A histogram can be

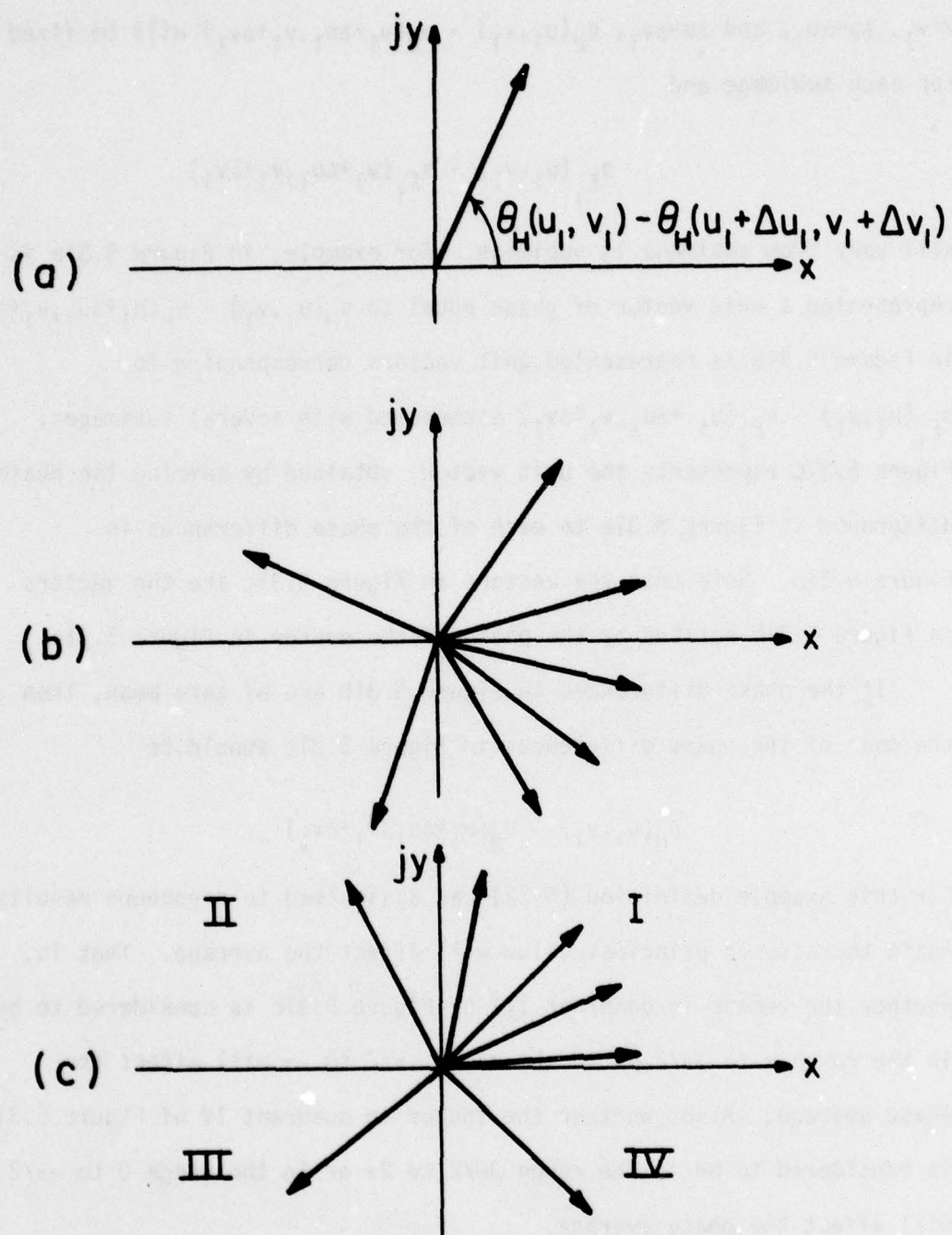


Figure 5.31 a) Representation of phase difference corresponding to OTF b) Representation of phase differences corresponding to undegraded subimages c) Representation of phase differences corresponding to degraded subimages

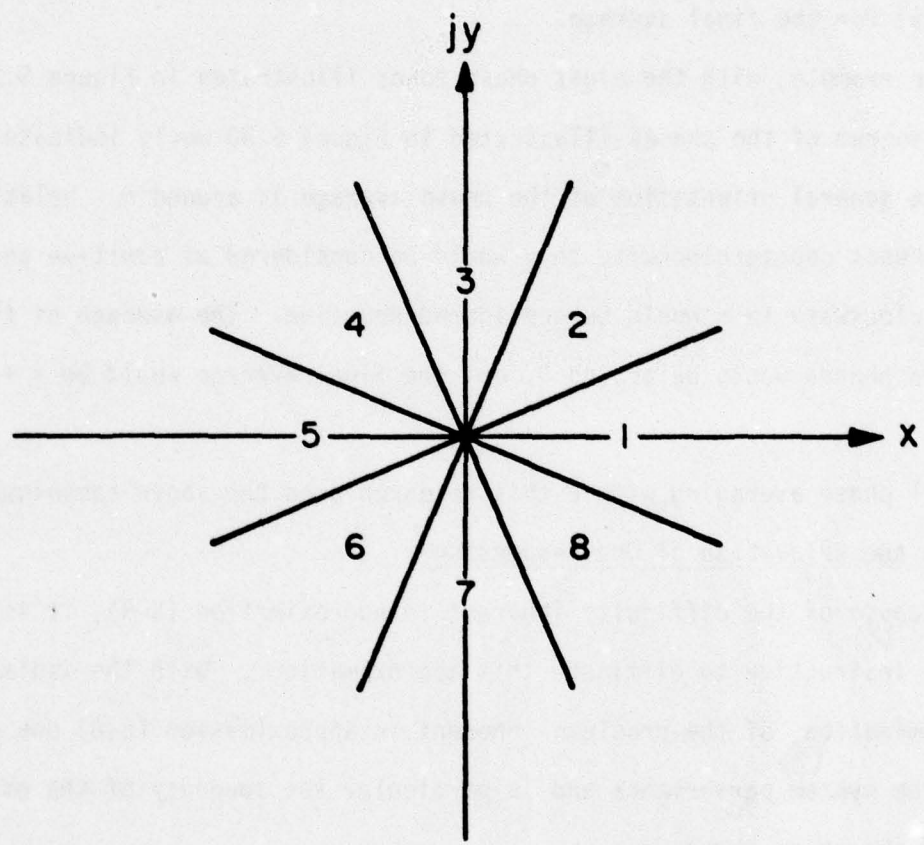


Figure 5.32 Phase zones

constructed of the number of phases included in the average which fall into each of the phase zones. Using the histogram information, the general orientation of the phase average can be estimated. Denoting this phase by $\theta(u,v)$, all phases in the average are now made relative to $\theta(u,v)$. The relative phases are averaged. This average is then added to $\theta(u,v)$ for the final average.

For example, with the eight phase zones illustrated in Figure 5.32 the histogram of the phases illustrated in Figure 5.30 would indicate that the general orientation of the phase average is around π . Relative to π , phases counterclockwise to π would be considered as positive and phases clockwise to π would be considered negative. The average of the relative phases would be around 0, and the final average would be $\pi + 0 = \pi$.

All phase averaging within this research used the above technique.

5.7 On the Relaxation of One Assumption

Because of the difficulty inherent in approximation (5-8), it is perhaps instructive to eliminate this approximation. With the isolation and elimination of the problems inherent in approximation (5-8) one can study the system performance and in particular the adequacy of the estimate of the phase averages

$$[\theta_{F_i}(u,v) - \theta_{F_i}(u+\Delta u, v+\Delta v)] ,$$

the adequacy of the phase averaging technique, and additionally the adequacy of the rates of convergence of the phase averaging.

This approximation can be eliminated in the simulations by the following method. Recall that within a half width of the PSF from the

edge of a subimage, approximation (5-8) is not approximate but equal. As a result, if one zeros the edges of the subimages of the undegraded image to an extent greater than a half width of the PSF and then blurs the resulting image via convolution, approximation (5-8) is now equality everywhere.

For example, Figure 5.33a is an example of an image zeroed at the edges of the subimages and Figure 5.33b is the result after blurring.

The estimate of the average phase differences of the undegraded image is no longer zero. In this case the average phase differences will converge to the phase differences associated with the subimage of Figure 5.34. One can use the mathematical function such as illustrated in Figure 5.34 to estimate the average phase differences associated with the undegraded image or one can use a similar zeroed undegraded image to estimate the average phase differences associated with the undegraded image. The latter approach was used in the simulations to follow.

If one zeros the edges of the subimages of an image and then calculates the average phase differences, one could then display the average phase differences. On the other hand, a more esthetically pleasing display is usually obtained by starting with the phase at the DC term of zero and using the average phase differences to recursively calculate a continuous phase plane.

Accordingly, zeroing the edges of the subimages corresponding to Figure 5.1b, calculating the associated average phase differences, using the phase of the DC term of zero and recursively calculating the phase plane from the average phase differences, the phase plane dis-



(a)



(b)

Figure 5.33 An image zeroed at the edges of the subimages and then blurred

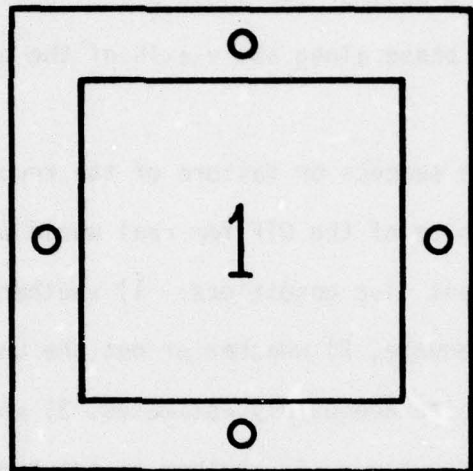


Figure 5.34 Average phase differences of zeroed undegraded image will converge to phase differences associated with above subimage

played in Figure 5.35a was obtained. This is the same phase plane as would be obtained by Fourier transforming the function in Figure 5.34 and displaying the unwrapped phase plane. Plotted in Figure 5.35b is the phase along the u-axis of the phase plane, while plotted in Figure 5.35c is the phase along the v-axis of the phase plane.

5.8 Summary

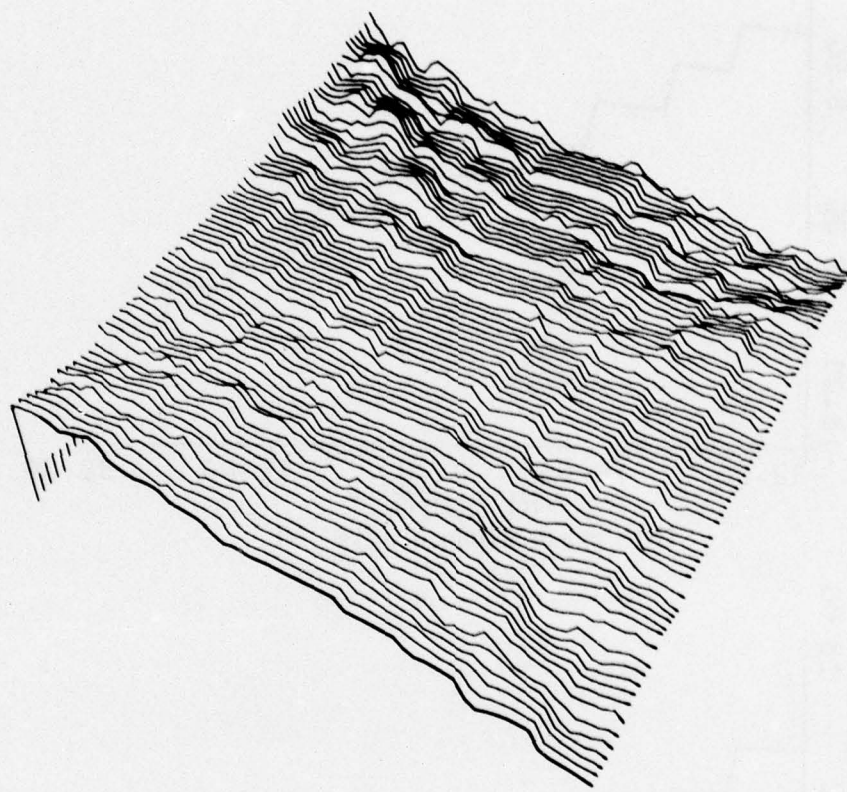
Recall that the success or failure of the recursive estimates of the magnitude and phase of the OTF for real world blurred imagery is contingent on at least five conditions: 1) whether or not the mathematical model is adequate, 2) whether or not the unknown quantities in the estimates can be adequately estimated, 3) whether or not the averages converge adequately, 4) whether or not the iterations are stable, and 5) whether or not the error inherent in the approximations are acceptable. Additionally, recall the success or failure of the phase recursion is dependent on the adequacy of techniques which assume only knowledge of the principal value of the phase.

Table 5.4 summarizes the system performance with respect to the above contingencies.

The ill-conditioned nature of the phase causes most approximations to be suspect. In particular, the approximation

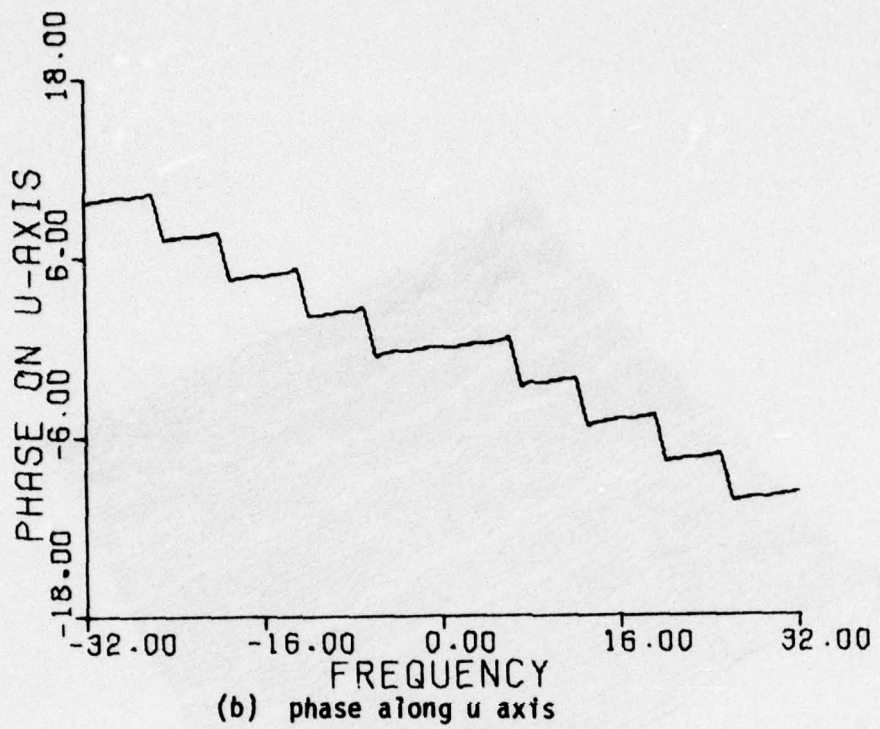
$$\theta_{G_i}(u,v) \approx \theta_H(u,v) + \theta_{F_i}(u,v) \quad (5-23)$$

is not a particularly good approximation in general. Windowing can sharpen the approximation, but at the same time the windowing causes a loss of resolution in the estimate of the phase differences. In the simulations presented in Chapter 6 it will be demonstrated that with

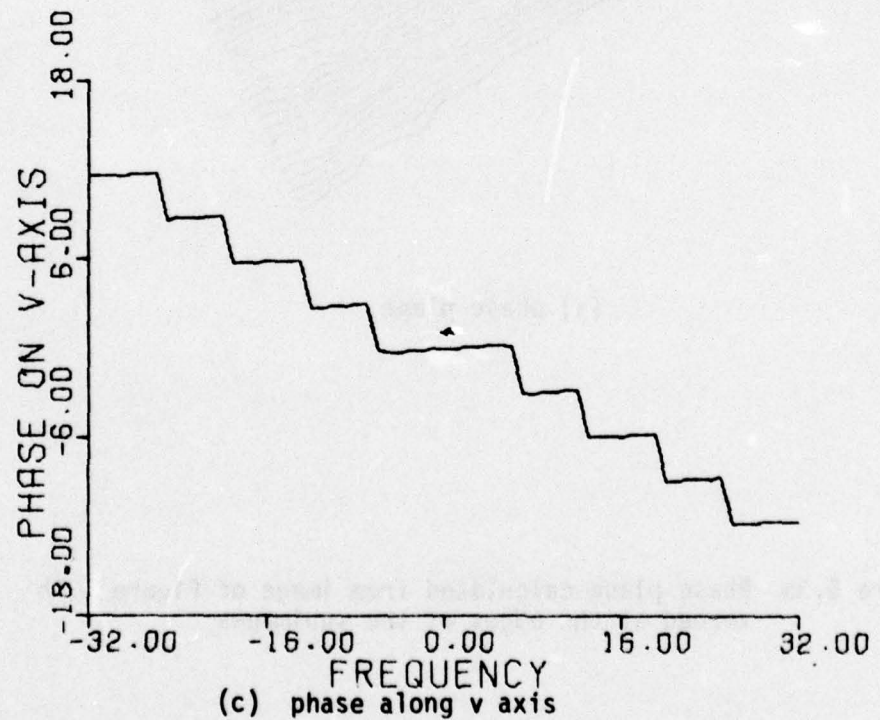


(a) phase plane

Figure 5.35 Phase plane calculated from image of Figure 5.1b zeroed at the edges of the subimages



(b) phase along u axis



(c) phase along v axis

Figure 5.35 (Cont'd) Phase plane calculated from image of Figure 5.1b zeroed at the edges of the subimages

	Magnitude recursion	Phase recursion
Model	adequate	adequate
Estimate of unknown quantities	adequate	adequate
Convergence of averages	adequate	adequate
Stability of iteration	conditionally unstable	stable
Approximations acceptable	acceptable	conditionally unacceptable
Adequacy of assuming only principal value of the phase		adequate

Table 5.4 Summary of adequacy of contingencies upon which recursion depends

the elimination of this approximation, via the method of section 5.7, the phase recursion gives reasonable estimates of the phase.

Windowing is one approach to sharpening the approximation. Another approach is to increase the subimage size. For example, if the PSF is nonzero over an extent of 7×7 pixels, for a subimage size of 64×64 pixels the relationship

$$g_i(x,y) \approx h(x,y)*f(x,y) \quad (5-24)$$

will be exact except for at most 19% of the 64×64 pixels. If the subimage size is 256×256 pixels, relationship (5-24) will be exact except for at most 5% of the 256×256 pixels. At some point the subimage size will be large enough such that the approximation (5-23) will contain sufficient accuracy to support a reasonable estimate of the phase.

Note, however, that given an image, as the subimage size increases the number of subimages of the given image decreases. Thus, it may be necessary to have a very large image and very large subimages for approximation (5-23) to support an accurate estimate of the phase.

Chapter 6

RESULTS OF SIMULATIONS

6.1 Presentation of Results

In this chapter will be presented the results of computer simulations for a variety of blurs. The format of presentation will be as follows. First, a diagram of the degrading PSF will be presented. This will be followed by a comparison of the magnitude of the OTF and the corresponding estimate. Because of the unstable nature of the recursive estimate of the magnitude of the OTF, the magnitude estimate was calculated via the method of Cannon [26-28]. Next, comparisons of the phase of the OTF against two estimates of the phase will be presented. The first phase estimate was obtained using recursion (5-2) and the method outlined in section 5.7; the second phase estimate was obtained using Parzen windowing and using recursion (5-13). Recall the method of section 5.7 relaxed one assumption. The first estimate will be referred to as Estimate 1 and the second estimate will be referred to as Estimate 2.

The degraded image together with seven restorations will then be presented. The assumptions underlying the seven restorations are given in Table 6.1.

As regards the diagram of the degrading point spread functions, the point spread functions are assumed to be lossless. Thus, the volumes under the point spread functions are assumed to be unity.

All plots comparing the magnitude of the OTF are of the \log_{10}

<u>Figure</u>	<u>OTF magnitude</u>	<u>OTF phase</u>	<u>Power spectrum of undegraded image</u>
b	given	given	given
c	given	estimated as 0	given
d	given	Estimate 2	given
e	estimated	given	estimated
f	estimated	estimated as 0	estimated
g	estimated	Estimate 2	estimated
h	estimated	Estimate 1	estimated

Table 6.1 Key to restorations

of the magnitude and are all presented on the same scale. For comparison purposes values of the \log_{10} of the magnitude below -2 have been set to -2 and in all cases the bottom of the skirt is at the -2.1 level. Because the point spread functions are assumed to be lossless, the \log_{10} of the DC term of the point spread function will be 0. Accordingly, the \log_{10} magnitude plot of the optical transfer functions will range from 0 to -2.1, the bottom of the skirt.

The estimate of the power spectrum of the undegraded image, i.e. of the image of Figure 5.1a, was the average power spectrum of the power spectra of the images of Figures 5.1b, c, and d.

Phase Estimate 1 used the image of Figure 5.1b as outlined in section 5.7 to estimate the phase differences associated with the undegraded image. In addition, phase Estimate 1 used subimages of 64 x 64 pixels and no overlapping of subimages. This resulted in an averaging over 64 subimages.

Phase Estimate 2 estimated the average phase differences corresponding to the undegraded image as zero. As did phase Estimate 1, phase Estimate 2 used a subimage size of 64 x 64 pixels. Unlike phase Estimate 1, however, phase Estimate 2 used a 50% overlapping of subimages. Thus, the averaging was over 225 subimages.

In each figure which compares the phase of the OTF and the corresponding estimates, the plot scaling is identical within the given figure, on the other hand, to adequately present different ranges of phase variations for different point spread functions, the scaling is usually different from figure to figure.

6.2 Discussion

Upon comparison of the magnitudes of the optical transfer functions and the estimates of the magnitudes, it is clear that the estimates adequately retain the essential features. The magnitude estimates resolve the essential features to at most 1 1/2 orders of magnitude. Most would agree that this is fairly good, especially in light of the fact that the degraded images which were input to the system were given to at most 8 binary digits (bits) of accuracy.

Upon comparison of the phases of the optical transfer functions and the estimates of the phases, it is evident that phase Estimate 1 is reasonable near the axes and not as accurate at a distance from the axes. Because images in general have little energy concentration in those frequency components away from the axes, the poorer results away from the axes are not very important from a restoration point of view.

Some of the differences observed between the phases of the optical

transfer functions and phase Estimates 1 are due to the unwrapping. It should be emphasized that a consistent unwrapping is necessary for an esthetically pleasing display, but not for the Wiener filter. Some unwrapping problems are evident. For example, in Figure 6.4a it may be noted that at one point the display of the phase of the OTF jumped $-\pi$ and at the same point the display of phase Estimate 1 jumped $+\pi$. Other unwrapping problems are apparent, for example, see Figures 6.14b, 6.19a, and 6.19b.

In addition, some of the differences observed between the phases of the optical transfer functions and phase Estimates 1 are due to the tendency of the phase estimates to contain a slight linear term. The slight linear term causes only a slight shift in the picture domain and is not responsible for any blurring; thus, it is of minor consequence. However, on comparing the displays of the phases of the optical transfer functions and the displays of the corresponding estimates, the comparisons are less favorable. For example, upon comparing the phase of the OTF and Estimate 1 in Figures 6.9a and 6.9b, it is evident that, if not for a slight linear term in Estimate 1, the estimate would be even closer. This effect is also evident in Figures 6.19a and b, 6.24b, and 6.29 a and b.

From the phase comparisons it may be noted that phase Estimate 2 is not particularly good.

Comparing restorations, it is apparent that the estimate of the magnitude of the OTF is reasonable to the extent of achieving an adequate restoration. In fact, the visual quality of the restorations using the estimate of the magnitude of the OTF seems to be superior to

the restorations given knowledge of the magnitude of the OTF. For example, compare Figures 6.10 b and e, Figures 6.15 b and e, Figures 6.20 b and e, and Figures 6.30 b and e. In general, upon restoration, the frequencies in the vicinity of the zeros of the OTF will be magnified the most by the Wiener filter. If one knows the magnitude of the OTF exactly, at times the restoration will contain periodic artifacts corresponding to those frequencies that were boosted the most by the filter. On the other hand, the inaccuracies inherent in the estimate of the magnitude of the OTF cause the frequencies in the vicinity of the zeros to be boosted less than the boost assuming knowledge of the magnitude of the OTF. As a result, when assuming the estimate of the magnitude of the OTF, in most cases the periodic artifacts are missing.

Although the visual quality of the restoration is usually superior when using the estimate of the magnitude of the OTF, in terms of minimum mean squared error, restoration b is superior in all cases.

Upon comparing restorations c and d of a set and restorations f and g of a set, it is generally agreed that Estimate 2 of the phase is not significantly better with respect to restoring than an estimate of zero for the phase.

The superiority of Estimate 1 of the phase is evident. For example, note in Figures 6.5 f and g the double set of eyes and the collar of the man; also note the streak of light across the arm and chest of the woman and below the knees of the woman. These anomalies are absent in Figure 6.5h. Note in Figure 6.15h the elimination of the double image in Figures 6.15 f and g. Note the clearer definition of the faces in

Figure 6.25h opposed to the faces in Figures 6.25 f and g. Additionally, note the general superiority of Figure 6.30h over Figures 6.30 f and g.

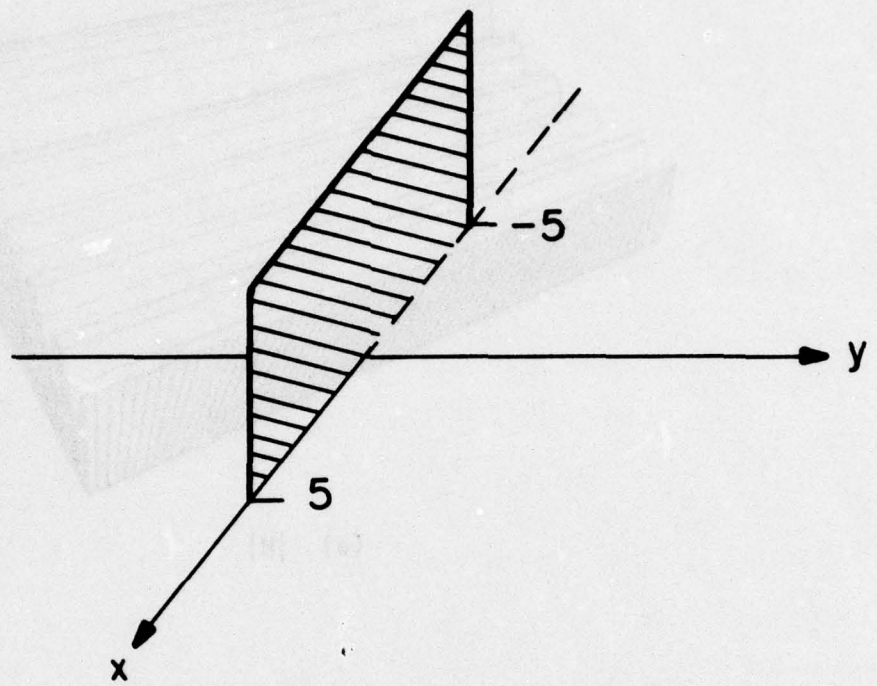
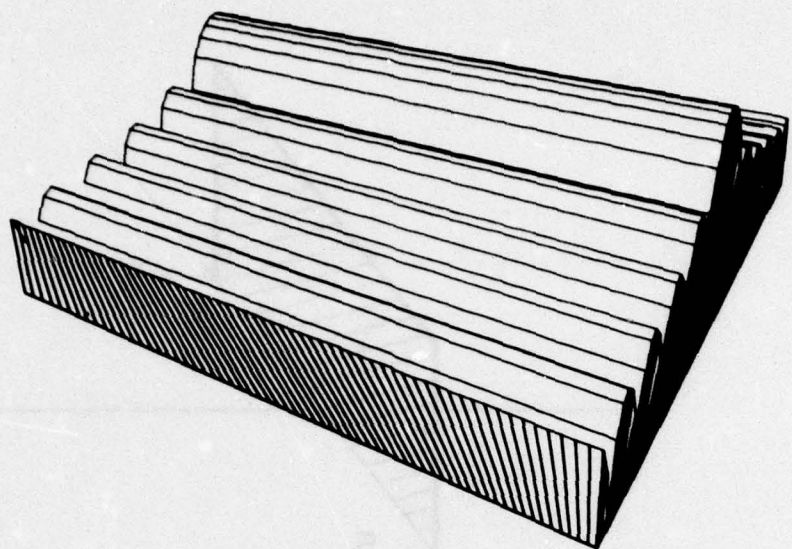
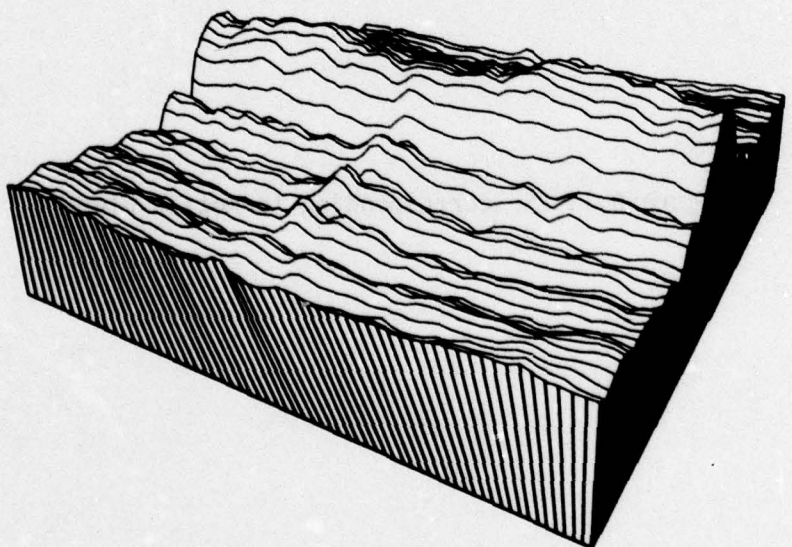


Figure 6.1 PSF corresponding to motion blur

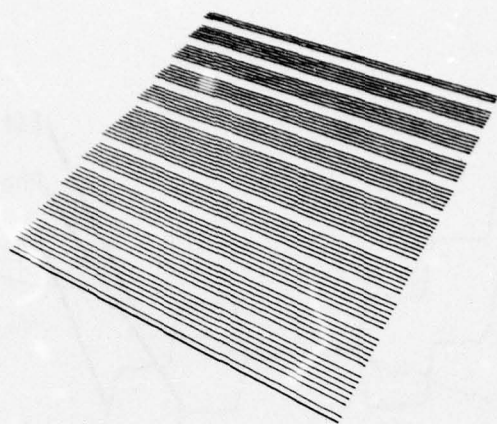


(a) $|H|$

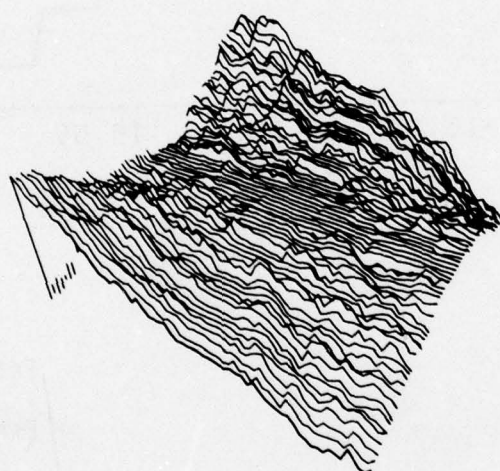


(b) $|\hat{H}|$

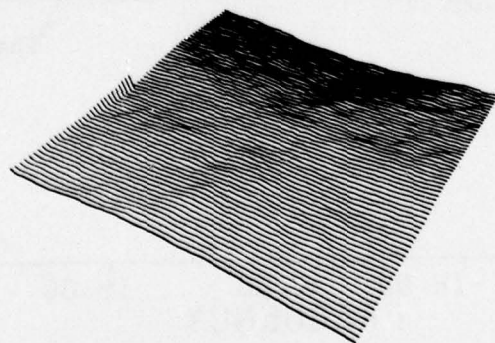
Figure 6.2 Comparison of magnitude of OTF and estimate



(c) θ



(b) $\hat{\theta} = \text{Estimate 1}$



(c) $\hat{\theta} = \text{Estimate 2}$

Figure 6.3 Comparison of phase of OTF and estimates

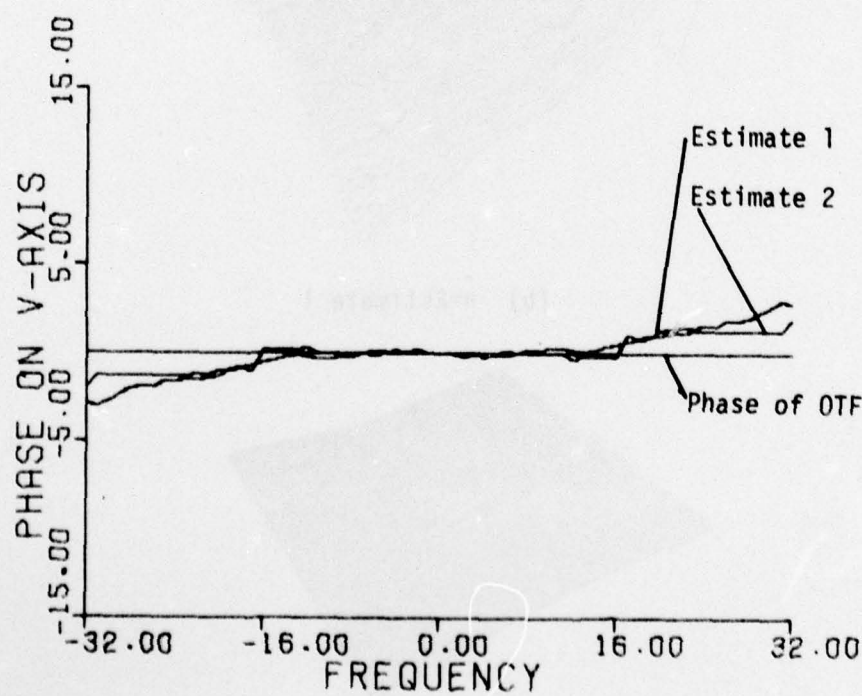
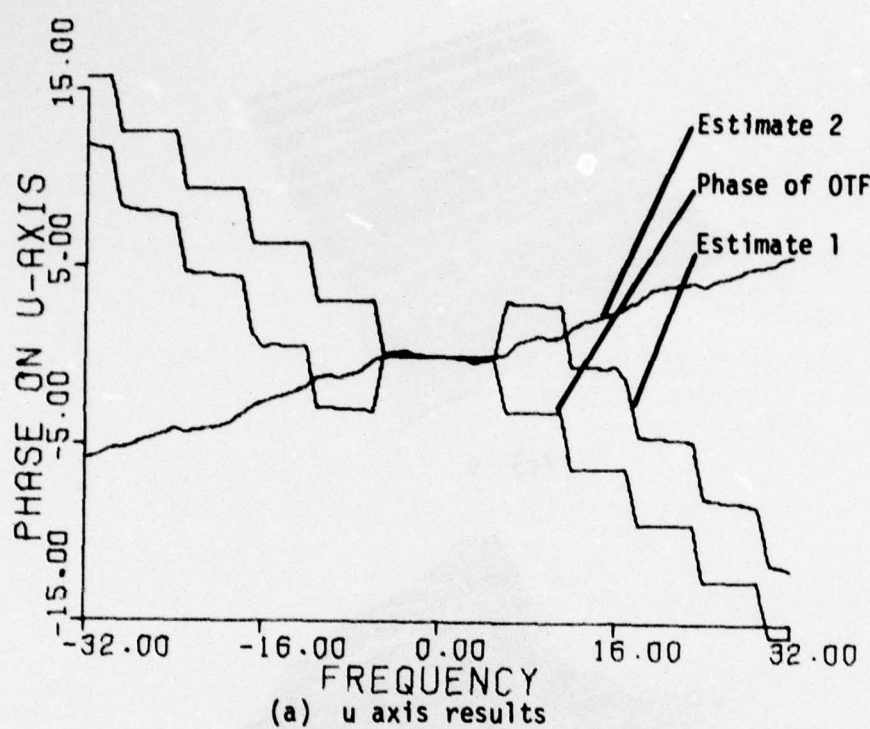


Figure 6.4 Comparison of phase of OTF and estimates

**Best
Available
Copy**



(a) degraded image



(b) magnitude of OTF given
phase of OTF given



(c) magnitude of OTF given
phase of OTF estimated
as 0



(d) magnitude of OTF given
Phase estimate = Estimate 2

Figure 6.5 Restorations



(e) magnitude of OTF estimated
phase of OTF given



(f) magnitude of OTF esti-
mated, phase of OTF esti-
mated as 0



(g) magnitude of OTF estimated
phase estimate = Estimate 2



(h) magnitude of OTF esti-
mated, phase estimate =
Estimate 1

Figure 6.5 (Cont'd)

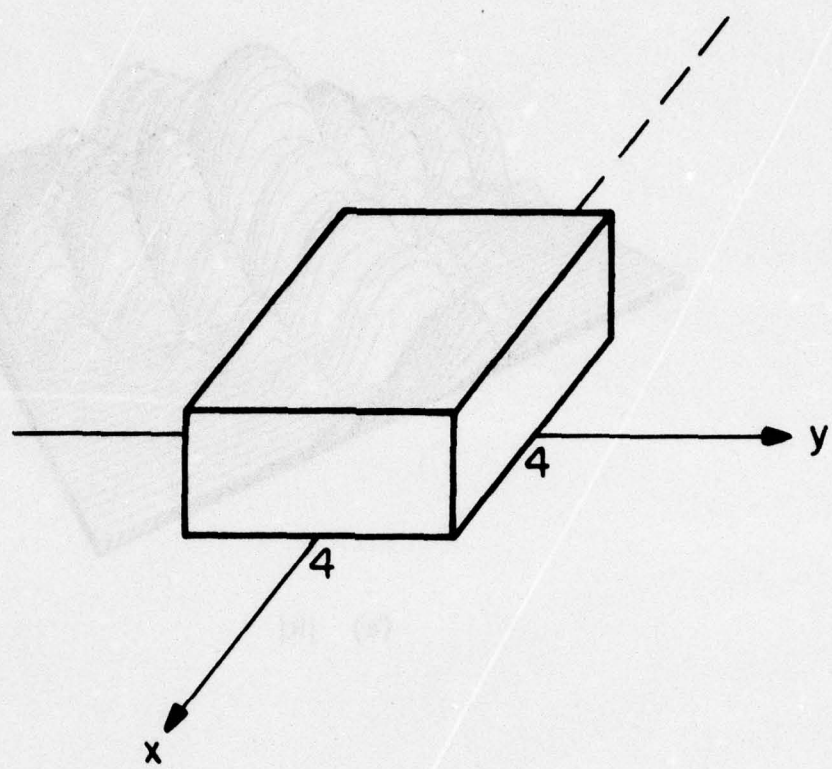
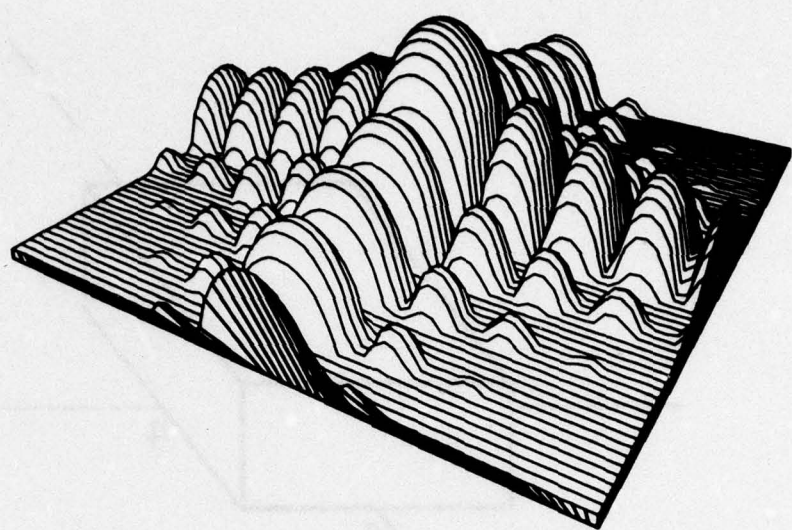
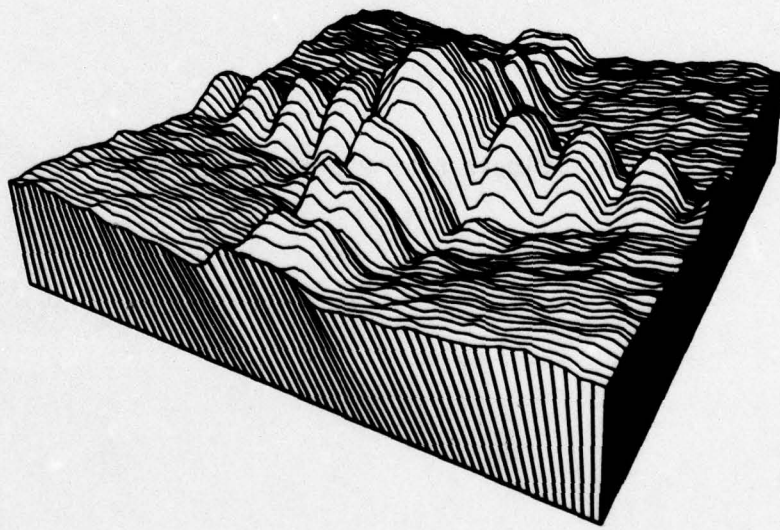


Figure 6.6 PSF of square blur

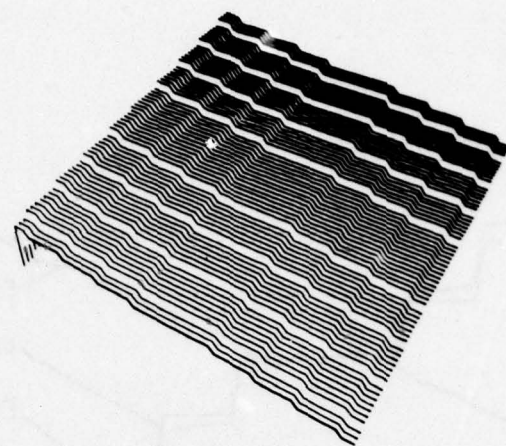


(a) $|H|$

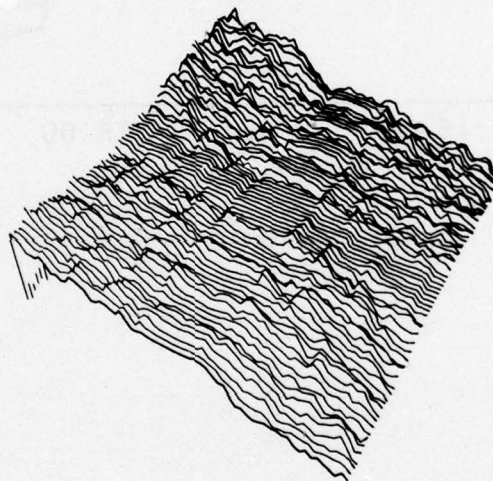


(b) $|\hat{H}|$

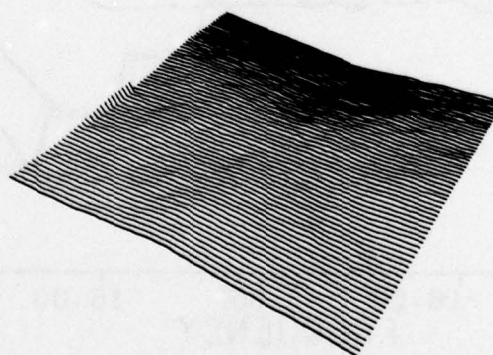
Figure 6.7 Comparison of magnitude of OTF and estimate



(a) θ

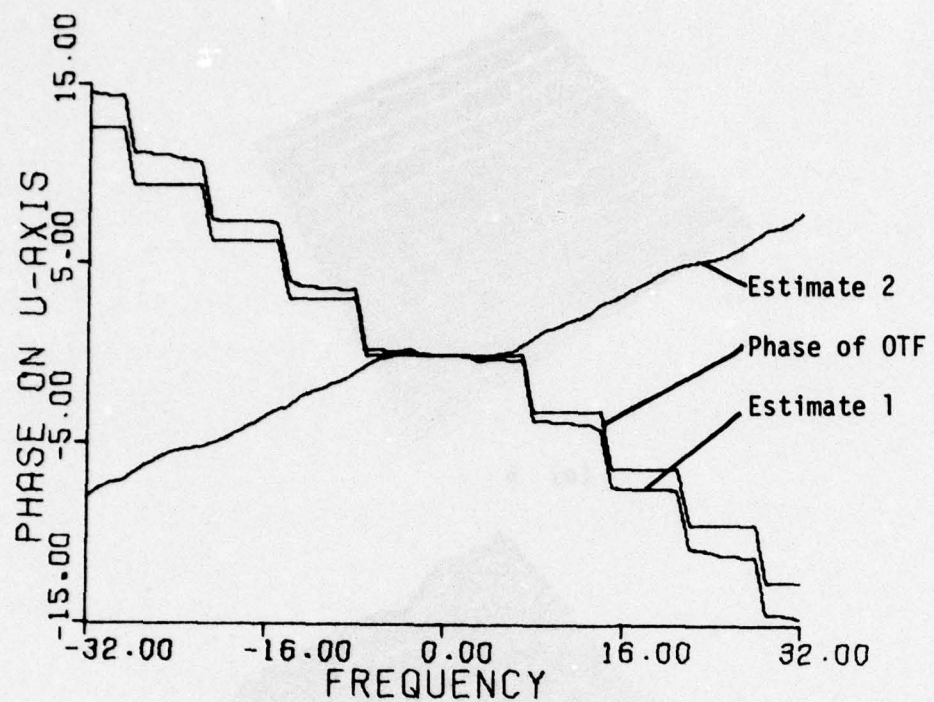


(b) $\hat{\theta} = \text{Estimate 1}$

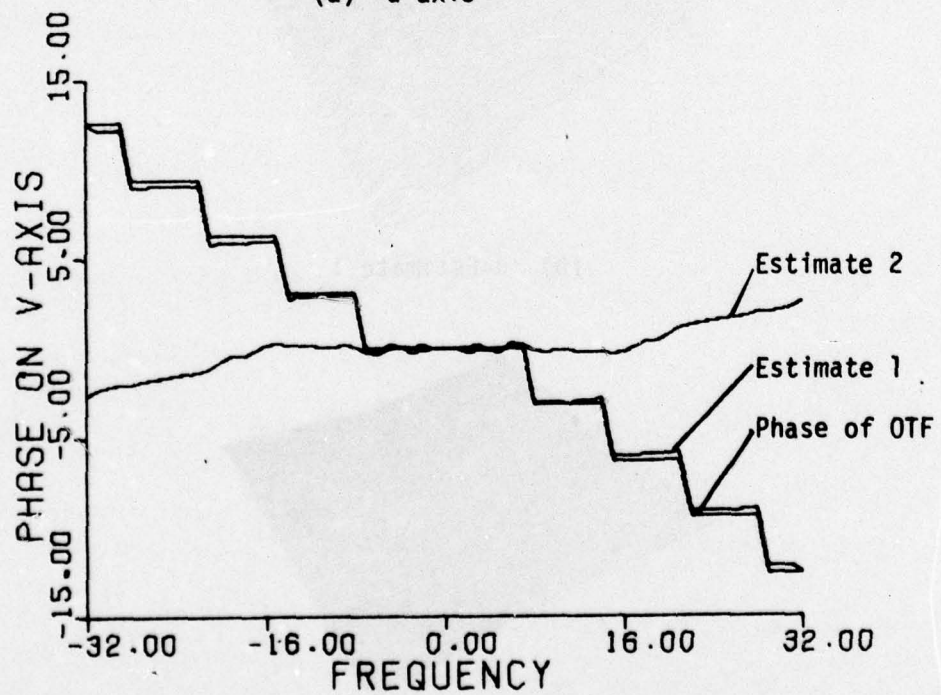


(c) $\hat{\theta} = \text{Estimate 2}$

Figure 6.8 Comparison of Phase of OTF and estimates



(a) u axis

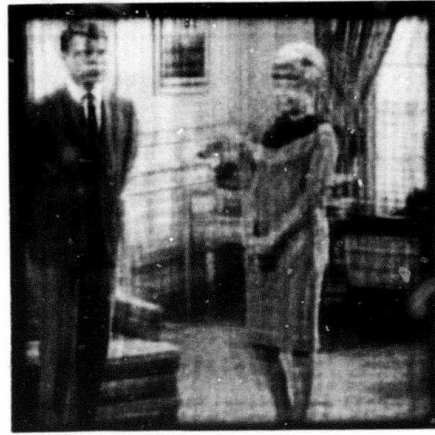


(b) v axis results

Figure 6.9 Comparison of phase of OTF and estimates



(a) degraded image



(b) magnitude of OTF given
phase of OTF given



(c) magnitude of OTF given
phase of OTF estimated as 0



(d) magnitude of OTF given
phase estimate =
Estimate 2

Figure 6.10 Restorations



(e) magnitude of OTF estimated
phase of OTF given



(f) magnitude of OTF esti-
mated, phase of OTF
estimated as 0



(g) magnitude of OTF estimated
phase estimate = Estimate 2



(h) magnitude of OTF esti-
mated, phase estimate =
Estimate 1

Figure 6.10 (Cont'd)

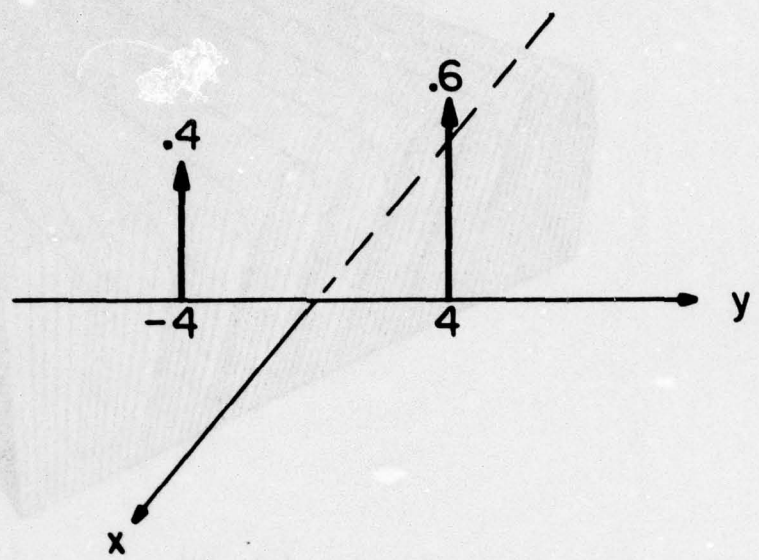
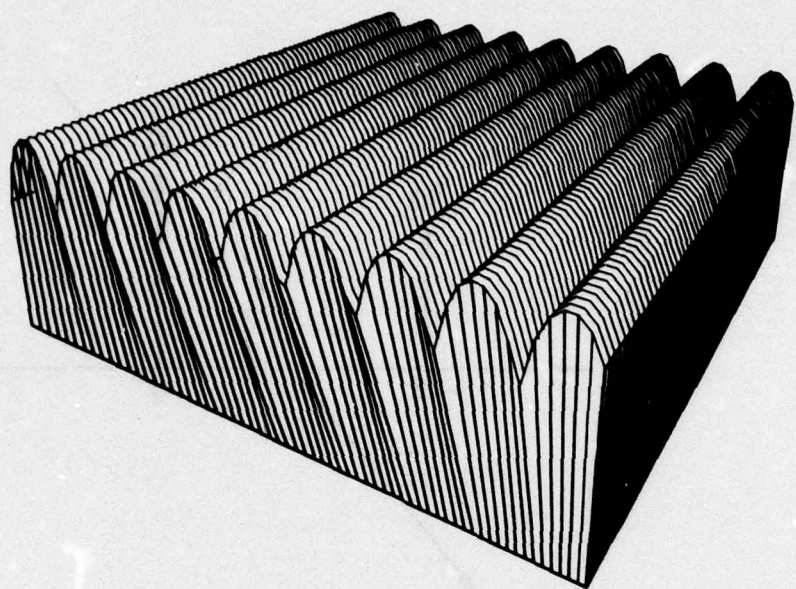
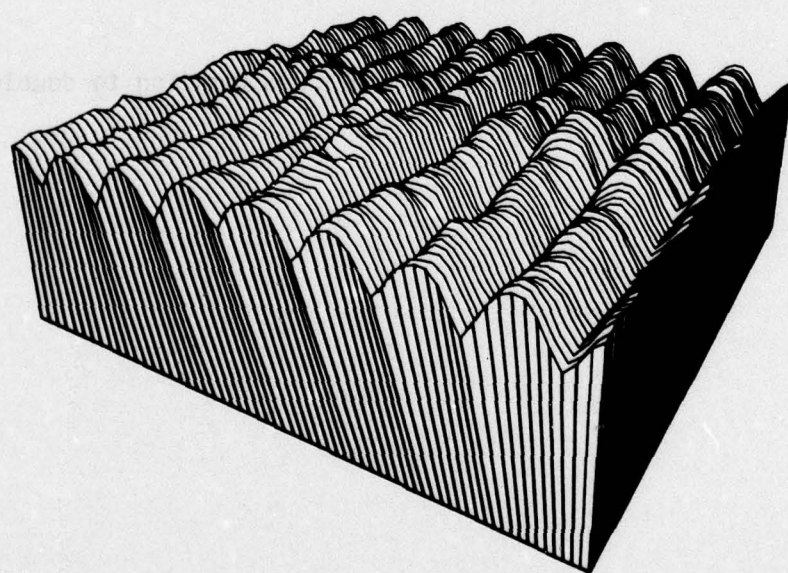


Figure 6.11 PSF corresponding to double exposure

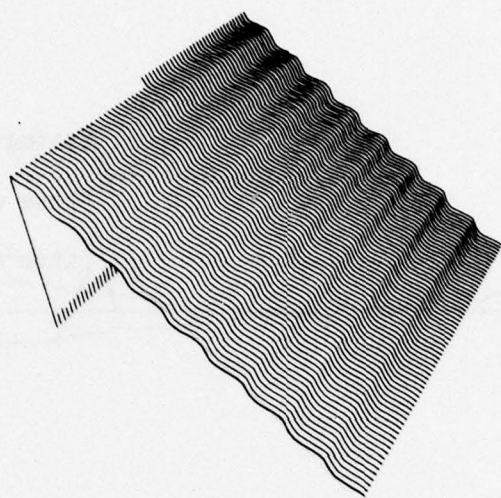


(a) $|H|$

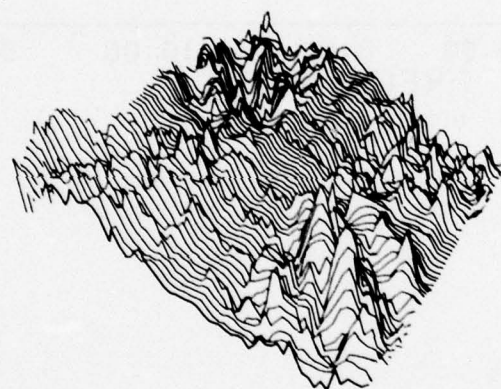


(b) $|\hat{H}|$

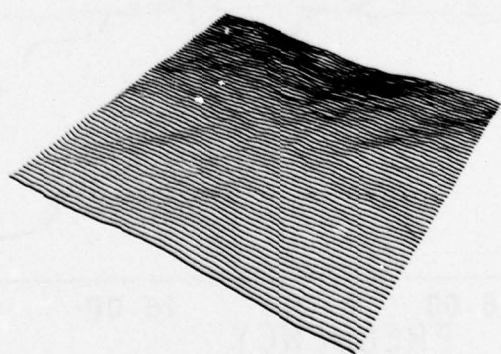
Figure 6.12 Comparison of magnitude of OTF and estimate



(a) θ



(b) $\hat{\theta} = \text{Estimate 1}$



(c) $\hat{\theta} = \text{Estimate 2}$

Figure 6.13 Comparison of phase of OTF and estimates

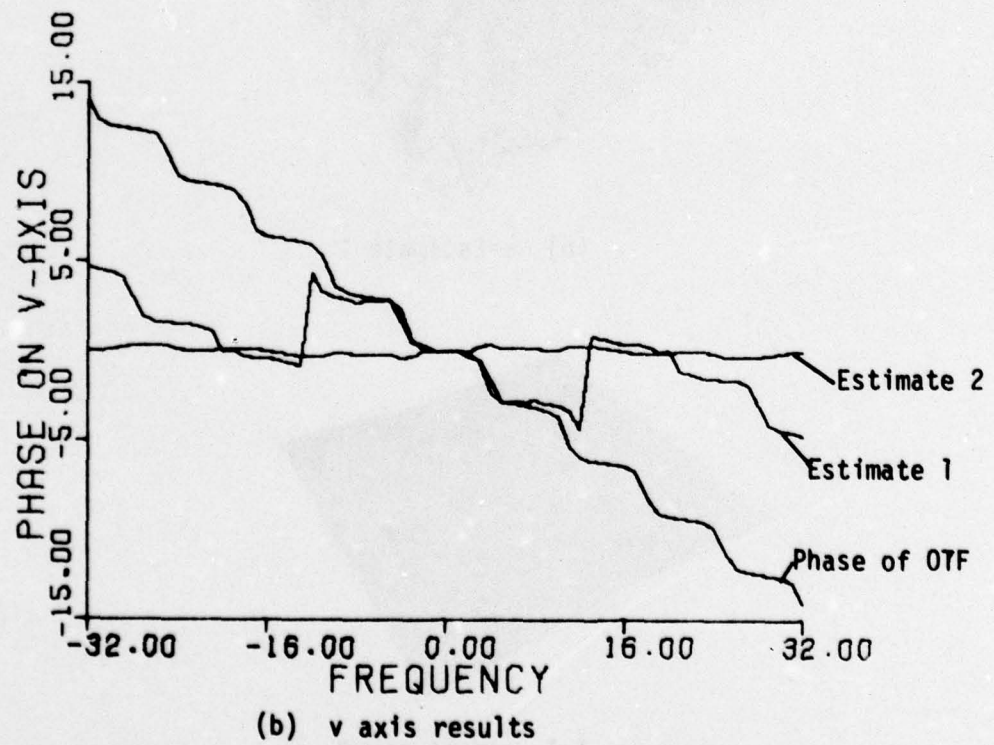
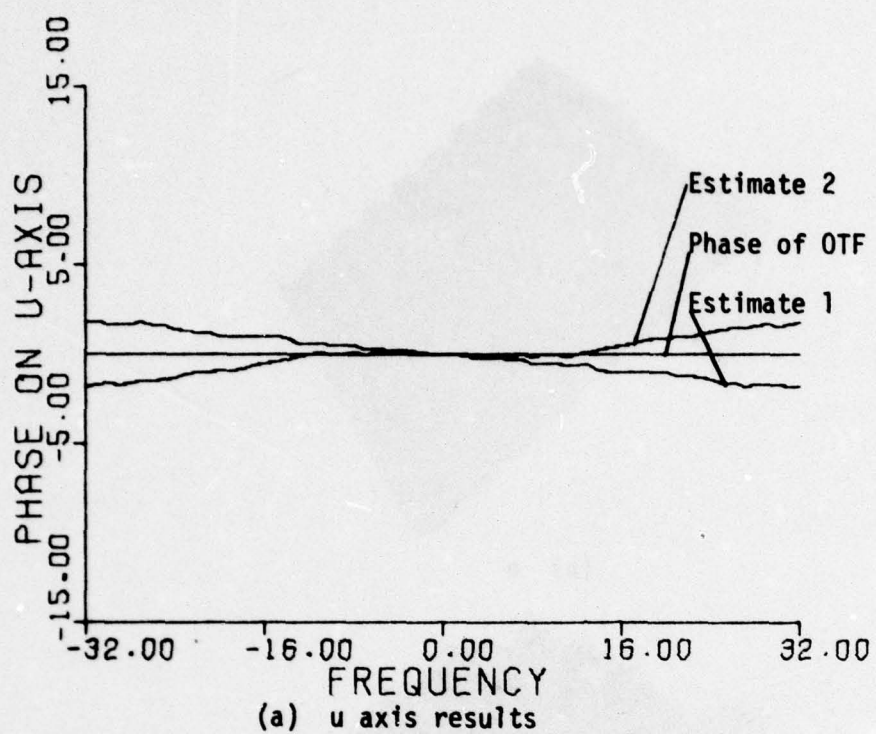
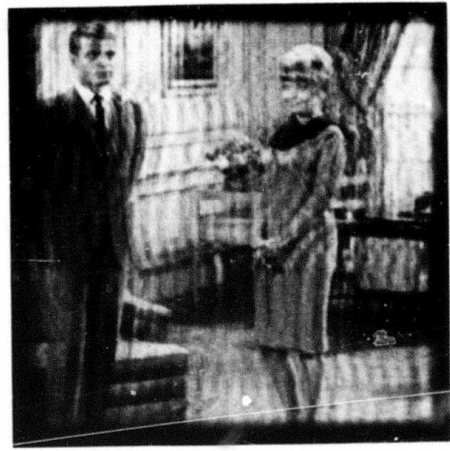


Figure 6.14 Comparison of phase of OTF and estimates



(a) degraded image



(b) magnitude of OTF given
phase of OTF given



(c) magnitude of OTF given
phase of OTF estimated as 0



(d) magnitude of OTF given
phase estimate = Estimate 2

Figure 6.15 Restorations



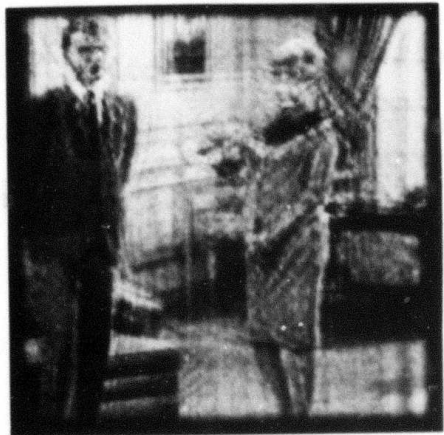
(e) magnitude of OTF estimated
phase of OTF given



(f) magnitude of OTF estimated
phase of OTF estimated as 0



(g) magnitude of OTF estimated
phase estimate = Estimate 2



(h) magnitude of OTF estimated
phase estimate = Estimate 1

Figure 6.15 (Cont'd)

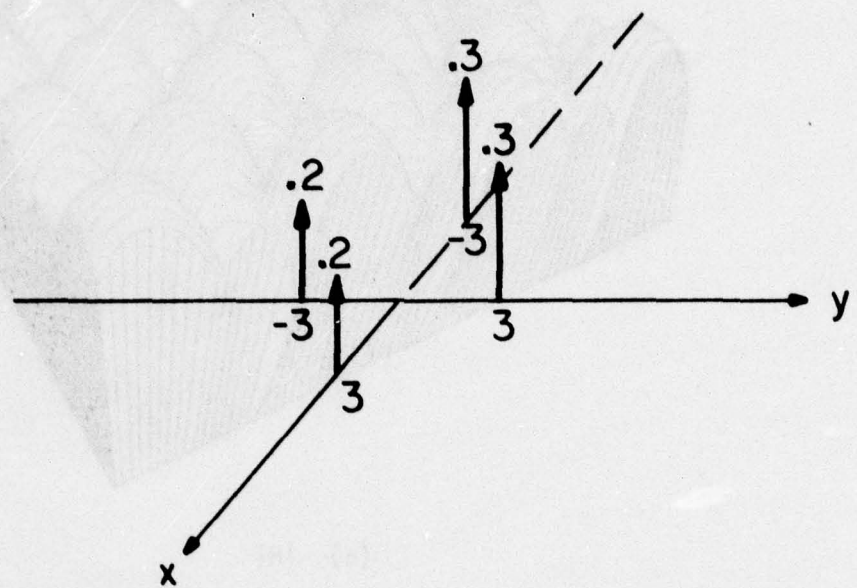
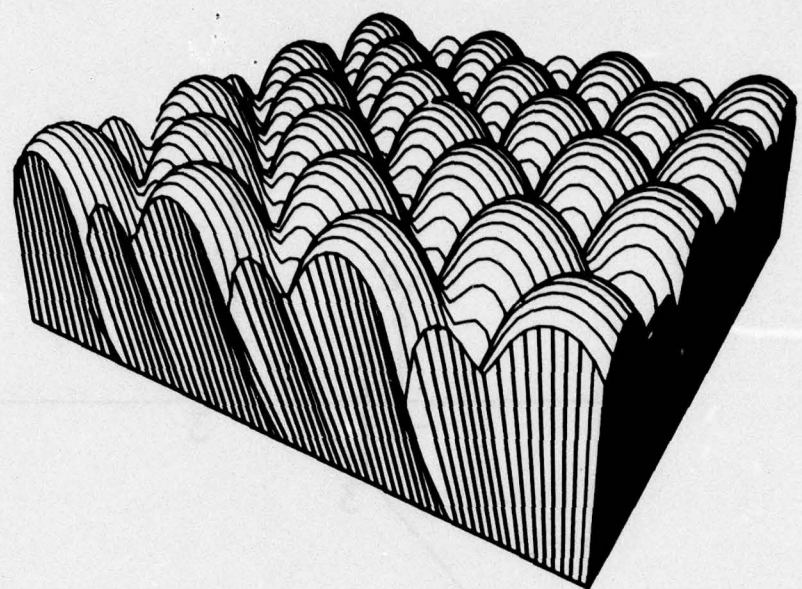
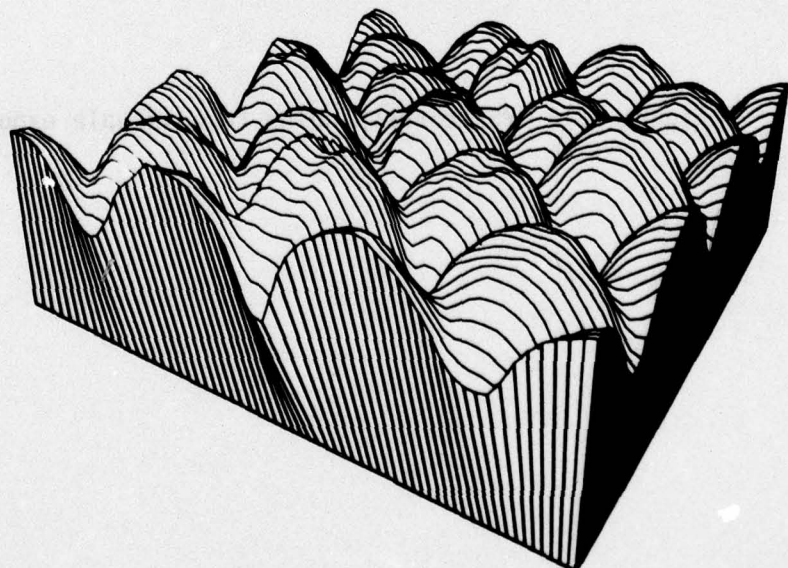


Figure 6.16 PSF corresponding to quadruple exposure

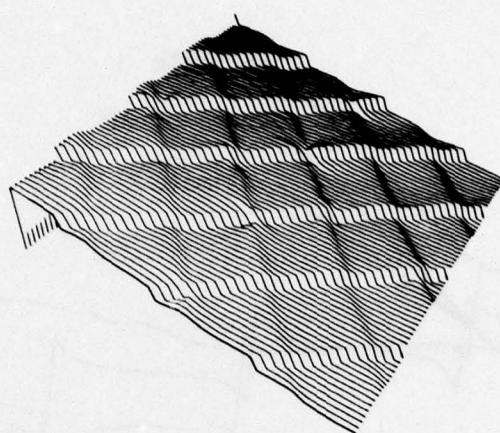


(a) $|H|$

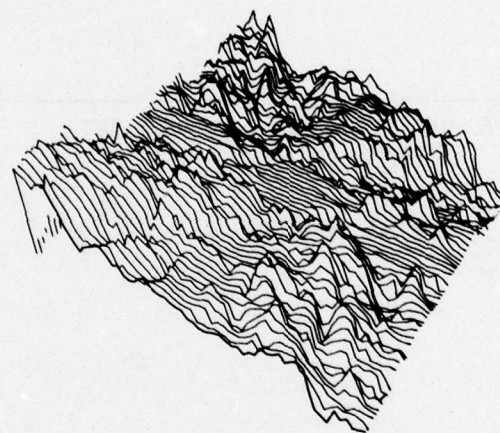


(b) $|\hat{H}|$

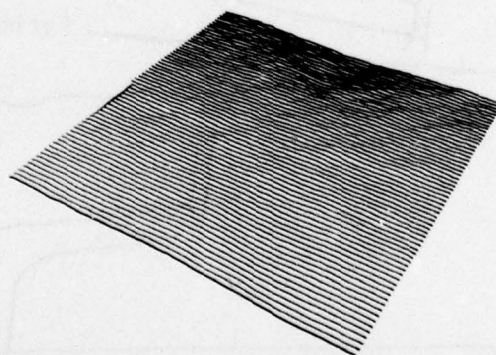
Figure 6.17 Comparison of magnitude of OTF and estimate



(a) θ

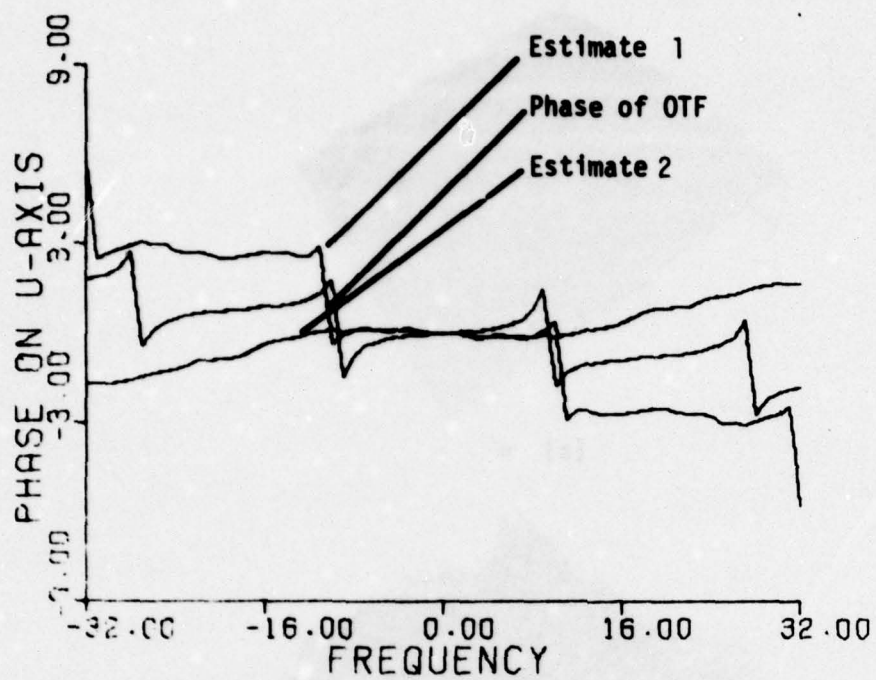


(b) $\hat{\theta} = \text{Estimate 1}$

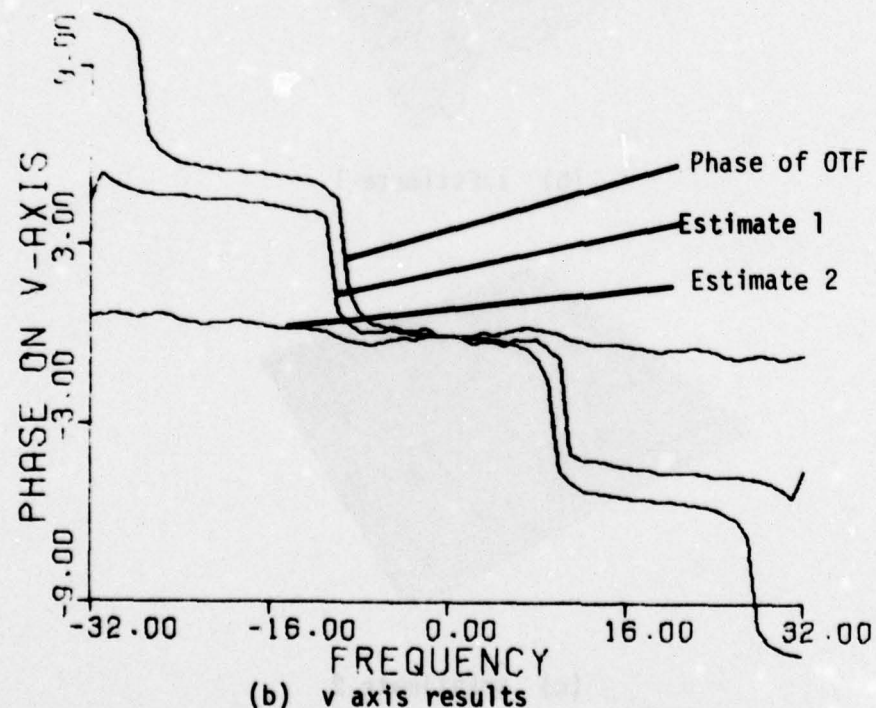


(c) $\hat{\theta} = \text{Estimate 2}$

Figure 6.18 Comparison of phase of OTF and estimates



(a) u axis results



(b) v axis results

Figure 6.19 Comparison of phase of OTF and estimates

**Best
Available
Copy**



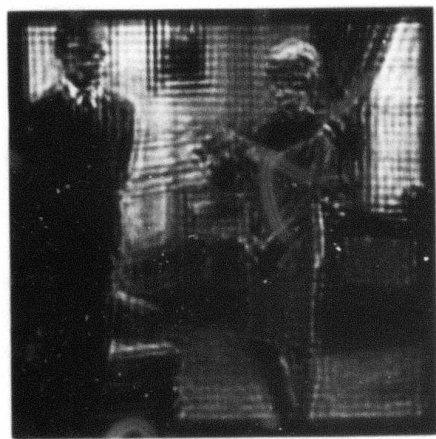
(a) degraded image



(b) magnitude of OTF given phase of OTF given



(c) magnitude of OTF given phase of OTF estimated as 0

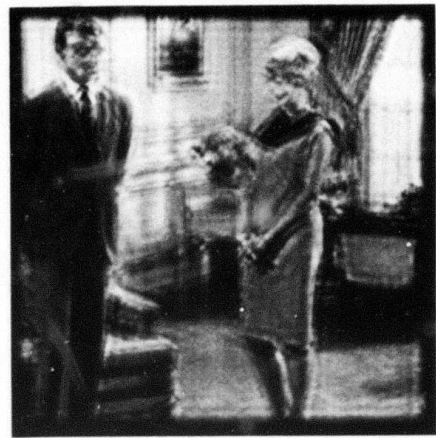


(d) magnitude of OTF given phase estimate = Estimate 2

Figure 6.20 Restorations



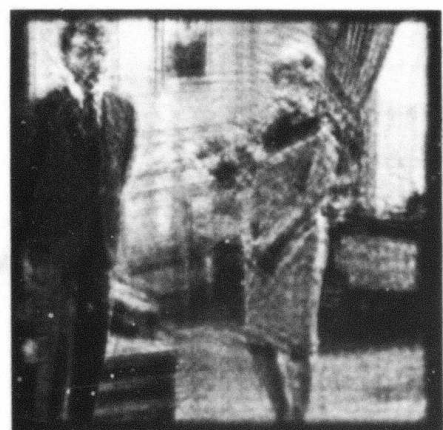
(e) magnitude of OTF estimated
phase of OTF given



(f) magnitude of OTF estimated
phase of OTF estimated as 0



(g) magnitude of OTF estimated
phase estimate = Estimate 2



(h) magnitude of OTF estimated
phase estimate = Estimate 1

Figure 6.20 (Cont'd)

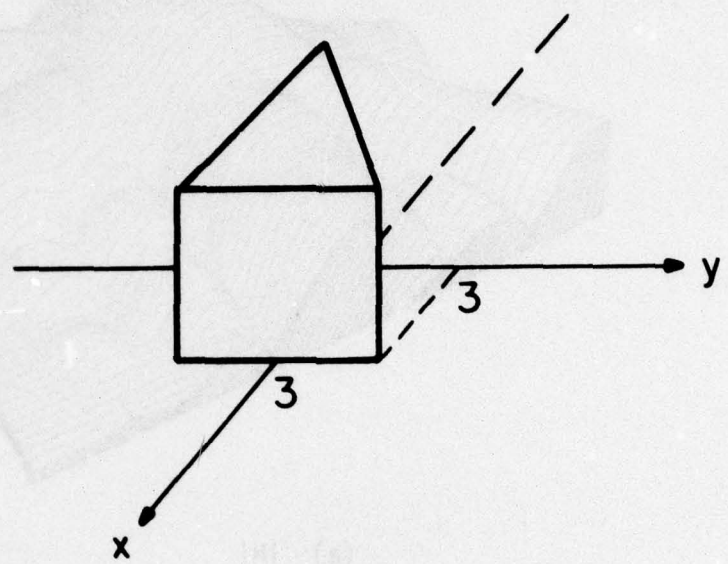
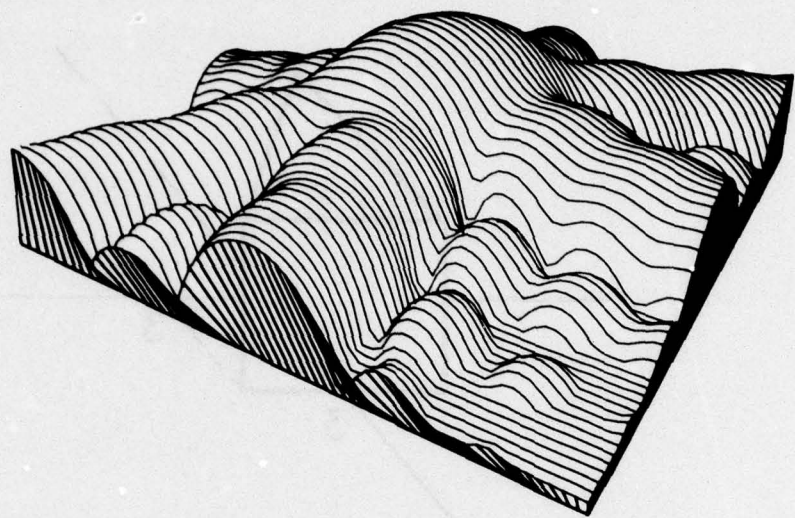
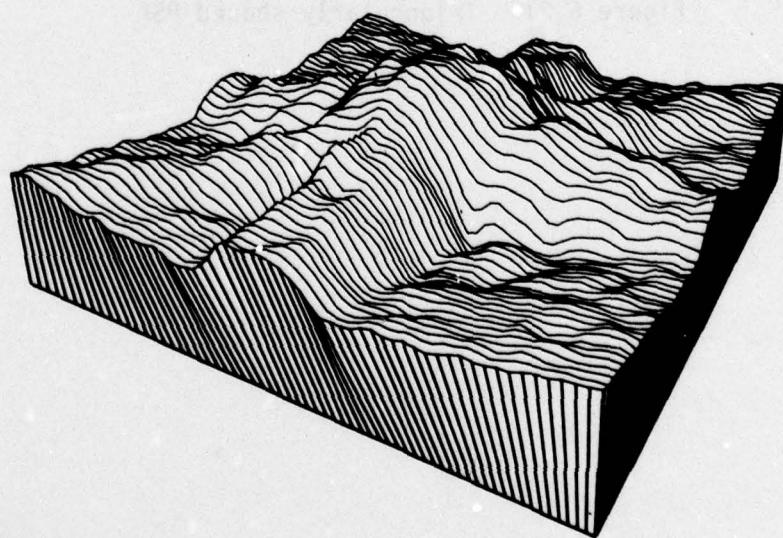


Figure 6.21 Triangularly shaped PSF

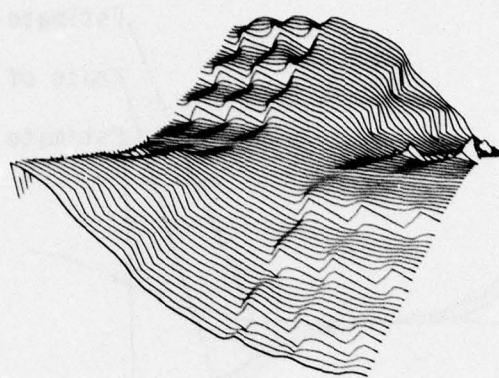


(a) $|H|$

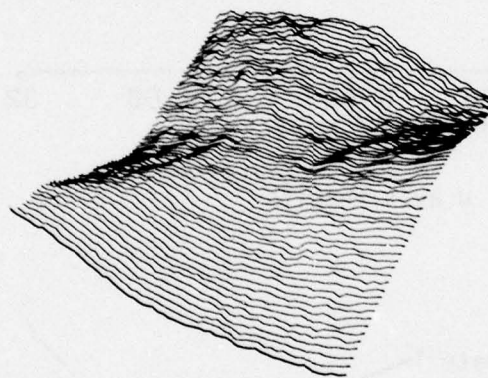


(b) $|\hat{H}|$

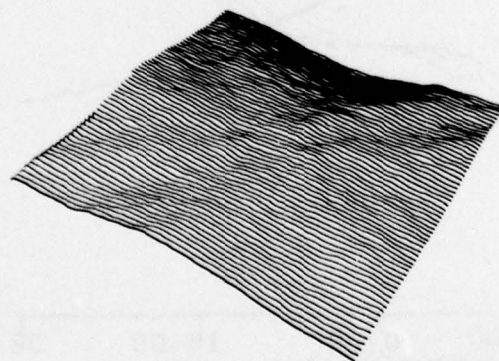
Figure 6.22 Comparison of magnitude of OTF and estimate



(a) θ

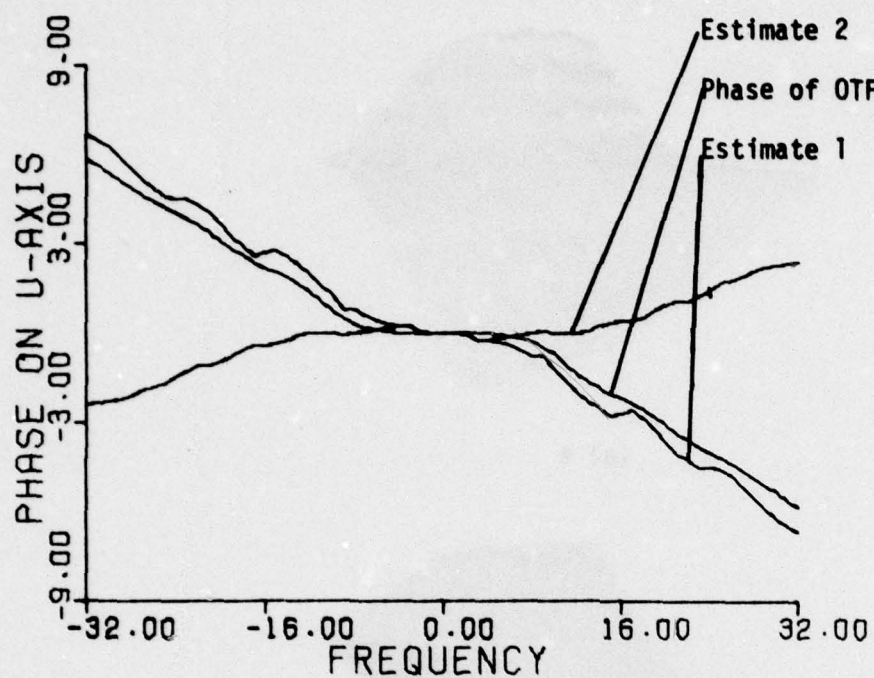


(b) $\hat{\theta} = \text{Estimate 1}$

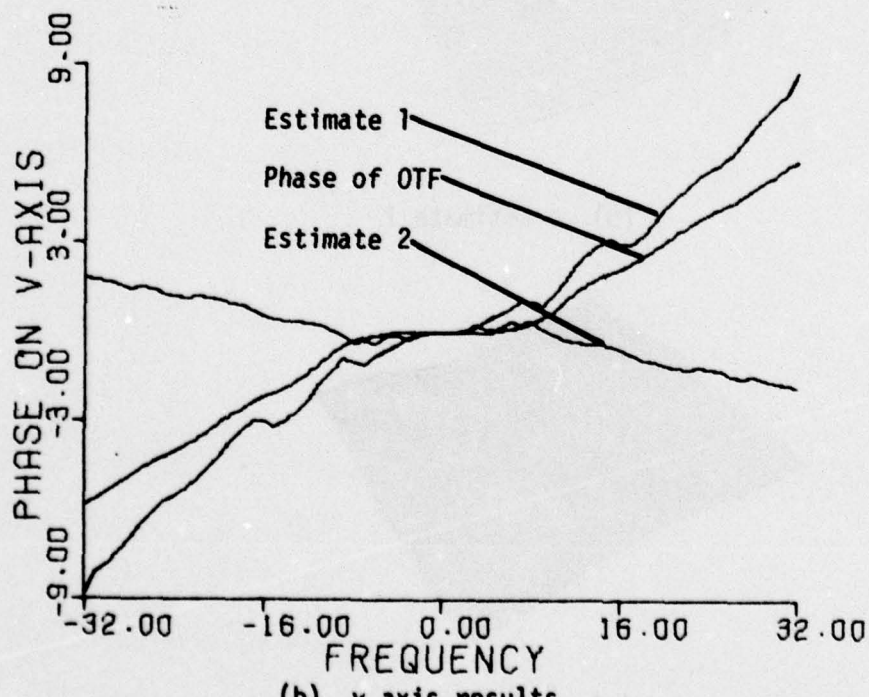


(c) $\hat{\theta} = \text{Estimate 2}$

Figure 6.23 Comparison of phase of OTF and estimates



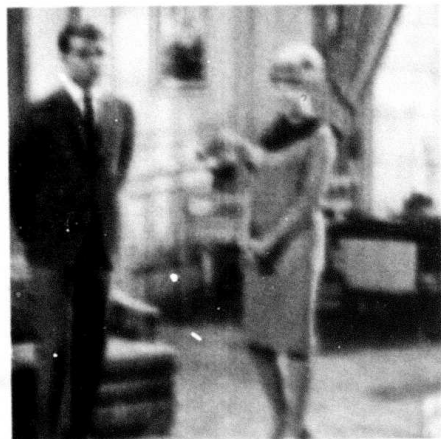
(a) u axis results



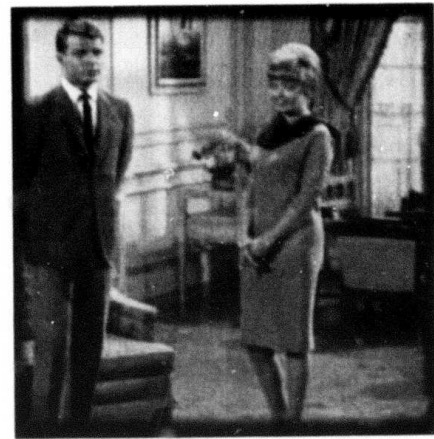
(b) v axis results

Figure 6.24 Comparison of phase of OTF and estimates

**Best
Available
Copy**



(a) degraded image



(b) magnitude of OTF given
phase of OTF given



(c) magnitude of OTF given
phase of OTF estimated as 0



(d) magnitude of OTF given
phase estimate = Estimate 2

Figure 6.25 Restorations



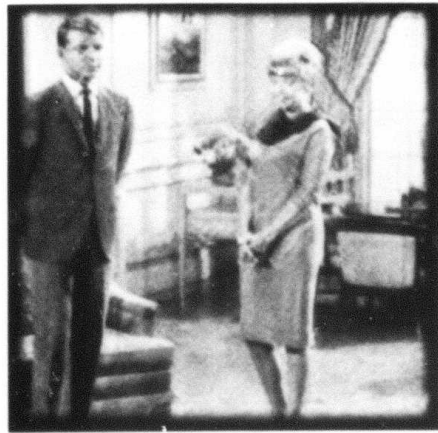
(e) magnitude of OTF estimated
phase of OTF given



(f) magnitude of OTF estimated
phase of OTF estimated as 0



(g) magnitude of OTF estimated
phase estimate = Estimate 2



(h) magnitude of OTF estimated
phase estimate = Estimate 1

Figure 6.25 (Cont'd)

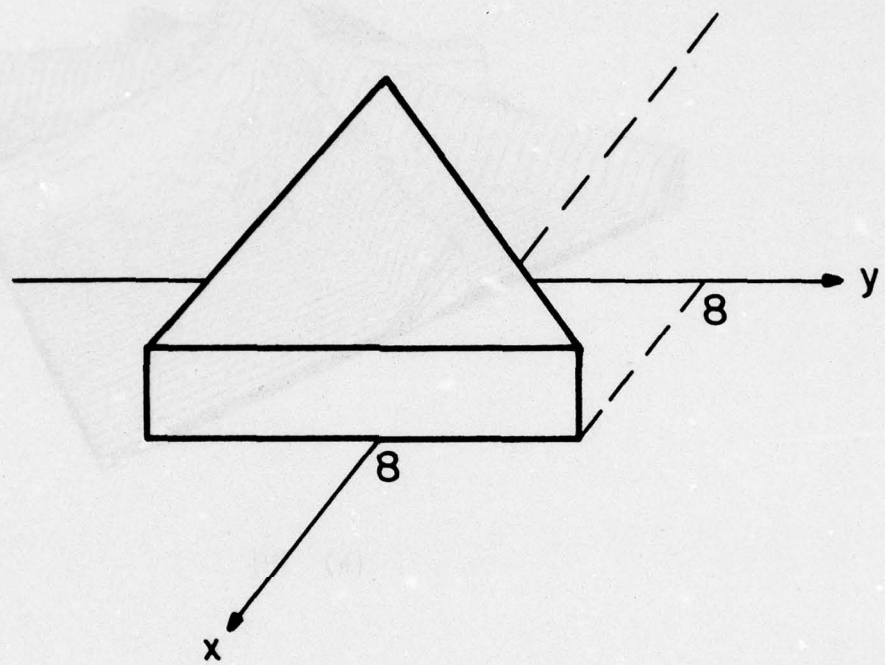
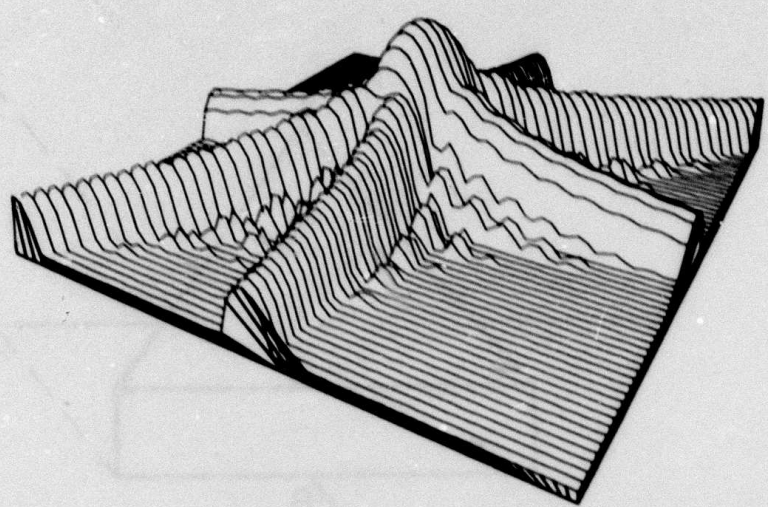
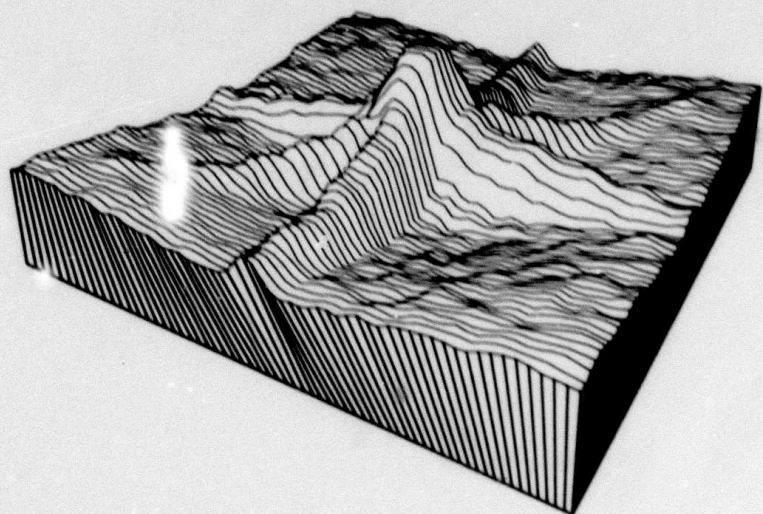


Figure 6.26 Triangularly shaped PSF

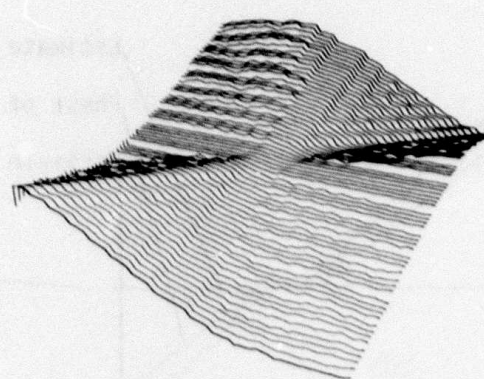


(a) $|H|$

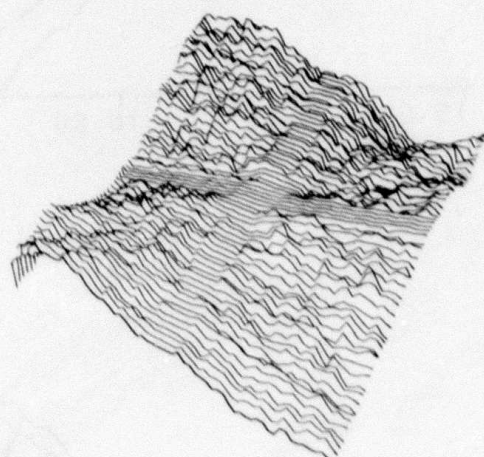


(b) $|\hat{H}|$

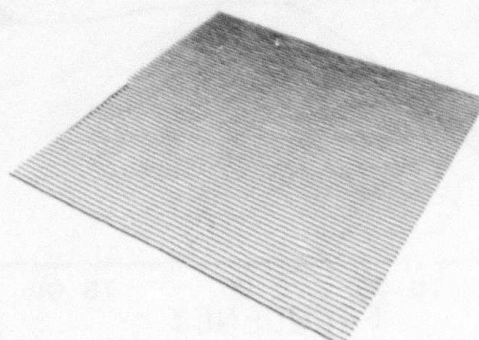
Figure 6.27 Comparison of magnitude of OTF and estimate



(a) θ

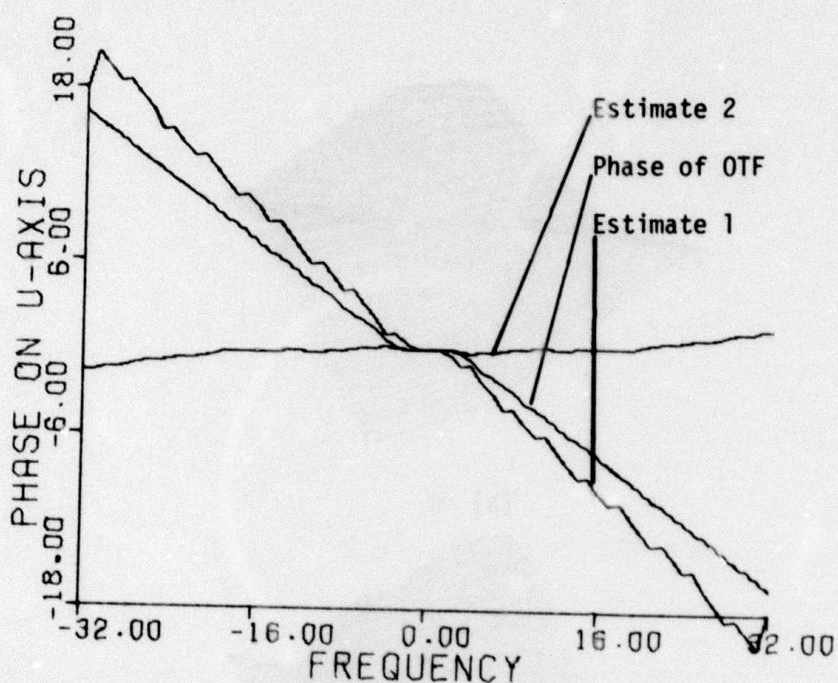


(b) $\hat{\theta} = \text{Estimate 1}$

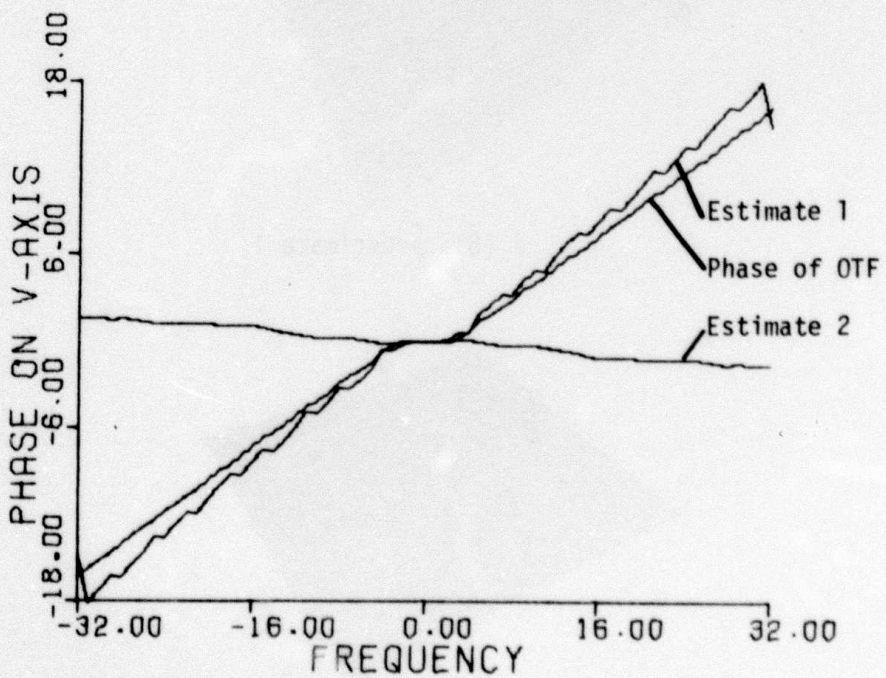


(c) $\hat{\theta} = \text{Estimate 2}$

Figure 6.28 Comparison of phase of OTF and estimates



(a) u axis results



(b) v axis results

Figure 6.29 Comparison of phase of OTF and estimates

**Best
Available
Copy**



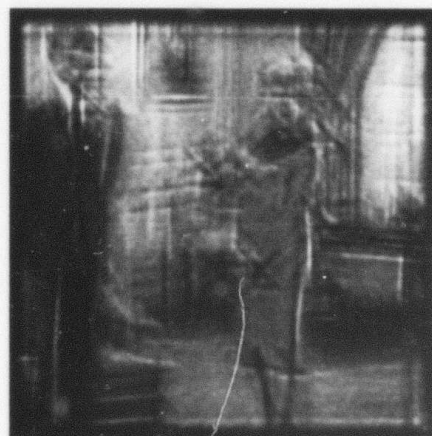
(a) degraded image



(b) magnitude of OTF given
phase of OTF given

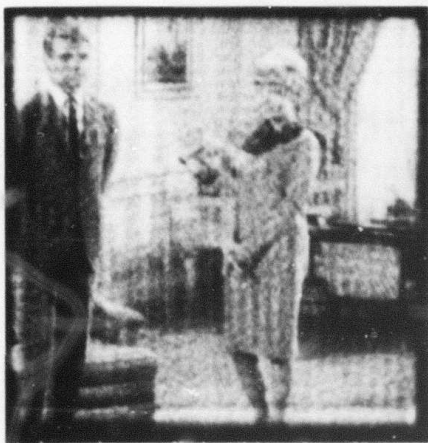


(c) magnitude of OTF given
phase of OTF estimated as 0

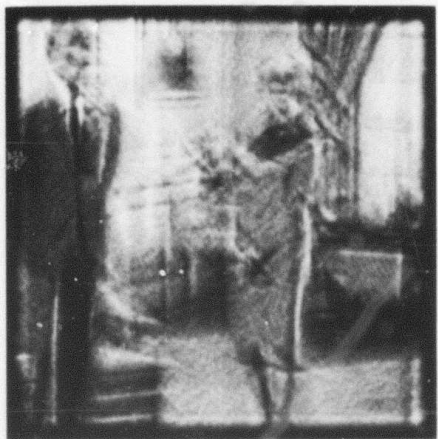


(d) magnitude of OTF given
phase estimate = Estimate 2

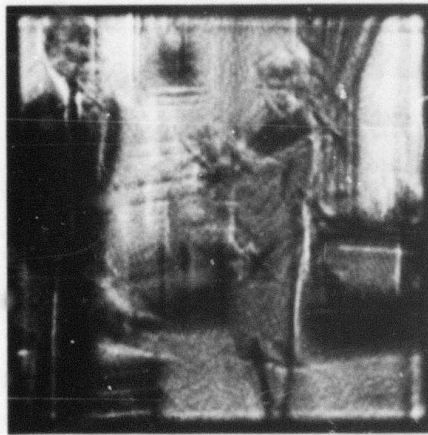
Figure 6.30 Restorations



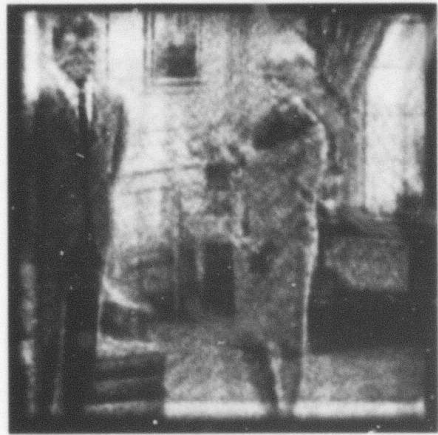
(e) magnitude of OTF estimated
phase of OTF given



(f) magnitude of OTF estimated
phase of OTF estimated as 0



(g) magnitude of OTF estimated
phase estimate = Estimate 2



(h) magnitude of OTF estimated
phase estimate = Estimate 1

Figure 6.30 (Cont'd)

Chapter 7

RESULTS ON REAL WORLD BLURRED IMAGES

This chapter presents the results for three photographically induced blurs. To induce the first two blurs the camera was jiggled and vibrated during exposure. The third blurred image was obtained from a private source; the blur was apparently the result of an incorrect use of the camera.

The blurred photographs were digitized to 512 x 512 pixels and the estimates of the OTF were made using the 512 x 512 blurred images. A 50% overlapping of subimages gave 225 subimages of 64 x 64 pixels each. The estimate of the magnitude of the OTF was made via the method of Cannon [26-28]. The estimate of the power spectrum of the undegraded image was the average power spectrum of the power spectra of the images of Figures 5.1b, c, and d. The phase estimate was obtained using a Parzen window and using recursion (5-13).

For the first two blurred images the restorations were made on each of the four 256 x 256 pixel quadrants of the 512 x 512 pixel blurred image. For the third blurred image four restorations of 256 x 256 pixels were made; the four restorations centered prominent features within the 512 x 512 pixel blurred image.

In Figure 7.1 is the same scene before and after the photographically induced blur. Note the "before" picture is earlier in time and is not used in the restoration. Figure 7.2 presents perspective plots of the estimates of the magnitude and phase of the OTF.

Figures 7.3-7.6 present the results of the restorations on the

**Best
Available
Copy**

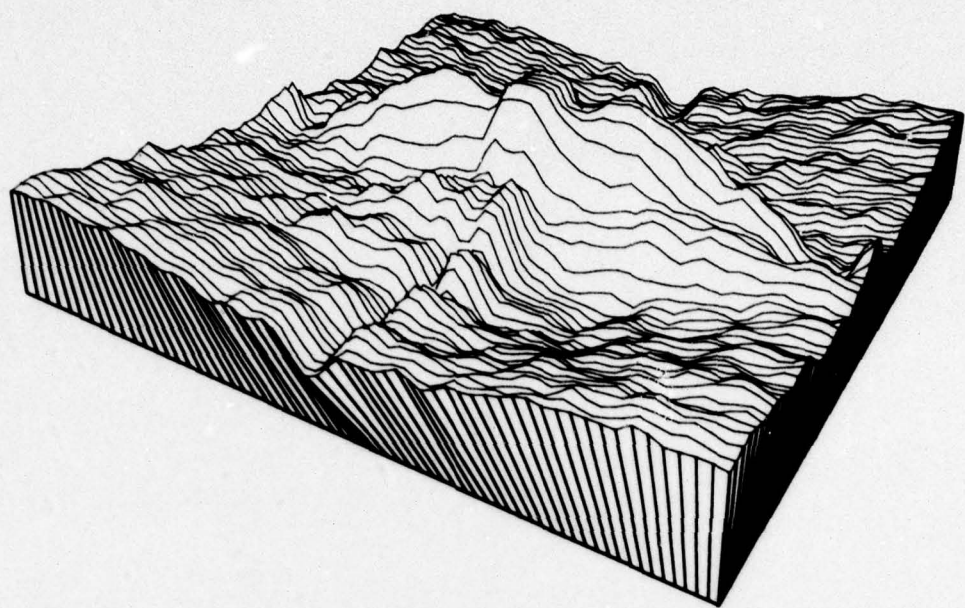


(a)

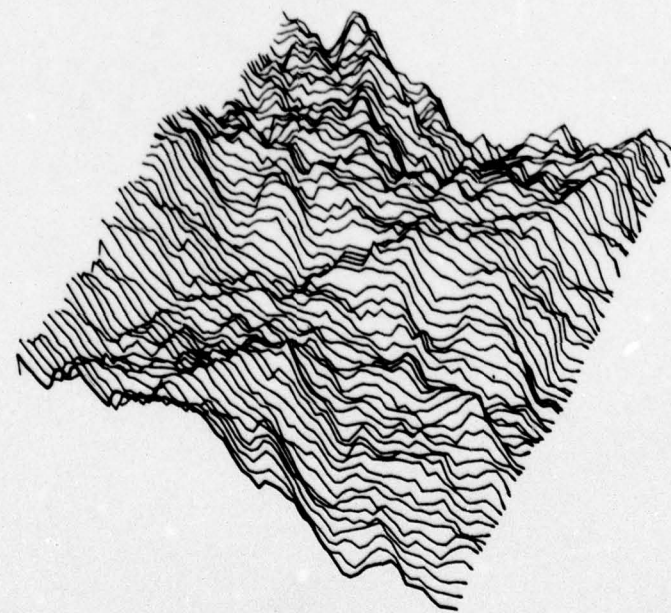


(b)

Figure 7.1 Scene before and after photographically induced blur



(a) $|H|$



(b) $\hat{\theta}$ (minimum = -1.04 radians,
maximum = 1.04 radians)

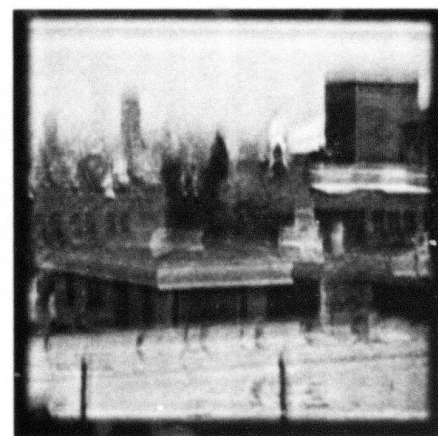
Figure 7.2 Estimates of magnitude and phase of OTF



(a) degraded

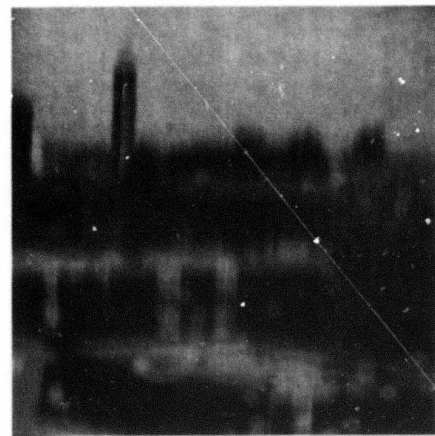


(b) phase of OTF estimated as 0

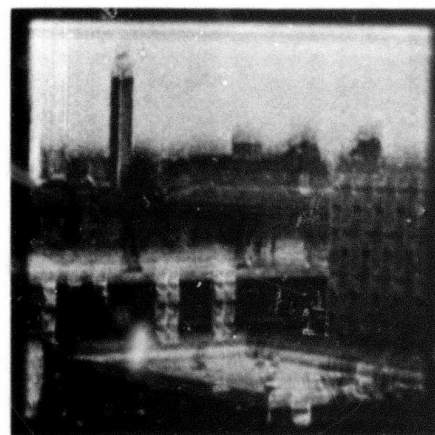


(c) phase estimate = Estimate 2

Figure 7.3 Blurred image and restorations



(a) degraded



(b) phase of OTF estimated as 0



(c) phase estimate = Estimate 2

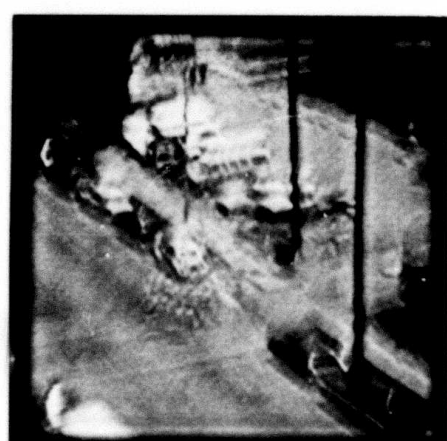
Figure 7.4 Blurred image and restorations



(a) degraded



(b) phase of OTF estimated as 0



(c) phase estimate = Estimate 2

Figure 7.5 Blurred image and restorations



(a) degraded



(b) phase of OTF estimated as 0



(c) phase estimate = Estimate 2

Figure 7.6 Blurred image and restorations

four 256 x 256 pixel quadrants of the 512 x 512 pixel blurred image. In each of Figures 7.3-7.6 is presented the degraded quadrant together with a restoration using the estimate of the magnitude and phase of the OTF and a restoration using the estimate of the magnitude of the OTF and estimating the phase of the OTF to be zero.

Improvement is evident. In addition to an improvement in sharpness, some objects that were not recognizable in the blurred images are recognizable after restoration. In Figure 7.3a the vertical columns of the building in the northeast quadrant of the image are not resolved. In the restorations in Figures 7.3b and c the columns are resolved.

In Figure 7.4a the object on top of the tower is not recognizable. In the restorations in Figures 7.4b and c it is seen to be a ball. In addition, in Figures 7.4b and c note the improvement in definition of the windows and structure of the building which is in the center of the right-hand side of the frame.

In the restorations of Figures 7.5b and c the lines of the crosswalk are now defined. Additionally, there is better definition in the cars; it is now possible to recognize the Volkswagen as a Volkswagen. Note the increased resolution in the windows of the minibus.

In Figures 7.7-7.12 are presented the results corresponding to the second photographically induced blur. Again, an improvement in sharpness and increased resolution is observed. In Figures 7.9b and c note the increased sharpness and definition in the tree in the southwest quadrants, the tree in the center of the right-hand side of the frames, and the trees along the top of the frames. Additionally, note

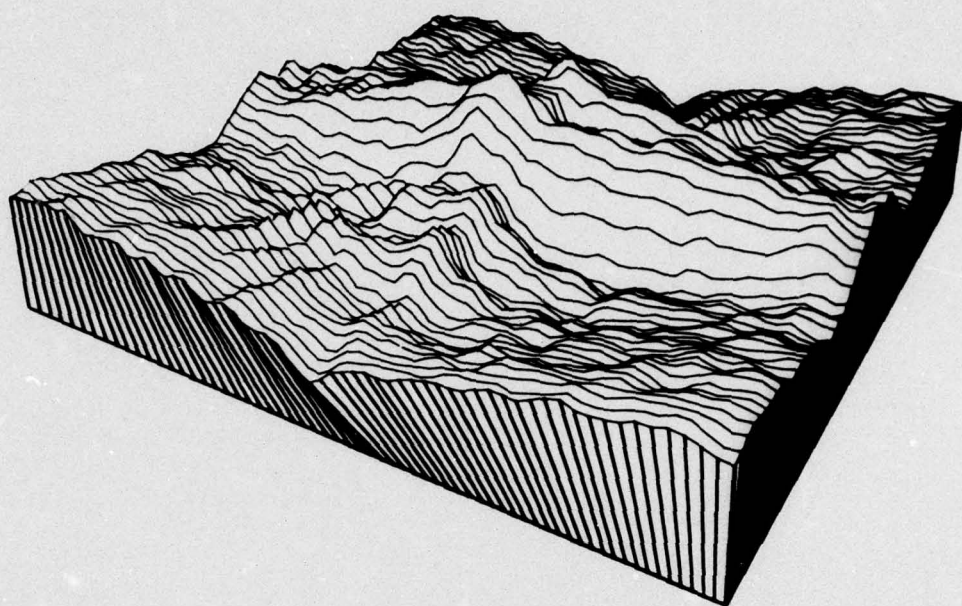


(a)

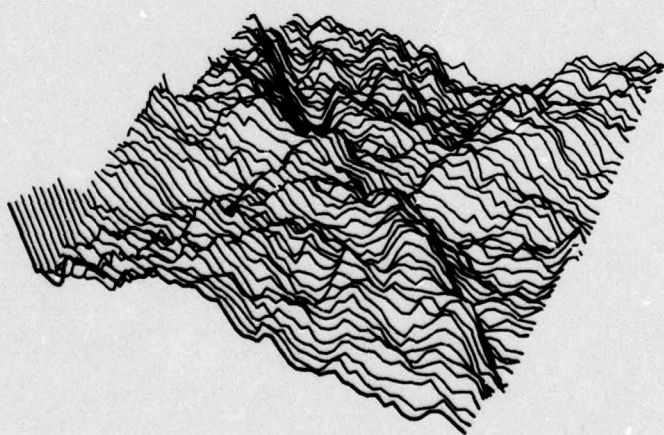


(b)

Figure 7.7 Scene before and after photographically induced blur



(a) $|\hat{H}|$

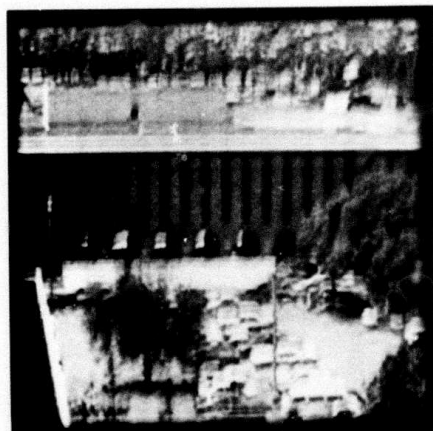


(b) $\hat{\theta}$ (minimum = $-.69$ radians,
maximum = $.69$ radians)

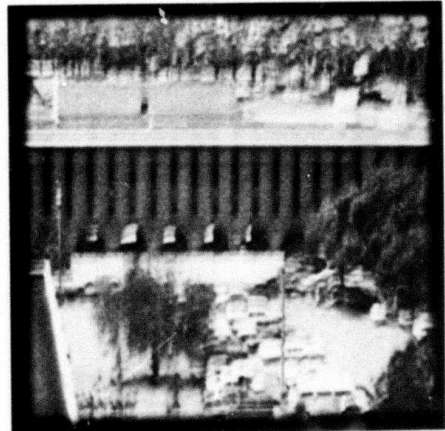
Figure 7.8 Estimates of magnitude and phase of OTF



(a) degraded

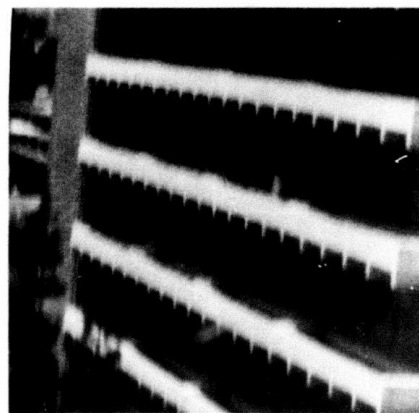


(b) phase of OTF estimated as 0

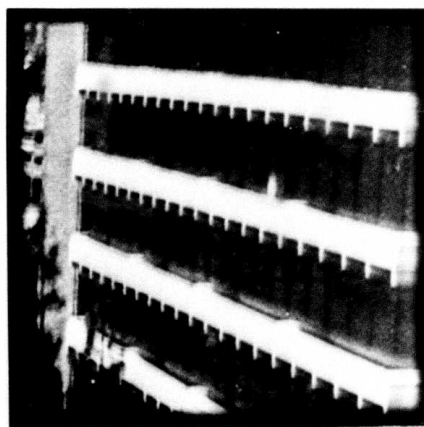


(c) phase estimate = Estimate 2

Figure 7.9 Blurred image and restorations



(a) degraded

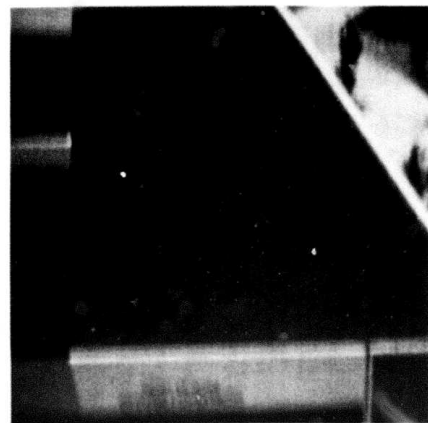


(b) phase of OTF estimated as 0

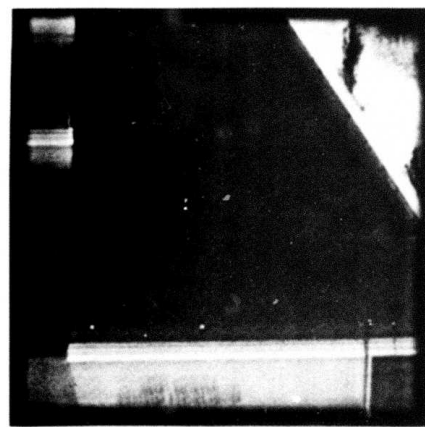


(c) phase estimate = Estimate 2

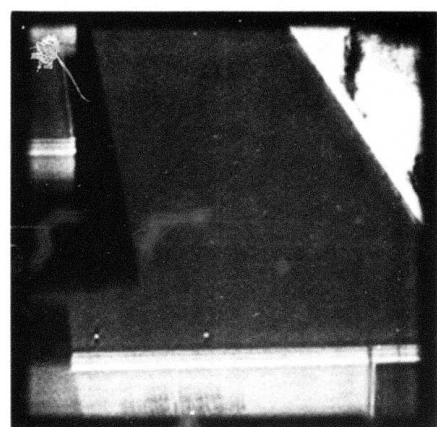
Figure 7.10 Blurred image and restorations



(a) degraded

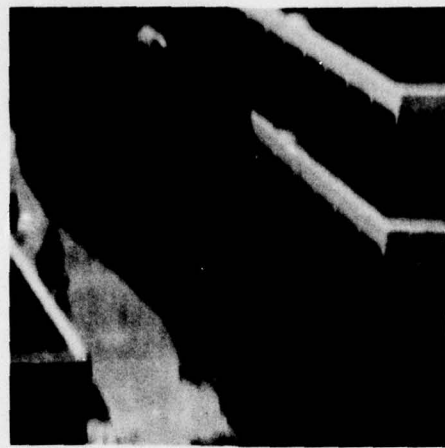


(b) phase of OTF estimated as 0

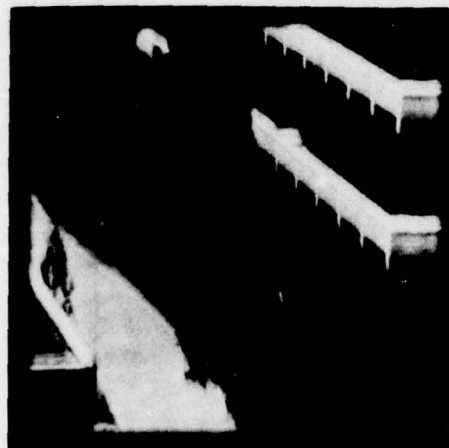


(c) phase estimate = Estimate 2

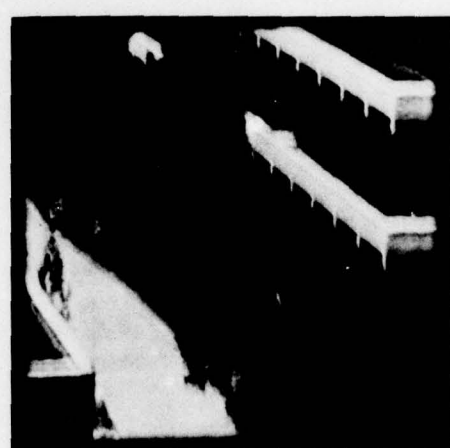
Figure 7.11 Blurred image and restorations



(a) degraded



(b) phase of OTF estimated as 0



(c) phase estimate = Estimate 2

Figure 7.12 Blurred image and restorations

the increased sharpness in the cars and building.

In Figures 7.10b and c there is better definition in the window panes and ledges. Note the increased sharpness in the trees of Figures 7.12b and c.

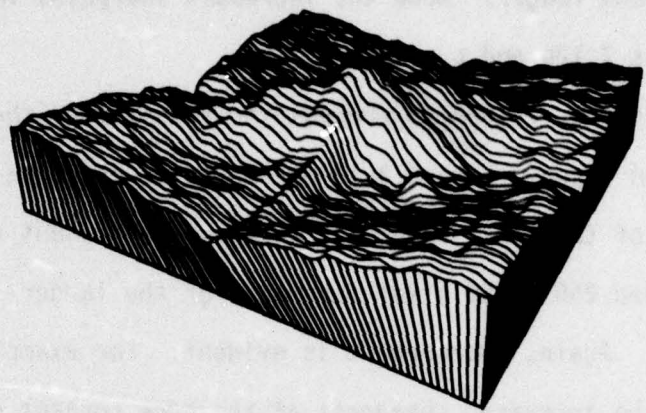
Figures 7.13-7.15 present the results for the third real world blurred image. Figure 7.13 presents the estimate of the magnitude and phase of the OTF. Figures 7.14 and 7.15 present restorations of selected 256 x 256 pixel subimages of the larger 512 x 512 blurred image. Again, improvement is evident. For example, in Figure 7.14b note the increased sharpness of the edge content compared to Figure 7.14a. Additionally, in Figure 7.14b note the better definition in the rocks.

In Figures 7.14d and 7.15b in addition to an increased sharpness some letters that were not discernible in the blurred versions are now discernible.

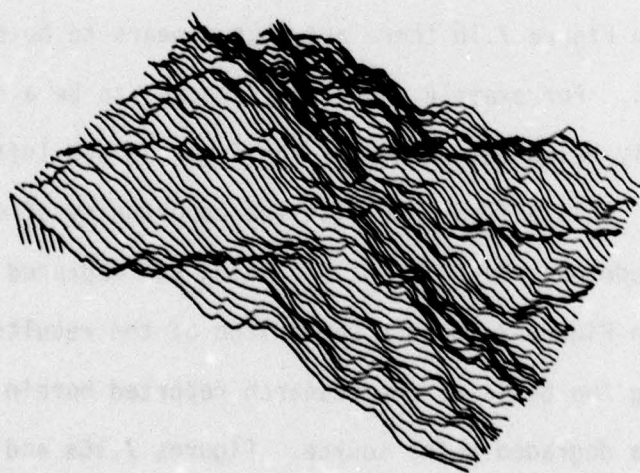
In Figure 7.1b there are what appears to be degraded point sources. For example, note what appears to be a degraded point source slightly below the center of the frame on the left-hand side of the frame. This affords one with the opportunity of estimating the magnitude and phase of the OTF using the degraded point source.

In Figure 7.16 is a comparison of the results using the techniques forming the basis of the research reported herein and results obtained using a degraded point source. Figures 7.16a and b are the same as Figures 7.5a and c, respectively, repeated here for convenience. Figure 7.16a is the degraded image. Figure 7.16b is the restoration obtained using the techniques reported herein.

**Best
Available
Copy**



(a) $|\hat{H}|$



(b) $\hat{\theta}$ (minimum = -1.5 radians,
maximum = 1.5 radians)

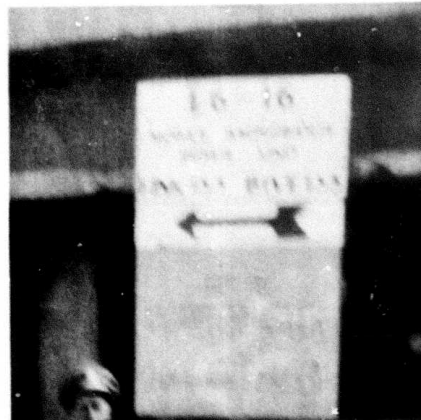
Figure 7.13 Estimates of magnitude and phase of OTF for third real world blurred image



(a) degraded



(b) restored



(c) degraded



(d) restored

Figure 7.14 Blurred images and restorations

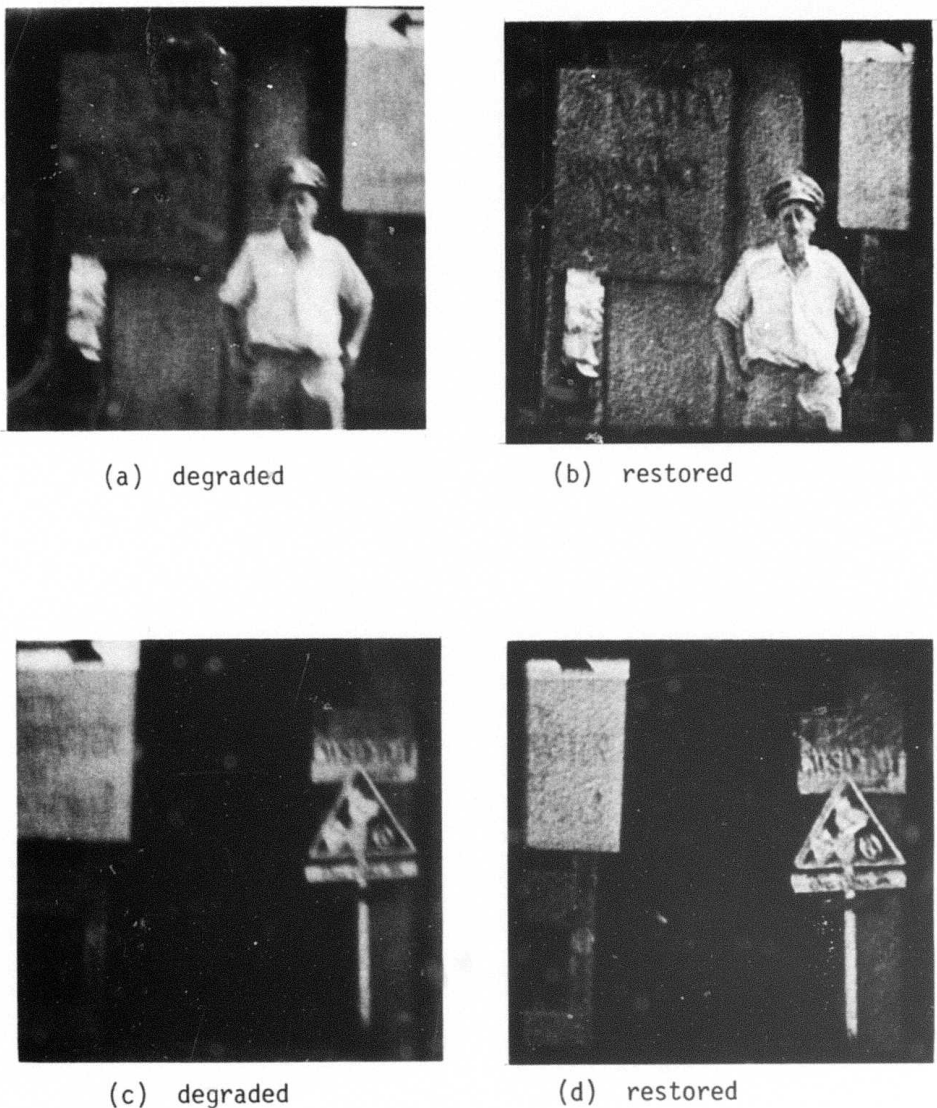
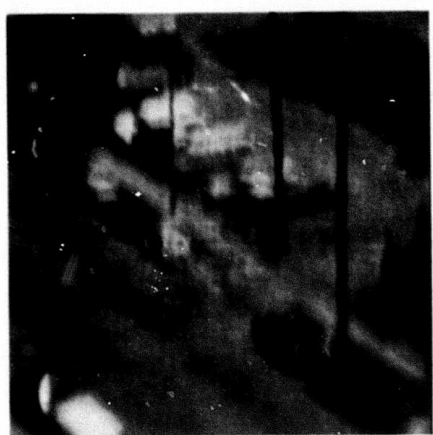


Figure 7.15 Blurred images and restorations



(a) degraded



(b) restoration using
techniques reported herein



(c) restoration using degraded
point source



(d) magnitude of OTF via method
of Cannon, phase of OTF
from degraded point source

Figure 7.16 Comparison of restoration results with restoration results using the degraded point source

Using the degraded point source in the northwest quadrant of Figure 7.16a to estimate both magnitude and phase of the OTF and using these estimates to estimate the undegraded image, Figure 7.16c was obtained. The degraded point sources are now closer to points. However, the rest of the image is probably a little worse. It is concluded that, although theoretically possible, it is very difficult in practice to restore blurred images by using degraded point sources to estimate the OTF.

Figure 7.16d uses the magnitude estimate used in Figure 7.16b, that is, via the method of Cannon [26-28], and uses the phase estimate from the degraded point source. Note the degraded point sources are closer to points. Note, additionally, the improvement in the definition of the back of the Pinto parked immediately before the crosswalk.

Chapter 8

SUMMARY

8.1 Summary

Because of the unstable nature of the recursive estimate of the magnitude of the OTF, this estimate is of little practical value.

With regards to the recursive estimate of the phase of the OTF, from the results of Chapter 6 it is seen that, via the method of section 5.7, a reasonable estimate of the phase of the OTF can be calculated. Recall the method of section 5.7 zeros the edges of the subimages prior to the blurring operation. This has the associated effect of sharpening the approximation

$$\theta_{G_i}(u,v) \approx \theta_H(u,v) + \theta_{F_i}(u,v)$$

to equality.

Another approach to sharpening the approximation is to use larger subimages in the calculations. As the subimage size is increased, however, the cost of the phase estimate increases accordingly. In addition, a larger image is needed to support a reasonable convergence of the averages.

8.2 Open Question

Given a PSF of a given nonzero extent, at what subimage size will the approximation

$$\theta_{G_i}(u,v) \approx \theta_H(u,v) + \theta_{F_i}(u,v)$$

be sufficiently sharp to support a reasonable estimate of the phase of the OTF.

APPENDIX A

Theorem: The trigonometric polynomial

$$T(u) = \sum_{k=0}^L a_k \cos\left(\frac{2\pi k u}{N}\right) + b_k \sin\left(\frac{2\pi k u}{N}\right)$$

can have at most $2L$ real zeros in the interval $\left(-\frac{N}{2}, \frac{N}{2}\right]$, even if each multiple root is counted the number of times it occurs.

Proof: Let us use the following identities.

$$\cos u = \frac{e^{ju} + e^{-ju}}{2}, \quad \sin u = \frac{e^{ju} - e^{-ju}}{2j}.$$

It follows that

$$T(u) = \sum_{k=-L}^L c_k e^{(j2\pi k u/N)}$$

where the c_k 's are complex constants.

$$\begin{aligned} T(u) &= e^{(-j2\pi Lu/N)} \sum_{k=-L}^L c_k e^{(j2\pi(k+L)u/N)} \\ &= e^{(-j2\pi Lu/N)} \sum_{\ell=0}^{2L} d_\ell e^{(j2\pi \ell u/N)} \end{aligned}$$

Now consider the polynomial

$$P(z) = d_0 + d_1 z + d_2 z^2 + \dots + d_{2L} z^{2L}$$

and form the correspondence

$$z = e^{(j2\pi u/N)}$$

Note that to each $u \in \left(-\frac{N}{2}, \frac{N}{2}\right]$ corresponds a unique z . Now

$$p(z) = e^{(j2\pi Lu/N)} T(u)$$

Differentiation with respect to u gives

$$\frac{\partial p(z)}{\partial z} \frac{\partial z}{\partial u} = \frac{j2\pi L}{N} e^{(j2\pi Lu/N)} T(u) + e^{(j2\pi Lu/N)} \frac{\partial T(u)}{\partial u}$$

$$p'(z) \frac{j2\pi}{N} e^{(j2\pi u/N)} = e^{(j2\pi Lu/N)} \left[\frac{j2\pi L}{N} T(u) + T'(u) \right]$$

$$p'(z) = N \frac{e^{[j2\pi(L-1)u/N]}}{j2\pi} \left[\frac{j2\pi L}{N} T(u) + T'(u) \right]$$

and via induction it can be shown that

$$p^{(s)}(z) = e^{[j2\pi(L-s)u/N]} [\lambda_0 T(u) + \lambda_1 T'(u) + \dots + \lambda_s T^{(s)}(u)] \quad (A-1)$$

where the λ_i 's are complex constants.

Now assume that u_0 is an m -fold zero of $T(u)$. This implies that

$$T(u_0) = T'(u_0) = \dots = T^{(m-1)}(u_0) = 0.$$

For $z_0 = e^{(j2\pi u_0/N)}$ and from equation (A-1) it follows that

$$p(z_0) = p'(z_0) = \dots = p^{(m-1)}(z_0) = 0.$$

Thus, to each m -fold zero of $T(u)$ corresponds an m -fold zero of $p(z)$.

The number of zeros of $p(z)$ cannot exceed $2L$ where the multiplicities of each zero is taken into account. Since to each zero of $T(u)$ of multiplicity m for $u \in \left(-\frac{N}{2}, \frac{N}{2}\right]$ corresponds a zero of $p(z)$ of

multiplicity m , the number of zeros of $T(u)$ also cannot exceed $2L$
where here again the multiplicities of each zero is taken into account.

REFERENCES

- [1] Hellstrom, C. W., "Image Restoration by the Method of Least Squares," J. Opt. Soc. Amer., Vol. 57, No. 3, March 1967, pp. 297-303.
- [2] McGlamery, B. L., "Restoration of Turbulence Degraded Images," J. Opt. Soc. Amer., Vol. 57, No. 3, March 1967, pp. 293-297.
- [3] Andrews, H. C., Computer Techniques in Image Processing, Academic Press, New York, 1970.
- [4] Robbins, G. M., "Image Restoration for a Class of Linear Spatially-Variant Degradations," Pattern Recognition, Vol. 2, No. 2, July 1970, pp. 91-105.
- [5] Frieden, B. R., "Restoring with Maximum Likelihood," Technical Report 67, U. of Arizona, Feb. 1971.
- [6] Frieden, B. R., "Restoring with Maximum Likelihood and Maximum Entropy," J. Opt. Soc. Amer., Vol. 62, No. 4, April 1972, pp. 511-518.
- [7] Andrews, H. C., A. G. Tescher and R. P. Kruger, "Image Processing by Digital Computer," IEEE Spectrum, Vol. 9, No. 7, July 1972, pp. 20-32.
- [8] Robbins, G. M. and T. S. Huang, "Inverse Filtering for Linear Shift-Variant Imaging Systems," Proc. IEEE, Vol. 60, No. 7, July 1972, pp. 862-872.
- [9] Sawchuk, A. A., "Space-Variant Image Motion Degradation and Restoration," Proc. IEEE, Vol. 60, No. 7, July 1972, pp. 854-861.
- [10] Sondhi, M. M., "Image Restoration: The Removal of Spatially Invariant Degradations," Proc. IEEE, Vol. 60, No. 7, July 1972, pp. 842-853.
- [11] Hunt, B. R., "The Application of Constrained Least Squares Estimation to Image Restoration by Digital Computer," IEEE Trans. Computers, Vol. C-22, No. 9, Sept. 1973, pp. 805-812.
- [12] Sawchuk, A. A., "Space-Variant System Analysis of Image Motion," J. Opt. Soc. Am., Vol. 63, No. 9, Sept. 1973, pp. 1052-1063.
- [13] Andrews, H. C. and C. L. Patterson, "Outer Product Expansions and Their Uses in Digital Image Processing," Amer. Math. Monthly, Vol. 82, No. 1, Jan. 1974, pp. 1-13.

- [14] Ekstrom, M. P., "Numerical Image Restoration by the Method of Singular-Value Decomposition," Proc. Seventh Hawaii International Conference on Systems Science, Honolulu, Hawaii, Jan. 1974, pp. 13-15.
- [15] Sawchuk, A. A., "Space-Variant Image Restoration by Coordinate Transformations," J. Opt. Soc. Amer., Vol. 64, No. 2, Feb. 1974, pp. 138-144.
- [16] Andrews, H. C., "Digital Image Restoration: A Survey," Computer, Vol. 7, No. 5, May 1974, pp. 36-45.
- [17] Hou, H. S., "Least Squares Image Restoration Using Spline Interpolation," USC/PI Report 650, U. of Southern California, ARPA Order No. 1706, Feb. 1976.
- [18] Andrews, H. C. and B. R. Hunt, Digital Image Restoration, Prentice-Hall, Englewood Cliffs, New Jersey, 1977.
- [19] Goodman, J. W., Introduction to Fourier Optics, McGraw-Hill, New York, 1968.
- [20] Tatian, B., "Method for Obtaining the Transfer Function from the Edge Response Function," J. Opt. Soc. Amer., Vol. 55, No. 8, August 1965, pp. 1014-1019.
- [21] Gennery, D. B., "Determination of Optical Transfer Function by Inspection of Frequency-Domain Plot," J. Opt. Soc. Am., Vol. 63, No. 12, Dec. 1973, pp. 1571-1577.
- [22] Honda, T., Y. Kukushima and J. Tsujiuchi, "An Estimation of the Amount of Motion in a Linear Motion Blurred Picture by Spectrum Analysis," Optica Acta, Vol. 23, No. 10, Oct. 1976, pp. 799-811.
- [23] Maitre, H., "Object Recognition in Numerical Images by Spectrum Zero Detection," Computer Graphics and Image Processing, Vol. 5, No. 2, June 1976, pp. 238-244.
- [24] Filip, A., "Estimating the Impulse Response of Linear, Shift-Invariant Image Degrading Systems," Ph.D. Thesis, M.I.T., October 1972.
- [25] Cole, E. R., "The Removal of Unknown Image Blurs by Homomorphic Filtering," Dept. of Computer Science, University of Utah, ARPA Technical Report UTEC-CSC-74-029, June 1973.
- [26] Cannon, T. M., "Digital Image Deblurring by Nonlinear Homomorphic Filtering," Dept. of Computer Science, University of Utah, ARPA Technical Report UTEC-CSC-74-091, August 1974.

- [27] Stockham, T. G., T. M. Cannon and R. B. Ingebretsen, "Blind Deconvolution Through Digital Signal Processing," Proc. IEEE, Vol. 63, No. 4, April 1975, pp. 678-692.
- [28] Cannon, T. M., "Blind Deconvolution of Spatially Invariant Image Blurs with Phase," IEEE Trans. ASSP, Vol. ASSP-24, No. 1, Feb. 1976, pp. 58-63.
- [29] O'Connor, B. and T. S. Huang, "Phase Unwrapping with Applications to Stability and Picture Deblurring," Image Understanding and Information Extraction, School of Electrical Engineering, Purdue U., Report TR-EE 77-16, March 1977, pp. 92-142.
- [30] Knox, K. T. and B. J. Thompson, "Recovery of Images from Atmospherically Degraded Short-Exposure Photographs," Astro. J., Vol. 193, Oct. 1, 1974, pp. L45-L48.
- [31] Knox, K. T., "Diffraction-Limited Imaging with Astronomical Telescopes," Ph.D. dissertation, U. of Rochester, N.Y., 1975.
- [32] Knox, K. T., "Image Retrieval from Astronomical Speckle Patterns," J. Opt. Soc. Am., Vol. 66, No. 11, Nov. 1976, pp. 1236-1239.
- [33] O'Neill, E. L. and A. Walther, "The Question of Phase in Image Formation," Optica Acta, Vol. 10, No. 1, Jan. 1963, pp. 33-40.
- [34] Walther, A., "The Question of Phase Retrieval in Optics," Optica Acta, Vol. 10, No. 1, Jan. 1963, pp. 41-49.
- [35] Roman, P. and A. S. Marathay, "Analyticity and Phase Retrieval," Nuova Cimento, Vol. 30, No. 6, Dec. 16, 1973, pp. 1452-1463.
- [36] Gerchberg, R. W. and W. O. Saxton, "A Practical Algorithm for the Determination of Phase from Image Diffraction Plane Pictures," Optik, Vol. 35, No. 2, April 1972, pp. 237-246.
- [37] Kohler, D. and L. Mandel, "Source Reconstruction from the Modulus of the Correlation Function: A Practical Approach to the Phase Problem of Optical Coherence Theory," J. Opt. Soc. Amer., Vol. 63, No. 2, Feb. 1973, pp. 126-134.
- [38] Hoenders, B. J., "On the Solution of the Phase Retrieval Problem," J. Math. Physics, Vol. 16, No. 9, Sept. 1975, pp. 1719-1725.
- [39] Gonsalves, R. A., "Phase Retrieval from Modulus Data," J. Opt. Soc. Amer., Vol. 66, No. 9, Sept. 1976, pp. 961-964.
- [40] Frieden, B. R. and D. Currie, "On Unfolding the Autocorrelation Function," presented at Opt. Soc. Amer. annual meeting, Tucson, Arizona, Oct. 1976.

- [41] Fienup, J. R., "Reconstruction of an Object from the Modulus of its Fourier Transform," presented at Opt. Soc. Amer. annual meeting, Toronto, Canada, Oct. 1977.
- [42] Ehn, D. C., "Calculation of Phase Error in the Pupil from the Point Spread Function," presented at Opt. Soc. Amer. annual meeting, Toronto, Canada, Oct. 1977.
- [43] McGlamery, B. L., "Image Restoration Techniques Applied to Astronomical Photography," in Astronomical Use of Television-type Image Sensors, report no. N71-28509-525 of the National Technical Information Service of the U. S. Dept. of Commerce, 1971.
- [44] Churchill, R. V., Complex Variables and Applications, McGraw-Hill, New York, 1960.
- [45] Natanson, I. P., Konstruktive Funktionentheorie, Akademie-Verlag, Berlin, 1955.
- [46] Welch, P. D., "The Use of Fast Fourier Transform for the Estimation of Power Spectra," IEEE Trans. ASSP, Vol. AU-15, No. 3, June 1967, pp. 70-73.
- [47] Papoulis, A., Probability, Random Variables, and Stochastic Processes, McGraw-Hill, New York, 1965.
- [48] Hildebrand, F. B., Introduction to Numerical Analysis, McGraw-Hill, New York, 1956.
- [49] Trbolet, J. M., "A New Phase Unwrapping Algorithm," IEEE Trans. ASSP, Vol. ASSP-25, No. 2, April 1977, pp. 170-177.